

POLITECNICO DI TORINO

Collegio di Ingegneria Chimica e dei Materiali

**Master of Science Course
in Materials Engineering**

Master of Science Thesis

Synthesis and investigation of noble metal-free mesoporous carbon-based catalyst for electrochemical CO₂ reduction



**Politecnico
di Torino**

Tutors

Prof. Simelys Pris Hernández Ribullen
Dr. Hilmar Guzmán

Candidate

Stefano Favero Costa

March 2022

Contents

Riassunto	I
1. Introduction.....	1
2. Electrochemical reduction of CO ₂	4
2.1 Electrocatalyst efficiency and other factors influencing the process.....	5
2.2 Electrochemical cell configurations	6
2.3 Electrolytes solutions	8
2.4 Electrocatalyst materials.....	9
2.5 Desired products and Reaction Pathways	15
3. Porous carbons for electrocatalysis.....	19
3.1 Doping	20
3.2 Synthesis of ordered mesoporous carbons	21
3.2.1 Templating	22
4. Purpose of the work.....	25
5. Materials, methods and experimental procedures	26
5.1 Materials	26
5.2 Synthesis procedure	26
5.2.1 Ordered mesoporous nitrogen-doped carbon	26
5.2.2 Ordered mesoporous nitrogen-doped carbon with copper	29
5.3 Characterisation techniques.....	31
5.4 Electrochemical activity testing.....	33
5.4.1 Electrochemical cell configuration and setup.....	34
5.4.2 ECSA measurements.....	36
5.4.3 Working electrodes preparation.....	36
6. Results and Discussion	39
6.1 Physical characterisation results	39
6.1.1 Nitrogen adsorption.....	39
6.1.2 X-ray diffraction.....	41
6.1.3 FESEM and EDS.....	43
6.1.4 Raman spectroscopy	45
6.1.5 X-ray photoelectron spectroscopy.....	47
6.2 Electrochemical behaviour of the synthesised N-doped carbon	51
6.2.1 Preliminary activity tests with RDE system	51

6.2.2 Electrochemical activity of carbon paper working electrodes	55
7. Conclusions	64
8. Future perspectives	65
List of abbreviations.....	66
List of figures.....	68
List of tables.....	70
Bibliography	71

Riassunto

Introduzione

Nell'ultimo secolo, l'eccessivo sfruttamento dei combustibili fossili come fonte di energia per soddisfare il fabbisogno energetico mondiale ha rilasciato nell'atmosfera un'enorme quantità di anidride carbonica, principale responsabile del riscaldamento globale, raggiungendo concentrazioni atmosferiche critiche di 415.2 ppm nel 2019 (Zhao & Quan, 2021). L'innalzamento della temperatura media di circa 1 °C ha portato alla comparsa di numerosi problemi ambientali, come ad esempio lo scioglimento dei ghiacciai ed eventi climatici estremi, che se non limitati metteranno seriamente a rischio la vita sulla Terra.

Tuttavia, ancora oggi la produzione di energia mondiale si basa ancora in larga parte sull'utilizzo di combustibili fossili così come il settore dei trasporti e del riscaldamento domestico (Catizzone et al., 2018). È possibile ricorrere a diverse strategie per la mitigazione delle emissioni di CO₂. In primo luogo, è necessario un progressivo abbandono dei combustibili fossili per favorire fonti di energia rinnovabile come le biomasse, il vento e il Sole. Il passaggio su larga scala è però frenato dalla necessità dell'apporto di importanti cambiamenti alle attuali infrastrutture energetiche che permetta l'integrazione e l'utilizzo di fonti di energia ecologiche in maniera efficiente e affidabile, nonché da motivazioni di carattere economico (Das et al., 2018; Roy et al., 2018).

Una seconda strategia consiste nella cattura e nello stoccaggio o utilizzo dell'anidride carbonica. La cattura e sequestro del carbonio (CCS) è un processo attraverso il quale il gas, prodotto da grandi impianti di combustione o di produzione di materiali come cemento e acciaio, viene separato dagli altri gas e confinato in larghe formazioni geologiche evitando dunque la sua emissione nell'atmosfera. Tuttavia, questa soluzione si rivela costosa sia in termini economici che energetici oltre che temporanea in quanto l'anidride verrà confinata per una quantità di tempo limitato prima del suo ritorno nell'atmosfera (Allahyarzadeh-Bidgoli et al., 2022; Fan et al., 2018).

La cattura e il riutilizzo della CO₂ (CCU) invece ha catturato crescente attenzione grazie alla possibilità di trasformare ciò che ora è uno scarto in una risorsa per la produzione di prodotti ad alto valore aggiunto da utilizzare come combustibili ecologici o materia prima per altri processi. A questo scopo la comunità scientifica si è adoperata per la ricerca e lo sviluppo di metodi efficaci per la sua conversione utilizzando processi sostenibili alimentati da fonti di energia rinnovabile. Tuttavia, sono necessari ulteriori sforzi per poter applicare queste energie a livello industriale (Guzmán et al., 2021; Li et al., 2020; Xing et al., 2022).

Riduzione elettrochimica della CO₂

Tra le tecnologie precedentemente citate si è distinta la riduzione elettrochimica della CO₂ (EC CO₂R) grazie alla sua flessibilità, ai bassi costi e la possibilità di convertire energia elettrica dal carattere aleatorio in stabile energia chimica di facile accumulo. È un processo controllabile, conducibile a temperature e pressioni ambientali in soluzioni acquose, che prevede l'applicazione di un potenziale elettrico per la conversione chimica del gas. Tuttavia, l'anidride carbonica possiede una molecola triatomica poco reattiva e altamente

stabile a causa della sua elevata ossidazione (North, 2015). Questo rende l'EC CO₂R in fase liquida un processo piuttosto complesso che richiede lo scambio di numerosi protoni ed elettroni e l'utilizzo di un catalizzatore per il superamento delle elevate barriere energetiche per l'attivazione della molecola.

Attraverso la modifica dei parametri è possibile andare a selezionare i prodotti desiderati, anche se l'elevato numero di intermedi e prodotti di reazione limitano considerevolmente la selettività del catalizzatore. Tra i principali parametri vi è il potenziale applicato, esso influenza fortemente la selettività dei prodotti e il valore a cui inizia la reazione di riduzione si chiama potenziale di onset. Potenziali di riduzione più vicini allo zero indicano una maggiore facilità con cui la CO₂ viene ridotta sulla superficie del catalizzatore.

La differenza tra potenziale applicato e il potenziale di riduzione all'equilibrio è detta sovratensione, forza spingente della reazione chimica e indice dell'efficienza del processo (Li et al., 2020). Un altro utile parametro, che permette una rapida valutazione della selettività ed efficienza della produzione di un certo composto, è l'efficienza faradica data dal rapporto della carica effettivamente spesa nella riduzione chimica e la carica totale fornita, come descritto in **Equazione 2** (Woldu et al., 2022).

La densità di corrente invece rappresenta la velocità con cui gli elettroni fluiscono attraverso la superficie dell'elettrodo per unità di tempo. La morfologia del catalizzatore può significativamente variare questo parametro per questo è bene normalizzare la corrente rispetto all'area superficiale elettrochimica (ECSA), che rappresenta l'effettivo numero dei siti attivi utilizzati per lo scambio di elettroni e l'adsorbimento della CO₂ (Fan et al., 2018).

Per far sì che l'EC CO₂R diventi sufficientemente competitiva da essere applicabile a livello commerciali, oltre che lo sviluppo di catalizzatore altamente attivo, stabile e selettivo, è necessario raggiungere bassi potenziali, elevate densità di corrente come pure alte efficienze faradiche verso i prodotti desiderati (Rabiee et al., 2021)..

Anche la configurazione del sistema influenza le prestazioni del processo, in quanto può seriamente influire sul trasporto di massa dell'anidride carbonica nel mezzo di reazione. Diversi tipi di configurazione della cella elettrochimica sono raccolti in **Figura 4**. Tra i più semplici e utilizzati vi è la cella ad H che permette la separazione dei compartimenti catodico e anodico evitando quindi la re-ossidazione dei prodotti, anche se soffrono di basse densità di corrente. Tra i più recenti e promettenti, anche se più complesse, vi sono le celle a microflusso che permetterebbero di aggirare le limitazioni del trasporto di massa che condizionano gli elettroliti in bulk (Z. Sun et al., 2017; Xing et al., 2022). Gli elettroliti giocano un ruolo fondamentale, infatti sono i principali responsabili del trasporto della CO₂ verso la superficie dell'elettrodo e del trasporto di carica da un elettrodo all'altro. La composizione, concentrazione e tipo di ioni dell'elettrolita vanno a determinare le interazioni elettrostatiche, la capacità tampone, il pH e la disponibilità di donatori di protoni che sono tutti fattori che influenzano l'attività e la selettività del catalizzatore (Fan et al., 2018)

Gli elettroliti acquosi sono i più diffusi grazie alla possibilità di operare in condizioni più miti; tuttavia, essi soffrono della bassa solubilità dell'anidride carbonica in acqua (Nitopi

et al., 2019). L'ottimizzazione della cella elettrochimica e dell'elettrolita sono dunque un fattore cruciale per il raggiungimento di elevate prestazioni.

Infine, il catalizzatore è il principale fattore che influenza l'attività e la selettività del processo. I più studiati sono i catalizzatori metallici grazie all'importante capacità di coordinarsi con la CO₂ modificandone la struttura elettronica e la reattività. Sono suddivisibili in 4 classi, schematizzate in [Figura 5](#), e tra di essi si è distinto il rame grazie all'abilità di ridurre l'anidride in una grande varietà di prodotti fino a composti a più atomi di carbonio come l'etanolo, anche se a causa di ciò soffre di una bassa selettività (Hori et al., 1985).

Negli ultimi anni hanno fatto la loro comparsa e attratto molta attenzione catalizzatori a base di materiali carboniosi, cosiddetti metal-free, in quanto economici, abbondanti e disponibili in molteplici forme, dai nanotubi al diamante.

Carboni porosi per l'elettrocatalisi

Tra i catalizzatori a base di carbone si sono distinti i carboni porosi grazie alle loro morfologie uniche e controllabili. La struttura porosa gioca un ruolo cruciale nell'adsorbimento e nella diffusione della CO₂, oltre che introdurre importanti effetti di confinamento in grado di favorire la riduzione verso specifici prodotti piuttosto che altri (Duan et al., 2017; Tian et al., 2020).

Purtroppo, questo tipo di catalizzatori presenta attività catalitica trascurabile se non dopati, a questo scopo si ricorre all'introduzione di diversi eteroatomi nella struttura del carbone. Il dopante più diffuso è l'azoto che migliora la conduttività elettrica e introduce siti attivi attraverso la polarizzazione dei legami N-C, modificando così la distribuzione di carica e la simmetria di spin del materiale (F. Yang et al., 2021). L'azoto si può trovare sottoforma di diverse specie nel reticolo del carbone, rappresentate in [Figura 10](#).

L'ottenimento di una struttura porosa ordinata, ovvero uniforme in termini di forma, volume e dimensione dei pori è preferibile in quanto permette di ottenere proprietà più omogenee (Davis, 2002).

Un metodo di sintesi molto efficace per la sintesi di materiali porosi ordinati di varia morfologia è il templating. Questa tecnica prevede la riproduzione di un modello, detto template, e in base alle sue caratteristiche si può parlare di hard o soft templating. Nel caso dell'hard templating si utilizza un materiale solido, come silici o zeoliti mesoporose, che viene ricoperto con il precursore del carbone che in seguito alla sua conversione e alla rimozione del template darà un carbone con una struttura che è la replica inversa del modello. Questo metodo, tuttavia, può risultare tedioso a causa della necessità di sintetizzare in precedenza il template solido, per evitare ciò è possibile ricorrere all'utilizzo di tensioattivi o copolimeri a blocchi (come il Pluronic) cosiddetti templanti soft. Il principio è analogo all'hard templating con la differenza che il metodo soft si basa sull'autoassemblaggio di precursore e agente template e non sulla replica di una superficie tramite la sua copertura (Z. Yang et al., 2015). I due processi sono confrontati in [Figura 11](#).

Per la sintesi di carboni mesoporosi ordinati possono essere utilizzati diversi precursori come resine fenoliche, PAN o zuccheri. Tra le resine fenoliche un ottimo precursore sono

le resine termoindurenti dette dei resoli in quanto possiedono: (i) un elevato contenuto di carbonio nella loro struttura, (ii) un elevato numero di gruppi ossidrilici in grado di formare legami idrogeno con il templante e (iii) la capacità di stabilizzare la mesostruttura durante la rimozione del templante attraverso reticolazione. Per l'introduzione di azoto nella struttura si può invece ricorrere a diverse molecole contenenti azoto, come la cianoguanidina ad esempio, una molecola molto reattiva che contiene il 66 % di azoto e può agire come agente reticolante nel caso delle resine fenoliche.

I resoli appartengono alla famiglia dei precursori che danno vita ai cosiddetti hard carbons, carboni con un ridotto livello di grafittizzazione dovuto alla difficoltà della formazione di piani grafittici ordinati e impilati in maniera uniforme, durante la pirolisi, causata dai forti legami introdotti dalla reticolazione. La differenza tra la struttura della grafite e di questo gruppo di carboni è rappresentata in [Figura 12](#).

Obiettivo della tesi

Nel contesto appena introdotto, l'obiettivo di questa tesi si pone nella sintesi e caratterizzazione di un carbone mesoporoso ordinato dopato con azoto come catalizzatore per la riduzione elettrochimica della CO₂. I campioni sono stati sintetizzati attraverso un metodo di soft templating, con autoassemblaggio promosso dall'evaporazione del solvente (EISA), utilizzando come precursori di carbone e azoto un resole a basso peso molecolare e cianoguanidina, mentre come agente templante il copolimero a blocchi Pluronic F127. Tre differenti trattamenti di carbonizzazione sono stati utilizzati per investigarne il ruolo nelle proprietà del carbone, mentre per l'indagine dell'effetto della morfologia della struttura porosa sono stati utilizzati dei carboni CMK-3 come confronto. Infine, è stato introdotto del rame nella struttura del carbone nel tentativo di migliorarne le prestazioni.

Metodi, materiali e procedure sperimentali

Il processo di sintesi dei carboni mesoporosi ordinati può essere riassunto in cinque passaggi fondamentali. Il primo passaggio prevede la sintesi del precursore del carbone attraverso la polimerizzazione di fenolo e formaldeide in rapporto molare 1 a 2 in ambiente basico. In questo modo si ottiene un migliore controllo del peso molecolare del resole. Una volta ottenuto il precursore si procede con la formazione di un complesso tensioattivo/resole e il suo autoassemblaggio in una mesostruttura ordinata promosso dall'evaporazione del solvente. In questo caso si è utilizzato Pluronic F127 come tensioattivo ed etanolo e acqua come solvente in concentrazioni tali da ottenere un'organizzazione a simmetria esagonale (gruppo spaziale p6mm). È in questo passaggio che inoltre viene aggiunta la cianoguanidina. Dopo la rimozione nel solvente si stabilizza la mesostruttura ottenuta attraverso un trattamento di reticolazione causando l'indurimento della resina. Dopodiché la resina viene frantumata e macinata per essere pronta per l'ultima fase del processo. Gli ultimi passaggi, il quarto e il quinto, sono la rimozione del template e la conversione del precursore in carbone. Possono essere eseguiti in unico trattamento, in particolare la polvere della resina è stata prima calcinata per la rimozione del Pluronic e in seguito carbonizzata. I diversi prodotti ottenuti durante le fasi del processo di sintesi sono visibili in [Figura 13](#). In questo caso i tre diversi trattamenti

utilizzati T0, T1 e T2, riportati in **Tabella 4** e **Figura 14**, prevedevano la stessa temperatura e mantenimento per la calcinazione mentre le rampe termiche e le temperature di carbonizzazione erano diversi. In questo modo sono stati ottenuti tre diversi campioni: CND_T0, CND_T1, CND_T2. Il campione con rame Cu_CND_T0 è stato sintetizzato macinando nitrato di rame e mischiandolo alla polvere della resina dopodiché è stato trattato in maniera analoga a quanto detto sopra. Inoltre, seguendo la stessa rampa di calcinazione del trattamento termico T0 è stato trattato del nitrato di rame per verificarne la completa decomposizione e studiare la differenza di prestazione rispetto al campione Cu_CND_T0. Quest'ultimo campione è stato nominato CuO. La lista completa dei campioni è raccolta in **Tabella 5**.

I campioni così ottenuti sono stati successivamente caratterizzati mediante adsorbimento di azoto per quanto riguarda l'area superficiale e la distribuzione della dimensione dei pori. Analisi XRD sono state effettuate per lo studio del grado di grafitizzazione e la natura del rame presente nei campioni, mentre attraverso spettroscopia Raman è stato investigato il loro grado di ordine. L'analisi attraverso FESEM ha permesso l'ottenimento di dati riguardo alla morfologia delle particelle dei campioni. Infine, analisi XPS sono state effettuate per la determinazione della composizione superficiale e le specie azotate presenti. L'attività catalitica è stata studiata attraverso diverse tecniche. Ciclo voltammetrie, sia in azoto che anidride carbonica, sono state eseguite per ottenere informazioni riguardo a picchi di riduzione e il comportamento del catalizzatore nel mezzo di reazione. Le analisi LSV hanno permesso invece l'ottenimento di informazioni riguardo la potenziale di onset. Infine, l'attività catalitica è stata valutata tramite crono potenziometrie e crono amperometrie in elettrolita saturato con anidride carbonica.

Le analisi sono state condotte adottando un sistema a tre elettrodi composto da una cella H con come anodo una spira in Pt, come elettrodo di riferimento un elettrodo Ag/AgCl (3M, NaCl) e un catodo composto da un supporto su cui è stato depositato il catalizzatore. In **Figura 20** è rappresentato schematicamente il sistema appena descritto.

Come supporti per la deposizione del catalizzatore sono stati utilizzati dapprima un RDE (in **Figura 21b**) e successivamente fogli di fibre di carbone intrecciate per aumentare l'area degli elettrodi. In base al substrato sono state adottati inchiostri di diversa composizione per la deposizione.

I test preliminari sono stati eseguiti utilizzando un sistema RDE (RRDE-3A), poiché è più semplice ed evita limitazioni di trasferimento di massa. Le analisi successive hanno impiegato elettrodi funzionanti con un'area più ampia e un carico del catalizzatore maggiore, rispettivamente di 1 cm² e 1 mg cm⁻². Gli elettrodi sono stati realizzati depositando il materiale del catalizzatore su un substrato di carta carbone con l'obiettivo di aumentare la produttività oltre che l'area.

Risultati e discussione

Adsorbimento di azoto

Le analisi della resina prima del trattamento termico hanno confermato l'assenza di porosità e il ruolo positivo del trattamento di carbonizzazione nella sua formazione.

I campioni CND_T0, CND_T1, CND_T2 hanno mostrato isoterme di adsorbimento dell'azoto di tipo IV, in **Figura 23a**, tipiche dei materiali mesoporosi. L'area superficiale maggiore è di $460 \text{ m}^2 \text{ g}^{-1}$ appartenente a CND_T0, mentre CND_T2 mostra quella minore pari a $328 \text{ m}^2 \text{ g}^{-1}$, i risultati delle analisi sono raccolti in **Tabella 6**. Questo suggerisce che maggiori temperature di carbonizzazione portino a una diminuzione nell'area superficiale.

La condensazione capillare nella regione delle basse pressioni relative (0,4-0,6) indica una distribuzione della dimensione dei pori stretta (Uddin Ahmad et al., 2019), ulteriormente confermata dalla distribuzione della dimensione dei pori ottenuta nella **Figura 23b**.

I campioni CND_T0 e CND_T2 mostrano un ciclo di isteresi di tipo H1 indice della presenza di una struttura mesoporosa ordinata, il campione CND_T1 presenta invece un ciclo di isteresi di tipo H3 dato dalla presenza di adsorbimento nella regione ad alte pressioni relative. Questo effetto è probabilmente dovuto alla presenza di vuoti interparticellari e non esclude la presenza di una struttura mesoporosa ordinata per il campione CND_T1.

Il campione CND_T0 è l'unico non mostrare adsorbimento per pressioni relative ($P/P^0 \geq 0.8$) che potrebbe significare una struttura puramente mesoporosa, imputabile alla minore velocità di riscaldamento del trattamento T0 (Ayinla et al., 2019; Z. Yang & Mokaya, 2008).

La distribuzione dei pori è centrata a 3.7 nm, i diversi campioni presentano lievi variazioni nella dimensione media dei pori ascrivibili ai diversi trattamenti termici utilizzati. In generale si può dire che la variazione della dimensione dei pori è attribuibile a quanto la struttura del carbone si restringe durante la carbonizzazione. Basse velocità di riscaldamento o temperature più elevate determinano un restringimento inferiore e pori più piccoli (Z. Yang & Mokaya, 2008). In ogni caso, le velocità di rampa termica utilizzate in questo lavoro sono state sufficientemente basse da ottenere carboni mesoporosi ordinati. Il trattamento termico T0 ha prodotto carbone mesoporoso con l'ordine migliore, una superficie maggiore e possibilmente privo di micropori poiché offre un processo di carbonizzazione più omogeneo.

Diffrazione dei raggi X

Gli spettri XRD ad alti angoli mostrano la presenza di domini cristallini in quasi tutti i campioni. Invece, come già anticipato, non è stato possibile eseguire XRD a piccoli angoli ($2\theta < 10$) e, quindi, ottenere informazioni sull'ordine e la simmetria della struttura mesoporosa con questa analisi. Tuttavia, considerando la procedura utilizzata per sintetizzare i campioni è plausibile ipotizzare una mesostruttura ordinata con simmetria esagonale (p6mm).

Dai profili XRD raccolti in **Figura 24** si nota che i campioni CND_T0 e CND_T2 mostrano delle gobbe per angoli 2θ di 24° e 43° associati ai piani della grafite (002) e (101) (J. Ni et al., 2013), che suggeriscono una struttura in parte cristallina al contrario di quella del campione CND_T1 completamente amorfo. La gobba associata ai piani (002) è traslata verso minori angoli rispetto al picco della grafite, questo è dovuto al fatto che i forti legami di reticolazione ostacolano la formazione di piani grafiteici ordinati impilati in maniera uniforme durante il processo di carbonizzazione della resina fenolica (Lee et al., 2021). Si ha quindi una struttura cristallina simil grafiteica come rappresentato in **Figura 12**. In

generale si può dire temperature più elevate e/o velocità di rampa inferiori promuovono una maggiore cristallinità e anche una maggiore grafitizzazione.

Le analisi sui campioni con rame, riportate in **Figura 25**, hanno invece evidenziato la presenza di picchi corrispondenti a rame metallico cristallino per quanto riguarda il campione Cu_CND_T0 oltre che alla presenza di gobbe come per i carboni senza metallo.

Lo spettro del campione CuO ha confermato la composizione dell'ossido di rame, in particolare i picchi ottenuti appartengono alla fase monoclina con simmetria spaziale Cc. L'assenza di picchi di nitrato conferma la dispersione dell'azoto nel carbonio.

FESEM e EDS

Differenti caratteristiche delle particelle dei carboni mesoporosi CND sono riportate in **Figura 26**. In generale le particelle hanno mostrato una distribuzione eterogenea, superfici rugose e a tratti escoriate possibilmente dovute della macinazione (Mangi et al., 2022). La risoluzione e l'ingrandimento dello strumento non sono state sufficienti per indagare la struttura porosa.

Quanto appena detto si può dire anche delle particelle di Cu_CND_T0, che però a differenza di CND_T0 mostrano numerose strutture nanometriche sulla superficie. Si presume che derivino dall'aggregazione di atomi di rame durante il trattamento termico per formare aggregazioni cristalline di forma irregolare densamente impaccati a causa di una grande quantità di rame introdotta.

Anche CuO mostra una distribuzione di taglia delle particelle ampia con particelle che variano da centinaia di nanometri a unità di micrometri. In particolare, si sono notate sia particelle irregolari, formate dall'aggregazione cristalli prismatici e nano lamelle, che particelle a forma di "fiore" formate da nano lamelle disposte in maniera opportuna (Khan et al., 2013). Quanto appena detto è visibile in **Figura 27**.

Le analisi EDS hanno invece evidenziato un'elevata presenza di rame nel campione Cu_CND_T0, superiore a quanto si era supposto durante la preparazione del campione. Una possibile spiegazione è una disomogeneità del campione portata dalla coalescenza e aggregazione del rame favorita dal processo di sintesi, che prevedeva la miscelazione di due polveri micrometriche. Come previsto, CuO mostra solo ossigeno e rame con un rapporto atomico da 1 a 1. La **Tabella 7** raccoglie i risultati dell'EDS.

Per i campioni senza metallo invece sarebbe meglio fare riferimento alle analisi XPS per la poiché i picchi di carbonio e azoto potrebbero sovrapporsi a causa della loro vicinanza non consentendo una precisa identificazione del contenuto di azoto con EDS (Massardier et al., 2001).

Spettroscopia Raman

La spettroscopia Raman è stata utilizzata per studiare il grado di ordine e il contenuto di azoto dei carboni dopati con azoto. I dati risultanti sono riassunti nella **Tabella 8** mentre gli spettri sono mostrati in **Figura 28**.

Per valutare il grado d'ordine delle strutture del carbone sono di particolare interesse le bande D e G, che in questo caso sono identificate come picchi rispettivamente a 1330 cm^{-1} e circa 1560 cm^{-1} . Il rapporto tra l'intensità di queste due bande ($I_{D/G}$) è una misura dell'ordine della struttura del carbone, dipende da molteplici fattori come il grado di grafitizzazione, la presenza di eteroatomi, e in caso di carboni porosi anche sulla presenza di pori. I campioni CND_T0 e CND_T2 mostrano indici inferiori a CND_T1, $I_{D/G}$ pari rispettivamente a 1,65, 1,68 e 2,03, suggerendo un grado di ordine maggiore.

La differenza nel grado di ordine è attribuibile alla cristallinità e al contenuto di azoto. A temperature più elevate o velocità di riscaldamento minori portano una maggiore cristallinità (grado di ordine) con micro-cristalliti di tipo grafítico, come evidenziato anche dall'analisi XRD.

L'introduzione di azoto, invece, provoca una distorsione locale dei legami nei fogli grafítici a causa delle differenze nella massa atomica, nei raggi e nell'elettronegatività tra atomi di carbonio e azoto portando a un aumento del disordine (J. Wu et al., 2015). In particolare, l'analisi della banda I C-N ha evidenziato una maggiore presenza di azoto per il campione CND_T1.

Spettroscopia fotoelettronica a raggi X

La **Tabella 9** mostra la composizione superficiale dei campioni in percentuale atomica. Le analisi hanno confermato l'assenza di metalli nei campioni CND, mentre nel caso di Cu_CND_T0 e CuO è stato rilevato solo rame (Na escluso, presente in meno del 2 % eventualmente residuo dovuto al processo di sintesi).

Per tutti i campioni è stata rilevata una bassa concentrazione di azoto. La concentrazione atomica di N è pari a 2,4 e 2,5% per i campioni CND_T0 e CND_T2 rispetto al 10,6% per il campione CND_T1, confermando l'andamento riscontrato con l'analisi della spettroscopia Raman. Il contenuto di azoto è fortemente influenzato dal trattamento di carbonizzazione, il minor tempo e temperatura del trattamento T1 sembrerebbero responsabili di una maggiore incorporazione di azoto nella struttura del carbone.

La deconvoluzione del picco N1s (vedi **Figura 30**) ha evidenziato la presenza di diverse specie di azoto, i picchi a 398,5, 400,1 e 401 eV corrispondono rispettivamente all'azoto piridinico, pirrolico e grafítico. L'azoto piridinico è la specie prevalente per tutti i campioni con il 52,2% in CND_T1, notevolmente superiore al 39,8% e 37,7% rispettivamente per CND_T0 e CND_T2. Le percentuali delle specie di azoto per i vari campioni sono raccolte in **Tabella 10**.

L'analisi degli spettri C1s suggerisce una maggiore presenza di specie di carbonio sp^2 si riscontra nel caso dei carboni con un grado di ordine maggiore, mentre il campione CND_T1 mostra un numero maggiore di difetti simili a sp^3 . Gli spettri C1s di CND_T0 e CND_T2 sono quasi sovrapposti mentre quello CND_T1 devia maggiormente, il numero di difetti o atomi di C legati ad atomi diversi, come l'azoto, aumenta da T0 a T1, a conferma di quanto detto nei paragrafi precedenti.

L'introduzione del rame nel carbonio CND_T0 ha comportato un aumento del contenuto di azoto fino al 100%, ottenendo un 4,4%at per il campione Cu_CND_T0.

Dagli spettri C1s e N1s, mostrati in **Figura 32**, è possibile escludere diversi legami tra Cu e N (Cu-N_x) o con altri atomi. L'introduzione del rame non porta alla comparsa di nuovi picchi legati a specie di azoto diverse da quelle presenti nei campioni metal-free mentre dagli spettri di carbonio appare un aumento trascurabile dell'ordine in caso di Cu_CND_T0.

Infine, l'analisi XPS dell'ossido di rame ha mostrato un'elevata presenza di carbonio adventizio nelle forme C-C, C-O-C e O-C=O, probabilmente dovuta alla contaminazione in seguito all'esposizione all'atmosfera. Inoltre, ha confermato che la composizione del campione di CuO è principalmente di ossido di rame (88% Cu(II)) mentre il resto è una miscela di rame metallico e Cu(I), la cui formazione è probabilmente dovuta all'esposizione a raggi X durante la prova (C.-K. Wu et al., 2006).

Comportamento elettrochimico dei carboni dopati con azoto

Prove preliminari di attività catalitica con sistema RDE

In base alla caratterizzazione fisico-chimica eseguita, i campioni CND_T1 e CND_T2 sono stati sottoposti a dei test elettrochimici preliminari. L'obiettivo era quello di valutare il comportamento di due campioni con valori differenti in termini di area superficiale, grado di ordine e contenuto di azoto (specialmente di gruppi piridinici). La **Tabella 11** riassume i risultati della caratterizzazione per questi due campioni.

In entrambi i campioni, le curve CV eseguite durante il gorgogliamento di CO₂ raggiungono densità di corrente inferiori rispetto a N₂. In generale, significa una maggiore attività catalitica nei confronti di HER rispetto alla CO₂RR. Tuttavia, potrebbe anche essere dovuto all'adsorbimento di molecole di anidride carbonica sulla superficie del carbonio che inibisce la corrente per potenziali superiori a -0,8 V vs RHE (Pérez-Rodríguez et al., 2017).

Non ci sono picchi di riduzione evidenti, e la voltammetria ciclica di CO₂ mostra densità di corrente massime intorno a 60 mA cm⁻² per entrambi i catalizzatori. In generale, CND_T1 raggiunge densità di corrente più elevate a parità di potenziale, come notato nel caso della voltammetria ciclica sotto azoto in **Figura 33**. La spiegazione potrebbe risiedere nel maggior contenuto di azoto del campione CND_T1 che ha effetti positivi sulla conducibilità dei carboni amorfi (Ray et al., 2014).

Sulla base dei risultati LSV, si è deciso di testare l'attività di riduzione della CO₂ con un CP, mostrato in **Figura 35**, fornendo una corrente corrispondente a un potenziale di -1,6 V vs RHE, un potenziale maggiormente negativo per garantire l'attività catalitica. Il mantenimento di questa densità di corrente ha richiesto un potenziale leggermente superiore nel campione CND_T1, che ha conservato una corrente costante nelle due ore, possibile indice di maggiore stabilità.

Gli unici prodotti gassosi rilevati sono stati idrogeno e monossido di carbonio, la cui evoluzione durante la CP è mostrata in **Figura 36a**, mentre le corrispondenti efficienze faradiche sono mostrate in **Tabella 12**. Per entrambi i campioni, è stata trovata una produzione di idrogeno maggiore rispetto alla CO con efficienze faradiche del 70% per CND_T1 e 79% per CND_T2, che conferma la debole attività catalitica verso CO₂RR. La

concentrazione dei prodotti gassosi è stata approssimativamente costante per la durata della prova, suggerendo la stabilità di entrambi i catalizzatori per due ore.

Nel caso dei prodotti liquidi, CND_T1 ha prodotto maggiormente isoproporpanolo con un FE del 2% e una produttività di $1,3 \text{ mmol h}^{-1} \text{ g}^{-1}$ mentre per CND_T2 è stato il formiato con una produttività pari a $19 \text{ mmol h}^{-1} \text{ g}^{-1}$ e un FE del 3%. In ogni caso, la produttività dei prodotti liquidi era molto bassa ed è raccolta nella **Tabella 13**.

Sulla base dei risultati ottenuti nonostante la debole attività catalitica nei confronti della CO_2 , il campione CND_T1 sembrerebbe propenso a produrre prodotti a più atomi di carbonio. Infatti, il catalizzatore CND_T1 sembra favorire la formazione dell'intermedio $^*\text{COOH}$, che evolve verso il CO e poi verso i prodotti C_{2+} attraverso il meccanismo di dimerizzazione.

Attività elettrochimica degli elettrodi in carbon paper

Le prove sono state eseguite a potenziali più bassi poiché sembrerebbero favorire la produzione di idrocarburi, alcoli e acidi organici (Pérez-Rodríguez et al., 2017) attraverso lo sblocco di vie di reazione altrimenti svantaggiate termodinamicamente. Inoltre, i campioni CMK-3 sono stati testati per accertare l'effetto delle diverse strutture mostrate in Figura 9. L'attività elettrocatalitica del campione di ossido di rame (CuO) è stata studiata per comprendere le possibili sinergie tra i materiali di Cu_CND_T0 .

In generale, le densità di corrente sono inferiori a quelle registrate durante le prove preliminari RDE a causa delle diverse resistenze di carica e trasporto di massa e della maggiore area degli elettrodi (1 cm^2 per elettrodi in carta carbone vs $0,1962 \text{ cm}^2$ per RDE). È importante ricordare che la fabbricazione di un elettrodo più grande non garantisce una densità di corrente uniforme.

L'attività catalitica per CO_2 è stata quindi studiata utilizzando una misurazione CA, mostrata in **Figura 39**. In generale, si ottengono densità di corrente molto basse a potenziali bassi, tra $0,02$ e $0,15 \text{ mA cm}^{-2}$ per $-0,4 \text{ V}$ vs RHE e $0,04 \text{ mA cm}^{-2}$ per CND_T0 e $0,8 \text{ mA cm}^{-2}$ di CuO a $-0,6 \text{ V}$ vs RHE. CuO e CND_T1 mostrano le maggiori densità di corrente ad alti potenziali, pari rispettivamente a 7 e 6 mA cm^{-2} , suggerendo una maggiore attività catalitica e conduttività, seguite dal campione Cu_CND_T0 con $2,5 \text{ mA cm}^{-2}$.

I campioni CND_T0 e CMK-3 mostrano invece le densità di corrente più basse a tutti i potenziali raggiungendo valori massimi a -1 V vs RHE, pari a $0,8 \text{ mA cm}^{-2}$ per CND_T0 e CMK-3-750 e $1,3 \text{ mA cm}^{-2}$ per CMK- 3-600.

Le efficienze di faradiche dei prodotti gassosi sono mostrate nella **Figura 40** e riassunte nella Tabella 15, mentre le produttività dei prodotti liquidi sono raccolte nella **Tabella 16** e in **Figura 41**.

I campioni privi di metalli (CND) hanno solo idrogeno come prodotto gassoso, contrariamente a quanto visto nella misurazione RDE. Potrebbe essere riferito ai potenziali minori applicati che favorirebbero la ritenzione dell'intermedio $^*\text{CO}$ e la sua ulteriore riduzione. Aumentando il potenziale applicato, hanno mostrato una maggiore selettività verso la produzione di idrogeno, raggiungendo una FE vicino al 100% a -1 V vs RHE, nel caso di CND_T1.

I campioni contenenti rame invece hanno prodotto anche CO anche a FE basse (<10%), in particolare nel caso di CuO la produzione di CO sale con il potenziale fino ad alti potenziali -1V vs RHE, dove diminuisce. Il campione Cu_CND_T0 invece produce CO solo ad alti potenziali con una FE del 2%. Il campione con rame Cu_CND_T0 è più cataliticamente attivo rispetto alla controparte priva di rame CND_T0 in termini di HER e riduzione di CO₂.

In generale, per tutti i campioni a base di carbone, si osserva che la produzione di prodotti gassosi aumenta all'aumentare del potenziale applicato. Questa tendenza non è vera per il campione a base di CuO, che mostra efficienze più elevate a potenziali intermedi suggerendo una diversa attività catalitica rispetto ai campioni a base di carbone.

Per quanto riguarda i prodotti liquidi, le efficienze faradiche sono elencate nella **Figura 42** e nella **Tabella 17**. Tutti i campioni hanno efficienze faradiche relativamente basse. In generale, la massima produttività è stata raggiunta per la produzione di formiato. I campioni CMK-3 hanno mostrato una produttività molto bassa rispetto agli altri campioni. Il campione CND_T0 ha mostrato un'elevata selettività verso il formiato con una FE del 72,6%, mentre la produzione di prodotti C₂⁺ è trascurabile. L'introduzione di un maggiore contenuto di azoto (CND_T1) o rame (Cu_CND_T0) è favorevole al miglioramento dell'attività catalitica e della selettività verso prodotti più ridotti come metanolo ed etanolo anche se il prodotto principale rimane il formiato. Cu_CND_T0 mostra la più alta efficienza faradica per l'etanolo, pari al 18%.

L'elevata selettività verso HCOO⁻ del campione CND_T0 rispetto al campione CND_T1, così come la differenza in termini di contenuto di azoto, potrebbe essere attribuita alla cristallinità del carbone. I risultati ottenuti sia con le prove preliminari in RDE che in queste prove suggerirebbero che un aumento della cristallinità favorisca la selettività e l'efficienza verso il formiato.

Il campione CuO si è mostrato selettivo verso la formazione di formiato con lieve produzione di alcoli. Il campione CMK-3-600 ha mostrato una maggiore selettività verso gli alcoli, forse favorita dal maggior contenuto di gruppi piridinici, al contrario di CMK-3-750 che si è mostrato maggiormente selettivo verso il formiato. Nonostante la minore produttività, i campioni CMK-3 hanno mostrato efficienze faradiche maggiori rispetto al campione CND_T1; in particolare, il campione CMK-3-600 mostra la maggiore efficienza per il metanolo, pari a 8,7%.

La spiegazione potrebbe risiedere nelle diverse strutture del carbone. I carboni con una struttura formata da canali cilindrici (CND) hanno una maggiore produttività e conducibilità; invece, la curvatura dei pori della struttura dei nanorods limiterebbe la formazione di prodotti, e il basso numero di punti di contatto tra le barre si traduce in una minore conduttività che porta a correnti più basse, e quindi una minore quantità di carica utilizzata che va di pari passo mano a bassa produttività. Una struttura a pori cilindrici sarebbe quindi più favorevole alla riduzione della CO₂.

L'applicazione del rame sulla struttura del carbone favorisce la selettività verso prodotti a più atomi di carbonio; tuttavia, CuO è stato sintetizzato per calcinazione senza introdurre caratteristiche che potrebbero migliorarne l'attività catalitica.

Si ricorda infine che le efficienze faradiche sono state mediate sulle tre CA e, quindi, non riconducibili ad un unico potenziale. Sulla base di ciò, non è possibile verificare se

l'applicazione di potenziali minori favorisca la produzione di idrocarburi, alcoli e acidi organici. Sulla base dei risultati ottenuti, non è possibile suggerire quali siano i percorsi di reazione o i siti attivi nella riduzione della CO₂.

Conclusioni

In sintesi, l'utilizzo di un soft template e del metodo EISA ha consentito la sintesi di carboni mesoporosi dopati con azoto con canali cilindrici ordinati. I trattamenti con velocità di riscaldamento e temperatura finale inferiori sono risultati favorevoli per la produzione di campioni con un grado di ordine più elevato, un'area superficie più elevata e una struttura porosa più ordinata, mentre velocità di riscaldamento leggermente più elevate hanno consentito una maggiore incorporazione di azoto a scapito del grado di ordine. Un trattamento del primo tipo si è rivelato benefico anche nell'attività catalitica, portando a raggiungere un'efficienza faradica del 72% per la produzione di formiato. Pertanto, una struttura più ordinata e una mesoporosità uniforme sarebbero vantaggiose per l'aumento della selettività verso CO₂RR.

Una maggiore incorporazione di azoto ha mostrato effetti positivi nell'aumentare la conduttività e la produttività dei prodotti a più atomi di carbonio anche se le efficienze rimangono basse.

Il processo di macinazione ha avuto successo nell'introdurre rame metallico sotto forma di aggregati cristallini sulla superficie delle particelle di carbone, con un ruolo positivo in termini di riduzione della CO₂ in alcoli e per il raggiungimento di densità di corrente maggiori. Allo stesso tempo non sono stati rilevati gruppi Cu-N_x. Il campione di rame ha mostrato la maggiore selettività verso l'etanolo con un'efficienza del 18%.

Infine, l'indagine della struttura ha rivelato che una struttura di canali cilindrici ordinati porta a una maggiore produttività, attività catalitica e densità di corrente rispetto a una struttura di nanobarre interconnesse, probabilmente a causa delle migliori interazioni date dalla diversa curvatura dei pori.

In generale, tutti i campioni hanno mostrato densità di corrente basse e una maggiore selettività verso HER, specialmente ad alti potenziali. Al contrario, la riduzione della CO₂ potrebbe essere favorita a bassi potenziali. In ogni caso, in questo studio, non è stata verificata l'origine dell'attività catalitica né il ruolo del potenziale applicato nella selettività del catalizzatore.

In ogni caso, i campioni sintetizzati non soddisfacevano i requisiti necessari per l'idoneità all'applicazione commerciale.

1. Introduction

Earth has entered a new geological epoch; anthropogenic climate changes are one of the biggest threats to species already struggling to survive on an extensively human-transformed planet. In the last century, the rapid and unprecedented progress in both science and technology has led to a considerable improvement in the quality of life. Consequently, the world population has undergone exponential growth, especially in the last 50 years, tripling its number and increasing.

The excessive exploitation of fossil fuels as a source of energy to satisfy the world energy needs has released a tremendous amount of carbon dioxide (CO₂) in the atmosphere altering the carbon cycle so heavily that it would need millennia to return to an equilibrium (Guzmán, Russo, et al., 2021). Amongst greenhouse gasses, CO₂ is not the most powerful. However, it is the one emitted in greater quantities in the atmosphere, therefore is recognised as the main responsible for global warming and many other environmental issues such as glaciers melting, sea-level rise, extreme weather events, extinction of species, ocean acidification and acid rains (Duan et al., 2017). Carbon dioxide concentration reached the critical level of 415.2 ppm in 2019, which is considerably higher than the safety limit of 350 ppm (K. Zhao & Quan, 2021), leading to an average increase of 1.1 °C of the global temperature in 2017 and, according to the Intergovernmental Panel on Climate Change (IPCC) this will increase of 0.2 °C per decade.

Hence, limiting further global temperature increases are extremely important to avoid severe heatwaves and extreme precipitations, drought, loss of species, and extinction. In fact, as stated by the National Aeronautics and Space Administration (NASA), an increase of 1.5 °C will cause a sea level rise of 0.1 meters; around 6% of insects, plants and vertebrates will see their geographical range reduced by more than half and the population will face increased risks of heat-related illness, mortality and poverty. All these phenomena worsen with greater temperature increases.

According to the International Energy Agency (IEA), global energy production still heavily relies on carbon combustibles with 37 % from coal (responsible for 30 % of the global CO₂ emissions), 23 % from natural gas while only the 26 % from renewable energy sources.

The main sources of CO₂ emissions are human activities that involve burning fossil fuels such as power plants, house heating and vehicles, and cement, steel production, and animal farms contribute (Catizzone et al., 2018). For this reason, several countries agreed and have given greater importance to sustainable development to mitigate these effects, reduce CO₂ emissions and avoid more dangerous consequences by entering into agreements such as the Paris Agreement. The aim is to reduce CO₂ emissions by at least half of the current value and to avoid the average global temperature to increase to a maximum of 2 °C by 2050 (Catizzone et al., 2018).

Many strategies can be implemented to alleviate CO₂ concentration. However, it has to be done without affecting the energy needs of the growing population. Firstly, improving the combustion efficiency would reduce the consumption of fossil fuels while shifting to more sustainable and green energy sources such as wind, biomass, hydroelectric, and geothermal energies which emit fewer greenhouse gasses slowing down global warming.

Serious drawbacks restrain the large-scale switch from fossil fuels to greener energy sources. Major changes to the current transport sector energy infrastructure are required, such also further technological improvements to develop an efficient energy storage system that would allow the integration of renewable and distributed energy sources in the distribution network. Furthermore, these changes arise political issues especially in all those areas with large fossil fuels availability. (Das et al., 2018; Roy et al., 2018). Other possibilities to reduce CO₂ would be storage or its utilisation (see [Figure 1](#)).

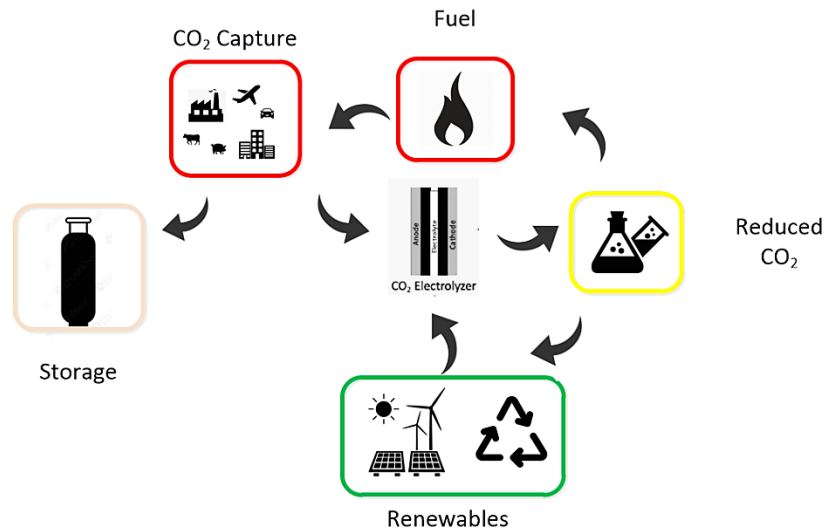


Figure 1: Carbon capture storage and utilisation cycle. It is inspired by (Eren & Özkar, 2021).

Carbon Capture Storage (CCS) implies capturing the CO₂ before it is released into the atmosphere to be stored or used. CCS is a noteworthy solution for all hard-to-abate industrial fields in which emissions are related to the production process, such as for chemical, cement and steel plants. CCS can be used complementary to other strategies to mitigate CO₂ emissions by separating and transporting the gas to be used in a variety of applications or to be stored in a place different from where it was produced, isolating the gas from the atmosphere for long terms (de Coninck & Benson, 2014), as shown in [Figure 2](#).

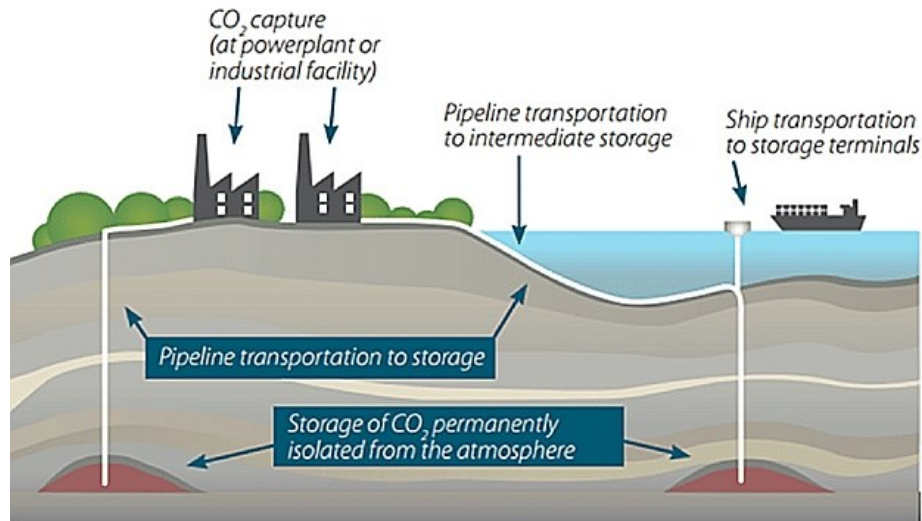


Figure 2: Basic principle of Carbon capture storage. Courtesy of Piyush Choudhary and Clicinnovation.

However, even if the high efficiency of this technology allows, in theory, to capture 90 % of the CO₂ produced by the plant, the energy required to achieve that value would reduce considerably the energy efficiency of the plant by 7-15 % creating an energy penalty. The most expensive part of the process is the capture of the CO₂, around 75 % of it incurs the capture technology (Yadav & Mondal, 2022).

Large geological or marine formations are generally used for storage. However, the impact this has on life forms is still unknown; it is believed that CO₂ eventually will slowly be released back into the atmosphere (A. Liu et al., 2020). Therefore, this strategy is still nonrecoverable, energy-intensive and expensive, thus needing further studies and optimisation. It is not sufficient as a solution (Allahyarzadeh-Bidgoli et al., 2022; Fan et al., 2018).

Carbon capture utilisation (CCU) has attracted many attentions thanks to the possibility of mitigating CO₂ emissions by transforming combustion waste into a variety of compounds to harvest and utilise as a green renewable fuel or raw material for other processes. To this purpose, the scientific community has sought effective methods to transform CO₂ into chemicals of economic value. Thus, nowadays there are different alternatives to convert CO₂ such as mineralisation, or photocatalytic, biochemical, thermocatalytic, electrocatalytic reactions (K. Zhao & Quan, 2021). The common aim is to obtain value-added products from CO₂ with the assistance of a catalyst and an energy source such as the sun, heat or electricity. However, the major challenge is developing proficiency systems with a high active stable catalyst with great selectivity. Among the alternatives to transform CO₂, the electrochemical reduction of CO₂ (EC CO₂R) is particularly attractive due to the compatibility of the process with renewable energy systems, minimisation of environmental impact, low cost, high energy density storage and potentially high flexibility. Nevertheless, further efforts are required to bring that technology to an industrial level (Guzmán, Russo, et al., 2021; L. Li et al., 2020; Xing et al., 2022).

2. Electrochemical reduction of CO₂

Electrolysis is based on using an electric current to induce a non-spontaneous reaction in an electrolytic cell; however, the only use of an electric current is not sufficient for the reduction reaction of CO₂ (CO₂RR). Carbon dioxide is a transparent gas at room temperature, neither flammable nor explosive. The linear structure and the high oxidation of this small triatomic molecule (see [Figure 3](#)) give high stability and low chemical reactivity, mainly determined by the double bonds between carbon and oxygen (North, 2015). Therefore, a catalyst is needed to help overcome the thermodynamic and kinetic barriers necessary for CO₂ activation and so its reduction.

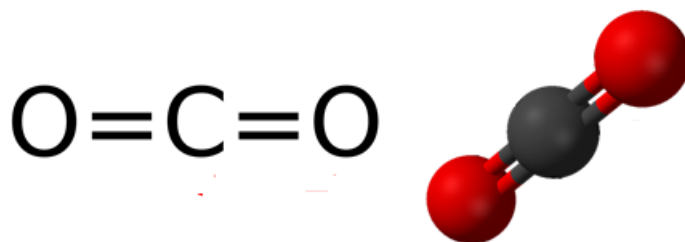


Figure 3: Carbon dioxide molecule, with carbon atoms in black and oxygen atoms in red.

As mentioned before, the EC CO₂R seems very promising for several reasons. It is a controllable process, so by adjusting external parameters such as the catalyst, the electrolytes or the applied voltage, the product distribution can be changed and tuned, making even possible to obtain highly desirable C_n compounds with higher energy densities, such as methanol, ethylene or ethanol (L. Li et al., 2020). The electrochemical process does not require high temperature or pressure; the whole process can be performed at low temperature, ambient pressure, and neutral pH. It is possible to conduct the reaction in an aqueous solution and therefore is unnecessary to feed hydrogen (H₂) for the carbon hydrogenation since it is generated in situ by hydrolysis. Moreover, it is compatible with the renewable energy system allowing to convert the intermittent electric energy to stable chemical energy (Fan et al., 2018; A. Liu et al., 2020; K. Zhao & Quan, 2021). In the case of gaseous products, such as CO, the downstream separation processes require few energy since the separation from the aqueous solution is spontaneous. However, liquid products entail high costs for downstream separation. It is the major disadvantage of in liquid-phase electrocatalytic configuration.

It is worth noting that the EC CO₂R in liquid-phase configuration is a rather complex multi-electron process that involves multiple protons/electrons transfer steps at the interface of the triple-phase boundary (gas-liquid-solid) and numerous intermediate compounds, which makes the selectivity of the catalyst a great challenge (A. Liu et al., 2020; Z. Sun et al., 2017). This technology is held back not only by the lack of a robust and active catalyst but also by the low solubility of CO₂ in aqueous media, resulting in low mass transport, thus allowing only small current densities and limiting the conversion rate. Therefore, the study and the smart design of the cell configuration, the electrodes, the electrolytes, and the local conditions around the catalytic sites are critically important, alongside developing a stable, active, and selective catalyst. (Xing et al., 2022). Furthermore, the CO₂RR competes with the water (H₂O) reduction when performed in

aqueous media. The typical reaction at the anode is the oxygen evolution reaction (OER), while at the cathode, the formation of CO₂ reduction products competes with the hydrogen evolution reaction (HER). It can be attributed to the fast kinetics of the reaction with a lower number of exchanged protons and electrons (2H⁺ and 2e⁻), see **Equation 1** (Eren & Özkar, 2021).



Although the presence of protons (H⁺) is necessary for the CO₂ hydrogenation, it is important to suppress as much as possible the HER with a catalyst with the proper interaction to increase the efficiency and favour the formation of the CO₂R intermediates over the formation of hydrogen (J. Li et al., 2021).

In summary, the EC CO₂R processes still need further experimental analysis and theoretical efforts to improve the design of the cell and optimise the activity, selectivity and stability of the catalyst, to enhance the mass transport and charge within the system. (Fan et al., 2018).

2.1 Electrocatalyst efficiency and other factors influencing the process

The main parameters useful for the comparison and the evaluation of the catalyst performance and the CO₂ electroreduction process are shown in the following.

A crucial parameter is the onset potential. The term onset potential indicates the lowest potential at which the reduction reaction occurs and generates a noticeable quantity of products. In the case of HER, this information can be obtained by the current density curve versus the potential since the reduction reaction causes a rapid increase of the current density at the onset potential. For CO₂RR, the take-off of the current not always coincides with the onset potential.

The applied potential is one of the parameters that greatly affects the selectivity of products. According to L. Li et al., more positive potentials, closer to zero, are more favourable as it indicates that the reduction reaction occurs more easily on the catalyst surface

Another important parameter is the overpotential, which refers to the difference between the potential in the working condition (any current intensity) and the potential at the equilibrium (the theoretical standard potential). The overpotential is the index of the driving force with which the reaction is catalysed; it measures cell efficiency. The lower it is, the lower the amount of energy to supply for the CO₂ reduction reaction. Since the CO₂RR is greatly affected by the working potential, it is always better to report it with other parameters for comparison and evaluation (L. Li et al., 2020).

A useful parameter to rapidly evaluate the selectivity and efficiency towards generating a certain product is the faradaic efficiency (FE), shown in **Equation 2**. It is a measure of the fraction of the total current consumed to yield a certain product; its increase may suggest an increase in selectivity towards that product.

$$FE_{product} = \frac{nZF}{Q} \cdot 100 \quad \text{Equation 2}$$

The FE can be calculated from the ratio between the the truly spent on CO₂ reduction towards a specific product and the total charge supplied over the process (Q). The real charge spent for reduction can be calculated by multiplying the number of moles (n) by the Faraday constant (96 485 C mol⁻¹) and the number of electrons (Z) necessary for the reduction (Woldu et al., 2022).

The current density (J) denotes the rate with which electrons flow through the electrode per unit of the surface of the catalyst and time. The catalyst structure and morphology can significantly vary this value. It can provide a incorrect description of the catalytic behaviour. The current should be normalised by the electrochemical surface area (ECSA), which is the effective number of available electrocatalytic sites used for the exchange of electrons and the adsorption of CO₂ and intermediates. It can be very useful in case of high roughness of the electrode. The ECSA can be obtained through different methods such as the hydrogen underpotential deposition method, double layer capacitance measurements or integration of cyclic voltammetric peaks (Fan et al., 2018).

The turnover frequency (TOF) refers to the reaction turnover, so the number of reactants converted per time and active site of the catalyst. The TOF can be considered a measure of the catalyst efficiency. It is an intrinsic property of the material since it is not affected by the catalyst area. However, the TOF is not easily determinable for several materials, for example, its calculation for carbonaceous material is very difficult or impossible due to the ambiguous nature of their active sites and the lack of reliable characterisation techniques to count them (Kozuch & Martin, 2012; L. Li et al., 2020).

Finally, a last useful parameter to consider is the Tafel slope. The Tafel plot can be obtained from the logarithm of the current density versus the overpotential. In general, a catalyst with a lower slope has a better performance. The Tafel slope can be useful to determine the reaction mechanism since it can be used to identify the rate-limiting step of the reaction, although on its own is not sufficient. Moreover, comparing different Tafel slopes is not advisable due to the frequent discrepancies in the experimental procedures (Fan et al., 2018; Woldu et al., 2022).

In any case, numerous improvements are still needed for CO₂ electro-reduction to become competitive enough to be applied on an industrial level. As mentioned before, for a practical application, it is necessary to achieve low overpotentials, high current density ($J \geq 200 \text{ mA cm}^{-2}$), high efficiencies and selectivity towards specific products and long-term operational stability (at least 20 000 hours) (Rabiee et al., 2021).

2.2 *Electrochemical cell configurations*

The electrochemical cell configuration can greatly affect the overall performance of EC CO₂R, influencing the mass transport and the solid-gas-liquid interface design.(Xing et al., 2022). The one-compartment(see [Figure 4a](#)) and H-cell (see [Figure 4b](#)) are the most traditional three-electrode configuration systems utilised as a platform for improvements. However, researchers have moved their attention towards continuous flow cells (Guzmán, Russo, et al., 2021). The electrodes are a cathode (often a support (Gas diffusion layer, GDL) on which is deposited the catalyst), an anode (for example Pt-based electrodes such as a Pt coil or similar) and a reference electrode (e.g., Ag/AgCl saturated electrodes).

In the traditional one-compartment cell, all the electrodes are in a common reaction medium. This configuration can suffer from re-oxidation of the products more than other configurations. On the contrary, H-type cells have two compartments to separate the cathodic from the anodic chamber by using an ion-exchange membrane, such as a Nafion 117 membrane. The anode-cathode separation prevents the back reaction of high energy products and allows different electrolytes for the anode and the cathode to optimise the working conditions.

The cathode compartment can be directly connected to a gas chromatograph to analyse the gaseous products in situ. However, these configurations greatly resent low mass transport of CO₂, which has to dissolve in the bulk electrolyte and then slowly diffuse to the surface of the catalyst, and so of relatively low current densities (Z. Sun et al., 2017; Xing et al., 2022) Microfluidic flow cells, such as gas-diffusion electrode (GDE) cells, shown in **Figure 4c**, have been developed and used recently for CO₂RR. This configuration is often used for better control of the three-phase boundary where the reaction occurs and to improve the mass transport of CO₂, allowing it to possibly reach high current densities (> 200 mA cm⁻²) with low overpotentials (Xing et al., 2022). It is a three-electrode system in which an ion exchange membrane separates the cathode compartment from the anode one. The CO₂ is fed directly to the backside of the cathodic electrode, increasing the concentration on the catalyst surface. It significantly reduces the thickness of the diffusion layer through the electrolyte with respect to the H-cell configuration, accelerating CO₂ diffusion to the electrode and improving mass transport. It is also possible to deposit one or both electrodes on the membrane to reduce as much as possible the distance between the two electrodes. As shown in **Figure 4d**, that system is called membrane electrode assembly (MEA) (Rabiee et al., 2021). The electrolytes are fed to the cell through peristaltic pumps in a laminar flow parallel to the electrodes minimising pH variation (Z. Sun et al., 2017). The local pH in the electrode plays a dual role: (i) inducing the production of carbonate and bicarbonate species (HCO₃²⁻, CO₃²⁻), which tend to decrease the pH and reduce the concentration of CO₂ at the catalytic surface, and (ii) affects the surface coverage by adsorbed intermediates, suppressing the HER because of a limited transport of protons (Guzmán, Zammillo, et al., 2021).

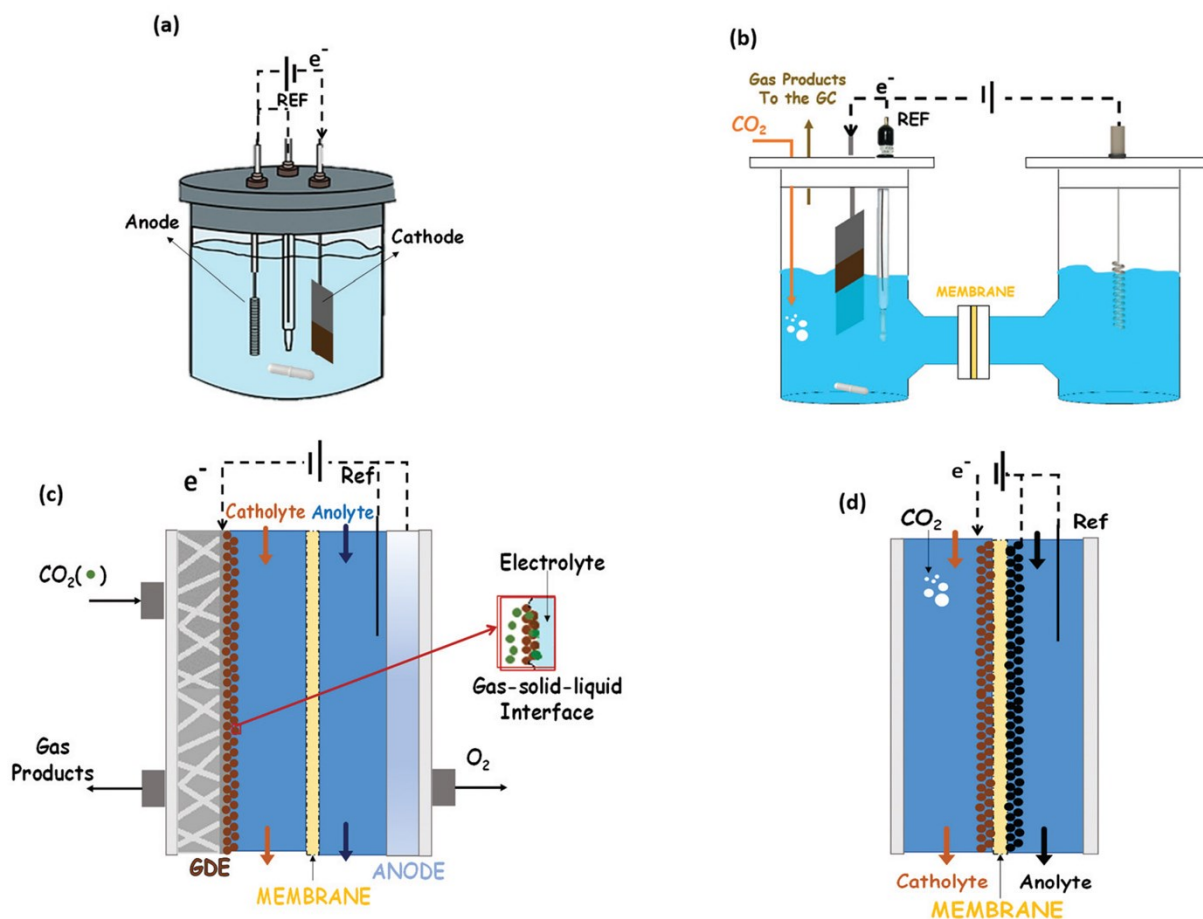


Figure 4: Schematic concepts of 3-electrode (a) traditional cell, (b) H-cell, (c) Gas Diffusion Electrode cell and (d) Membrane Electrode Assembly for electrochemical CO_2 reduction reactions. Adjusted from (Guzmán, Russo, et al., 2021).

2.3 Electrolytes solutions

Electrolytes play a fundamental role in electrochemical cells. They are responsible for the charge transport from one electrode to another, and, in the case of the EC CO_2 R, they are also responsible for the diffusion of CO_2 to the surface of the electrode. The choice of the electrolyte is crucial. Electrostatic interactions, buffer capacity, pH and availability of protons donors are all factors that influence the activity and selectivity of the catalyst, decisive for the reduction pathways. Those are affected by the composition, concentration and type of ions of the electrolyte (Fan et al., 2018). For this reason, it is also important to have no impurities (metallic or organic) in the electrolyte to avoid poisoning or alteration of the catalyst sites and performance (Nitopi et al., 2019).

Liquid electrolytes are commonly used for cells operating at low temperatures and ambient pressure, but it is possible to use solid electrolytes, such as zirconia or yttrium if the operating conditions require it (Z. Sun et al., 2017).

Alkaline electrolytes are advantageous as they have lower ohmic resistance and the high presence of OH^- ions favour the suppression of HER and the reduction of CO_2 towards multi-carbon products over C1 products. However, weakly acidic or neutral solutions are

typically used as electrolytes. In this regard, Na or K salts such as KCl, NaHCO₃ or KHCO₃ are typically used as electrolytes (Nitopi et al., 2019; Rabiee et al., 2021).

Most of the EC CO₂R studies have been performed in KHCO₃ solution thanks to its buffering properties, which help to maintain a neutral pH in the bulk and to the fact that it can act as a source of protons, as well of CO₂ even if the latter hypothesis requires further studies to be validated (Nitopi et al., 2019).

The different cations and anions can strongly influence the reduction of CO₂. The cations adsorbed at the electrode-electrolyte surface can modify the superficial interaction and the adsorption properties. For example, cations of alkane metals have shown positive effects in stabilising adsorbed species or reaction intermediates and the adsorption of CO₂ (Fan et al., 2018). On the other hand, the anions could determine the selectivity of the products also based on their concentration. During the electroreduction process, OH⁻ are generated, which can be neutralised by some anionic species such as HCO₃⁻; therefore, in the presence of anions with weak buffering capacity, such as solutions of diluted KCl or KHCO₃, for example, can favour high local pH; therefore, the reduction towards multi-carbon products. On the contrary, the presence of electrolytes with strong buffering capacities, such as more concentrated KH₂PO₄ or KHCO₃ solutions (e.g., 0.2 M), favours HER and C1 products (Nitopi et al., 2019; G. Wang et al., 2021).

Aqueous solutions are less toxic and easier to handle with the possibility of extracting most of the products without too much difficulty. However, they suffer from the low solubility of CO₂ in water which results in low current densities (Rabiee et al., 2021). To overcome that problem, it is possible to use organic electrolytes or ionic liquids, even if they are generally more expensive and toxic (Fan et al., 2018).

2.4 *Electrocatalyst materials*

Over the years, starting from the 1960s, numerous electrocatalysts for CO₂RR have been studied and classified according to various perspectives. A first distinction can be made between homogeneous and heterogeneous catalysts.

In homogeneous catalysis, the catalyst and the reactants are dissolved in the same phase, and the reduction reaction takes place on the surface of the catalyst. An example of homogeneous catalysts are organic or metal-organic molecules dissolved in electrolytic solutions. This of catalysts quickly captured wide attention thanks to their excellent selectivity towards CO₂ reduction and the possibility of minimising environmental disturbance. Despite the advantages, most homogenous catalysts are outperformed by heterogeneous catalysts and have numerous disadvantages such as high cost, toxicity, low stability and difficult separation from the products. Therefore, homogeneous catalysts were considered unsuitable for large-scale application, and the focus of research shifted to heterogeneous catalysts, which turned out to be more efficient, greener and easier to synthesise (Dongare et al., 2021; Eren & Özkar, 2021).

In the case of the heterogeneous catalysis, the catalyst and the reactant are in different phases; roughly speaking, the catalyst is in contact with a reaction mixture, and the reaction takes place at the interface between the two.

The catalyst, which is the cathode material in the electrochemical cell, is the main feature affecting the catalytic activity and the selectivity of CO₂ electrocatalysis. The

electrocatalytic activity is defined as the ability to increase the speed of a reaction by modifying its kinetic, while selectivity indicates the ability to direct the reaction towards a specific product. On the other hand, a low selectivity is unfavourable as it results in lower efficiency towards a specific product and higher costs of separation of the different products (Ling et al., 2021).

The activity of the heterogeneous catalyst is largely determined by the chemisorption binding strength between the reactants and the catalyst surface active sites. Thus, it is crucial that the reactant molecules, in this case, CO₂ molecules, bind to the catalyst surface with real chemical bonds to undergo a re-organisation of the electronic configuration and therefore acquire reactivity. On the contrary, it is equally important that the products have a sufficiently weak interaction to desorb and not poison the catalyst while, according to the Sabatier principle, the reaction intermediates binding energies should be just right, neither too high nor too low (Y. Li & Sun, 2016).

As already mentioned, CO₂ is a very stable and chemically inert molecule. For its reduction is necessary to break highly energetic carbon-oxygen double bonds (750 kJ mol⁻¹ for each C=O) (J. Li et al., 2021). However, a key factor for the CO₂RR is the susceptibility to the nucleophilic attack of the C=O bond, which makes CO₂ prone to coordinate with metals. Coordination is crucial as it allows the electronic and geometric rearrangement of the molecule, responsible for the radical change in its reactivity and activation (North, 2015). For this reason, metallic catalysts occupied a large part of the CO₂ electrocatalysis scene.

Based on what just said, a second distinction can be made in the metallic or metal-free catalyst.

The former group can be further divided into mono-metals, multi-metals/alloys, supported, doped and metal-organic frameworks (MOF) (Dongare et al., 2021). A class largely studied is the mono-metals, which consist mainly of transition metals whose activity relies on the presence of the d-band. In fact, the chemisorption of an adsorbate on the metal surface is given by the interaction of the *sp* and *d* states of the latter. However, since the contribution of the *sp* is almost the same for all those metals, the interaction is mainly determined by the d-band. It originates the linear scalar relationship, which is the correlation between the reaction energies of the different intermediates on the reaction surface.

The correlation is due to the impossibility to vary the binding energy towards a specific intermediate without changing the binding energy towards everyone, as it is determined by the d-band of the metal, with consequent difficulties in controlling and modulating the adsorption and desorption of the intermediates (Y. Li & Sun, 2016).

After a large study in 1985, Hori et al. proposed a first classification based on the selectivity of the different metals identifying four groups, as shown in [Figure 5](#).

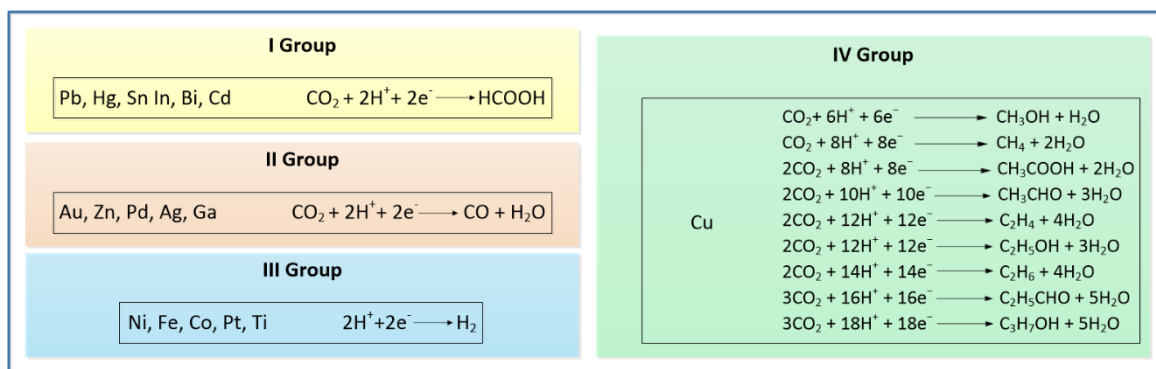


Figure 5: Schematic representation of selectivity-based classification of mono metallic catalyst.

The first (I) group is composed of the metals that yield formic acid (HCOOH), such as lead (Pb) and tin (Sn), thanks to their interactions with the oxygen of the CO₂ molecule, exposing the carbon to protonation.

To the second (II) group belong metals such as gold (Au), zinc (Zn), silver (Ag) and palladium (Pd). Second group metals are selective towards carbon monoxide (CO) thanks to the low binding energy, which facilitates desorption, and the carbon atom binding to the metal, promoting oxygen protonation.

Iron (Fe), nickel (Ni), titanium (Ti), cobalt (Co) and platinum (Pt) are included in the third (III) group. On these metals, HER prevails thanks to a strong interaction with CO.

Copper (Cu), IV group, is the only metal that has shown the ability to reduce the CO₂ towards multicarbon (C₂₊) products thanks to the moderate CO adsorption energy. Cu can yield up to 16 different gaseous and liquid products, including CO, HCOOH, methane (CH₄), methanol (CH₃OH), ethanol (CH₅OH) and ethylene (C₂H₄). However, this results in low selectivity (L. Li et al., 2020; Ling et al., 2021; Zhong et al., 2021).

To improve the performance of the metal catalyst, various strategies have been studied, such as introducing defects and/or supports, the control of surface, morphology and facets, and the modification of the composition.

The composition of the catalyst can be changed using different heteroatoms, such as boron (B), nitrogen (N), sulfur (S), other metals or through oxidation treatment.

Multi-metal catalysts obtained combining metals with synergic effects, such as Cu/Zn, Ag/Cu, Au/Cu, have shown excellent catalytic properties compared to pure metals. The electronic structure is easily modulated by changing the composition, the degree of order or even by engineering the interfaces (J. Li et al., 2021; Ling et al., 2021).

Another interesting possibility is using a support, for example incorporating metal nanoparticles (NPs) on a conductive material. The incorporation promotes the stabilisation of the NP, limiting agglomeration and material saving. The support material must be suitable for electrocatalysis and, therefore, must be conductive. Among the most used substrates are carbonaceous materials, such as graphene, Vulcan carbon, nanotubes (CNT), porous carbon and graphitic carbon. In this case, the selectivity can be controlled by tuning the structure, the morphology, the surface area and/or the pore dimension (Dongare et al., 2021). Some examples of the metal class of catalysts are listed in [Table 1](#).

Table 1: Examples of metallic catalyst for CO₂RR. Current densities are reported in absolute value.

Electrocatalyst	Cell	Electrolyte	Product	Faradaic efficiency	Current density	Reference
Anodized Ag	Two comp. *	0.5 M NaHCO ₃	CO	90 % @ -0.8 V vs RHE	0.9 (J _{co}) mA cm ⁻²	(K. Sun et al., 2016)
Cu-In	Two comp.	0.1M KHCO ₃	CO	85 % @ -0.6 V vs RHE	1 mA cm ⁻²	(Rasul et al., 2015)
S-modified Cu	Two comp.	0.1 M KHCO ₃	HCOOH	80% @ -0.8 vs RHE	–	(Shinagawa et al., 2018)
Sn(S)/Au	Custom	0.1 M KHCO ₃	HCOOH	93% @ -0.75V vs RHE	55 mA cm ⁻²	(X. Zheng et al., 2017)
Pd ₈₃ Cu ₁₇ aerogel	H-Cell	[Bmim]BF ₄ and water	CH ₃ OH	80% @ -2.1 V vs Ag/Ag+	31.8 mA cm ⁻²	(Lu et al., 2018)
Cu ₂ O/ZnO on carbon paper	Flow cell	0.5 M KHCO ₃	CH ₃ OH	17.7 % @ -1.3 vs Ag/AgCl	10.64 mA cm ⁻²	(Albo et al., 2015)
Pt @adenine-rGO	–	0.1 M KNO ₃	CH ₃ OH	85 % @ -0,3 V vs Ag/AgCl	0.5 mA cm ⁻²	(Alinajafi et al., 2018)
CuS@Ni Foam	H cell	0.1M KHCO ₃	CH ₄	73 % @ -1.1 V vs RHE	7.3 mA cm ⁻²	(Z. Zhao et al., 2017)
Cu ₂ Ag ₃ NP on poly-Fe(vbpy) ₃ (PF ₆) ₂	–	0.5 M KHCO ₃	CH ₃ COOH	21.2 % @ -1.33 V vs RHE	–	(Y. Wang et al., 2017)
Electrodeposited Cu	Three comp.	0.1 M KClO ₄	C ₂ H ₄	48.1 % @ -1.4 V vs NHE	5 mA cm ⁻²	(Hori et al., 1989)
Cu(B)	H-cell	0.1 M KCl	C ₂ H ₄	52 % @ -1.1 V vs RHE	70 mA cm ⁻²	(Zhou et al., 2018)
MC-CNT/CoO	H cell	0.5 M KHCO ₃	C ₂ H ₅ OH	60.1 % @ -0.32 V vs RHE	5.1 mA cm ⁻²	(J. Du et al., 2020)
Cu on C-NanoSpikes	–	0.1M KHCO ₃	C ₂ H ₅ OH	63 % @ -1.2 V vs RHE	1.5 mA cm ⁻²	(Song et al., 2016)
Ag _{0.14} /Cu _{0.86}	Flow cell	1 M KOH	C ₂ H ₅ OH	41 % @ -0.67 V vs RHE	10 mA cm ⁻²	(Y. C. Li et al., 2019)
Cu-Bi MOF	Flow cell	0.5 M KHCO ₃	C ₂ H ₅ OH	28.3 % @ -0.21V vs RHE	20 mA cm ⁻²	(Albo et al., 2019)

*comp. is the abbreviation of compartments.

Recently, catalysts classified as metal-free have attracted great attention for the EC CO₂R. Those are composed of carbonaceous materials, some examples of which are shown in [Table 2](#).

Carbon-based materials are particularly interesting thanks to their excellent thermal and electrical conductivity, great mechanical stability, versatility, low costs and great availability. Furthermore, the HER onset potential is higher than one of metals, which could favour the catalytic activity towards CO₂ reduction products and suppress the evolution of hydrogen (K. Zhao & Quan, 2021). However, pristine carbonaceous materials are electrochemically inert, even when immersed in an aqueous solution and applied negative potential, both in their *sp*² and *sp*³ forms (L. Li et al., 2020).

To introduce catalytic sites, it is possible to dope the carbon matrix with heteroatoms capable of modifying the electronic structure of neighbouring atoms and thus modifying the charge and the spin densities. Boron and nitrogen are typical doping atoms, which have similar dimensions to the C atoms, but also S can be used.

Since the catalytic activity is determined by the active centres generated by the doping and not by the d-band as for metals, carbon materials are not affected by the limitations of the linear scale relationship.

Carbonaceous materials offer a variety of structures capable of determining catalytic properties, such as quantum dots, nanotubes, graphene, porous carbon and diamond, which can be synthesised through various processes (J. Wu et al., 2019).

Carbon-based catalysts have proved to be able to electrochemically reduce CO₂ into many different products from CO to C₂₊ oxygenates, similar to copper and in some cases even with comparable efficiencies, although they do not share his limited selectivity. The interaction energies with the adsorbates can be tuned through the rational engineering and design of their structures (Ling et al., 2021; K. Zhao & Quan, 2021).

A final class of catalysts worth mentioning are the single-atom catalysts (SACs), born from the combination of the best qualities of both carbon and metal catalysts, of which some examples are shown in [Table 2](#).

The SACs consist of carbonaceous catalysts in which, in addition to doping with heteroatoms, one or more metals are introduced, through many different methods such as CVD, ALD, ball milling or impregnation, to disperse them atomically (Gawande et al., 2020).

Several studies have confirmed the interaction between the metal and the support, the metal atoms (M) coordinate in moieties with the heteroatoms of the carbon, i.e., M-N₄. It also has been confirmed that these interactions significantly had impacted both catalytic activities and stability. In fact, atomically dispersed metal atoms exhibit different behaviour in the CO₂RR with respect to their bulk counterpart due to the tuning effect of the carbon on the electric structure and charge distribution of metal atoms. For example, there are cases in the literature in which it is reported that SAC Fe-N-C shows high efficiencies towards CO when iron bulk is selective towards hydrogen (Jia et al., 2022; S. Liang et al., 2021; K. Zhao & Quan, 2021).

The use of single atoms, in addition to favour the catalytic activity, promote greater use of the metal as all the atoms are exposed and are reaction sites, unlike the bulk material where

only surface atoms participate in the reaction. One of the major drawbacks is the high thermodynamic instability of the individual atoms, partially compensated by the support, which leads them to aggregation during storage or under working conditions, limiting the catalyst stability. Besides, to avoid aggregation and favour a homogeneous dispersion, the concentrations are limited, generally equal to or less than 5% wt (Gawande et al., 2020; Jia et al., 2022).

Table 2: Interesting carbon-based and single-atom catalyst. Current densities are in absolute value.

Electrocatalyst	Cell	Electrolyte	Product	Faradaic efficiency	Current density	Reference
F-doped carbon	–	0.1 M KHCO ₃	CO	90% @ –0.62 V vs RHE	0.24 mA cm ⁻²	(J. Xie et al., 2018)
NSP doped carbon	Flow cell	1 M KOH	CO	98.5% @ –1 V vs RHE	186 mA cm ⁻²	(F. Yang et al., 2021)
B, N co-doped mesoporous carbon	H-cell	0.1 M KHCO ₃	CO	95% @ –0.55 V vs RHE	2.7 mA cm ⁻²	(Ma et al., 2021)
Ni-N-C	Two comp.	0.1 M KHCO ₃	CO	85 % @ –0.78 V vs RHE	–	(Ju et al., 2017)
Fe-N-C				65 % @ –0.55 V vs RHE	–	
N-doped graphene	Two comp.	0.5 M KHCO ₃	HCOOH	73% @ –0.84 V vs RHE	7.5 mA cm ⁻²	(H. Wang et al., 2016)
B-doped diamond	Flow cell	0.5 M KCl	HCOOH	94.7 %	2 mA cm ⁻²	(Natsui et al., 2018)
NiSn-APC	H-Cell	0.5 M KHCO ₃	HCOOH	86.1 % @ –0.82 V vs RHE	20.8 mA cm ⁻²	(W. Xie et al., 2021)
CuSAs/TCNFs	Two comp.	0.1 M KHCO ₃	CH ₃ OH	44% @ –0.9 V vs RHE	93 mA cm ⁻²	(H. Yang et al., 2019)
NGM/CP	H-cell	[Bmim]BF ₄	CH ₄	93.5 % @ –1.4 V vs SHE	1.42 mA cm ⁻²	(X. Sun et al., 2016)
CoPC@Zn-N-C	Flow Cell	1 M KOH	CH ₄	18.3 @ –1.24 vs RHE	44.3 mA cm ⁻²	(Lin et al., 2020)
Cu-SA/NPC	Two comp.	0.1 M KHCO ₃	CH ₃ COCH ₃	36.7% @ –0.36 V vs RHE	–	(K. Zhao et al., 2020)
N-doped carbon (c-NC)	H-cell	0.1 M KHCO ₃	C ₂ H ₅ OH	77% @ –0.56 V vs RHE	1 mA cm ⁻²	(Song et al., 2017)
B,N-doped nanodiamond	H-cell	0.1 M NaHCO ₃	C ₂ H ₅ OH	93.2% @ –1 V vs RHE	–	(Y. Liu et al., 2017)
Cu-N-C	Two comp.	0.1 M CsHCO ₃	C ₂ H ₅ OH	55% @ –1.2 V vs RHE	–	(Karapinar et al., 2019)

2.5 Desired products and Reaction Pathways

As aforementioned in the previous sections, the EC CO₂R is a complex process that involves many reaction intermediates, the breaking of C=O bonds and the formation of C–H, C–C, O–H bonds through the exchange of many electrons (e⁻) and protons (H⁺). Depending on the system used, different products can be formed. **Table 3** shows the different products that can be obtained from the EC CO₂R, whose reaction paths are still the subject of debate and study.

Table 3: Table of products with half-cell reaction. Potential referred to standard hydrogen electrode (SHE) at pH 7 in aqueous solution. Data from (K. Zhao & Quan, 2021).

Product	Half-cell reaction	Potential (V vs SHE)
CO ₂ ⁻	CO ₂ + e ⁻ → CO ₂ ⁻	-1.9
Hydrogen (H ₂)	2H ⁺ + 2e ⁻ → H ₂	-0.42
Carbon monoxide (CO)	CO ₂ + 2H ⁺ + 2e ⁻ → CO + H ₂ O	-0.53
Formic acid (HCOOH)	CO ₂ + 2H ⁺ + 2e ⁻ → HCOOH	-0.61
Formaldehyde (CH ₂ O)	CO ₂ + 4H ⁺ + 4e ⁻ → HCOH + H ₂ O	-0.48
Methanol (CH ₃ OH)	CO ₂ + 6H ⁺ + 6e ⁻ → CH ₃ OH + H ₂ O	-0.38
Methane (CH ₄)	CO ₂ + 8H ⁺ + 8e ⁻ → CH ₄ + 2H ₂ O	-0.24
Acetic acid (CH ₃ COOH)	2CO ₂ + 8H ⁺ + 8e ⁻ → CH ₃ COOH + 2H ₂ O	-0.30
Acetaldehyde (CH ₃ CHO)	2CO ₂ + 10H ⁺ + 10e ⁻ → CH ₃ CHO + 3H ₂ O	-0.35
Ethylene (C ₂ H ₄)	2CO ₂ + 12H ⁺ + 12e ⁻ → C ₂ H ₄ + 4H ₂ O	-0.34
Ethanol (C ₂ H ₅ OH)	2CO ₂ + 12H ⁺ + 12e ⁻ → C ₂ H ₅ OH + 3H ₂ O	-0.33
Ethane (C ₂ H ₆)	2CO ₂ + 14H ⁺ + 14e ⁻ → C ₂ H ₆ + 4H ₂ O	-0.27
Propanal (C ₂ H ₅ CHO)	3CO ₂ + 16H ⁺ + 16e ⁻ → C ₂ H ₅ CHO + 5H ₂ O	-0.32
Propanol (C ₃ H ₇ OH)	3CO ₂ + 18H ⁺ + 18e ⁻ → C ₃ H ₇ OH + 5H ₂ O	-0.32

The first step of EC CO₂R is the activation of the molecule, which requires a very high negative redox potential (-1.9 V vs SHE). However, the use of a proper catalyst, capable of stabilising the intermediate radical CO₂⁻ through the formation of reaction bonds, allows the reduction can occur at less negative redox potentials (Birdja et al., 2019).

It should be remembered that the adsorption energies between the various intermediates and the surface of the catalyst depending on various factors such as the nature of the catalyst and the product under consideration, the electrolyte, the pH and the overpotential.

In general, the reaction paths are formulated based on theoretical DFT calculations and measurements of the reaction intermediates thanks to in situ characterisation techniques. Despite that, detailed reaction paths for some products are not yet fully known (K. Zhao & Quan, 2021).

The simplest products are CO and HCOOH for which only two electrons and protons are needed and whose possible reaction paths are shown in **Figure 6**.

The initial interaction between the catalyst and the corresponding intermediate decides the formation of one rather than the other. Specifically, HCOOH originates through the hydrogenation of the intermediate $*\text{OCHO}$ obtained through the rearrangement and hydrogenation of the CO_2 molecule adsorbed on the surface catalyst, which is the rate-limiting step of the reaction.

Instead, the path for CO formation consists of coupled electron and proton transfer for the hydrogenation of adsorbed CO_2 into the intermediate $*\text{COOH}$ and then its dehydrogenation in aqueous solutions (Zhong et al., 2021).

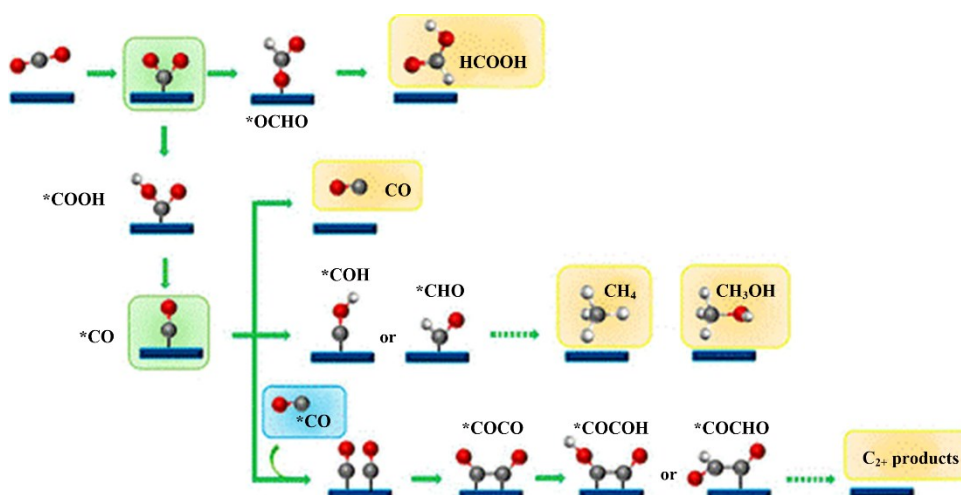


Figure 6: CO and HCOOH pathways and schematic pathways for methane, methanol and C_{2+} products. Adjusted from K. Zhao & Quan, 2021.

Other two relevant more reduced C_1 products are methane and methanol. Methane requires a greater number of electrons/protons than methanol, specifically 8, while in the case of methanol, they are 6.

Figure 7 shows a possible path for forming these products on polycrystalline copper.

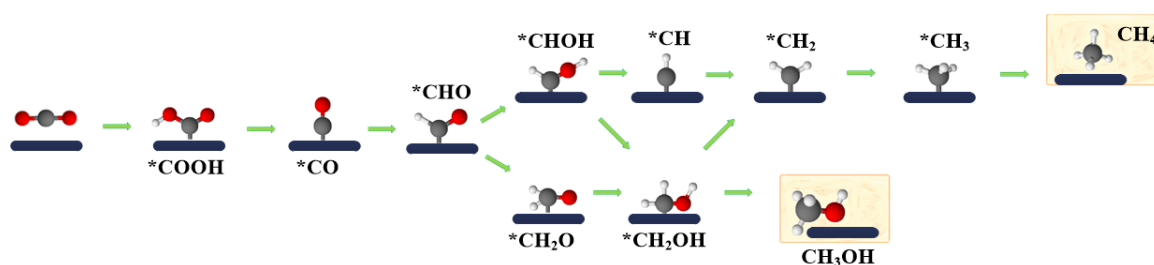


Figure 7: Examples of pathways on copper for methane and methanol. Reaction pathways from (Cheng et al., 2015; X. Liu et al., 2019).

The reaction pathway involves the hydrogenation of $*\text{CO}$ into $*\text{COH}$ or $*\text{CHO}$. Several studies on copper-based catalysts have shown that the formation of the intermediate $*\text{CHO}$ is more favourable since both the carbon and the oxygen atom interact with the catalyst

surface and therefore require the overcoming of a lower energy barrier (Y. Li et al., 2021; X. Wei et al., 2021).

For methane, the reduction continues with progressive hydrogenation and dehydration. A possible reduction path results in $\text{CO}_2 \rightarrow \text{*COOH} \rightarrow \text{*CO} \rightarrow \text{*CHO} \rightarrow \text{*CHOH} \rightarrow \text{*CH}$ followed by a sequence of downhill steps from $\text{*CH}_2 \rightarrow \text{*CH}_3 \rightarrow \text{*CH}_4 \rightarrow \text{CH}_4$. Recent studies have revealed that this reaction is very influenced by the pH and the overpotential. In particular the rate-limiting step is $\text{*CHO} \rightarrow \text{*CHOH}$ at low overpotentials, while for high, it is $\text{*CO} \rightarrow \text{*CHO}$ (Nitopi et al., 2019; Zhong et al., 2021).

On the other hand, a possible reaction path is given by $\text{*CO} \rightarrow \text{*CHO} \rightarrow \text{*CH}_2\text{O} \rightarrow \text{*CH}_2\text{OH} \rightarrow \text{*CH}_3\text{OH}$ for methanol, which has been reported favourable on Cu (211) (S. P. Liu et al., 2017). However, in acid conditions on Cu (100), the formation of $\text{*CH}_2\text{O}$ is kinetically unfavourable compared to *CHOH therefore *CHOH is the common intermediate where the formation of methane or methanol is determined at low pH. The pathway would be then $\text{*CO} \rightarrow \text{*CHO} \rightarrow \text{*CHOH} \rightarrow \text{*CH}_2\text{OH} \rightarrow \text{*CH}_3\text{OH}$ and finally CH_3OH , but the barrier for $\text{*CHOH} \rightarrow \text{*CH}_2\text{OH}$ is slightly larger than the one for $\text{*CHOH} \rightarrow \text{*CH}$, and therefore, these conditions are unfavourable for methanol (Cheng et al., 2015).

More reduced multicarbon products start from the same intermediate *CO . CO is, therefore, one of the major products in the CO_2RR , and *CO is a key intermediate for the formation of C_1 and C_{2+} products. The catalyst binding energy with *CO intermediate should be sufficient to transform it into more reduced products further. Nevertheless, it does not have to be excessive to avoid catalyst poisoning (J. Li et al., 2021). Few catalysts have proved to be suitable for this purpose. The most reported and studied catalysts capable of converting CO_2 to C_{2+} products are copper-based catalysts. Other examples are NiGa, PdAu, NiP and doped carbon catalysts, although often not with the same efficiencies (Birdja et al., 2019).

The fundamental step that distinguishes the formation of C_{2+} products from the others is dimerisation by coupling two carbon atoms with the consequent formation of a C–C bond. That bond is kinetically disadvantaged if compared to C–H and C–O bonds; therefore, for the C_{2+} products is not only necessary to overcome the high thermodynamic barrier for the activation of the CO_2 molecule but also the unfavourable kinetics for the C–C coupling, which is the main challenging step for the formation of multi carbon products (K. Zhao & Quan, 2021).

The C–C dimerisation is still under study; however, different possibilities have been proposed for Cu-based catalysts involving the orientation of the facets, the pH, and the applied potential.

The coupling of two adsorbed *CO groups is thermodynamically more favourable at low potentials, while at more negative potentials, a different mechanism is favoured, in which the coupling occurs between a *CO and a *CHO .

Theoretical calculations also suggest that the dimer *COCO is stabilised in the presence of water and alkaline ions on Cu with lower energies for the facets (100) than on (111), which is in agreement with experimental evidence in which Cu(100) shows high activity at low overpotentials towards C–C coupling. In particular, at low local pH, the reaction pathways towards C_2 products are blocked, while at neutral pH (pH = 7), the coupling $\text{*CO} - \text{*COH}$ is unlocked, and at high local pH (about 12), the dimerisation of the *CO .

Regarding the facets, several studies have shown that for copper, the facets (100) favour ethylene C_2H_4 , the facets (111) CO and formate ($HCOO^-$), while the facets (110) favour acetate (CH_3COO^-), ethanal (CH_3CHO), and C_2H_5OH , even if the reasons for this selectivity are still unclear (Birdja et al., 2019; Y. Zheng et al., 2019; Zhong et al., 2021).

For the sake of simplicity, only the reaction pathways for ethylene and ethanol, which are the two products of great interest and therefore more studied, will be reported. Instead, for the C_3 products, the reaction mechanism is little known as these products are usually detected in traces, limiting the study (K. Zhao & Quan, 2021).

To yield ethylene and ethanol are required 12 electrons and protons. **Figure 8** shows two possible pathways for ethanol, one of these reaction pathways presents common intermediates for the production of ethylene. Still, as mentioned above, other paths that do not necessarily share the same intermediates are also possible, such as the one shown in the upper part of **Figure 8**. For both products, the reaction pathway start from the dimerisation of $*CO$ to form $*C_2O_2^-$, which will subsequently be protonated in $*COCO$ or $*COCHO$, the two forms are tautomeric. From here, there is a series of hydrogenation steps, one dehydration and the formation of a double bond between the carbon atoms passing, in the case of $*COCHO$, from $*CHOCHO \rightarrow *CHOCHOH \rightarrow *CH_2CHO$. $*CH_2CHO$ is the intermediate that determines whether ethylene or ethanol will be formed. If it is protonated further by removing the oxygen atom, C_2H_4 will be released. On the other hand, if the carbon atom not bonded to oxygen is protonated, the pathway should be $*CH_2CHO \rightarrow *CH_3CH_2O$. From here, with the addition of two electrons and two protons, first $*CH_3CH_2O$ and finally CH_3CH_2OH are formed (Fan et al., 2018; K. Zhao & Quan, 2021).

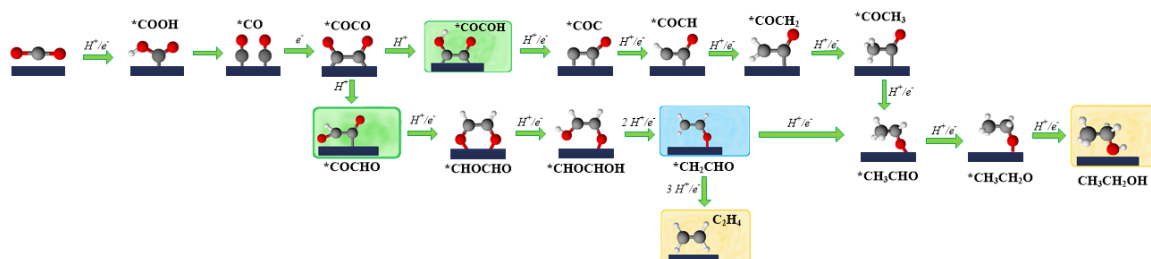


Figure 8: Ethylene and ethanol reaction pathways from K. Zhao & Quan, 2021.

3. Porous carbons for electrocatalysis

In the following section, some aspects of porous carbons useful for this work will be explored.

In addition to the advantages listed in the previous section regarding carbonaceous materials, porous carbons possess interesting and important properties which makes them promising not only for electrocatalysis but also as molecular sieves, supercapacitors, electrodes for lithium batteries, fuel cells and adsorbent materials (Liang et al., 2008).

Porous carbons have unique morphologies and a tailorable porous structure that give them a high specific surface and porous volume. The pores can be classified according to their size: micropores (< 2 nm), mesopores (2-50 nm) and macropores (> 50 nm), while based on their distribution, it is possible to have hierarchically porous carbon, but also carbon with ordered or disordered porosity (Tian et al., 2020).

The porous structure plays a crucial role in the diffusion of the electrolyte towards the surface and in the adsorption of the CO₂ molecule. Therefore, the regulation of the porous structure through the size, shape and volume of the pores is one of the factors in determining the activity and selectivity of the catalyst.

The microporosity gives the main contribution to the surface area, pore sizes close to the size of the molecule to be adsorbed increase the adsorption energy thanks to the greater number of interactions with the surface. However, their small size can lead to diffusion limits or be inaccessible due to the aggregation of molecules. Therefore, the presence of macro/mesopores is also necessary since despite having lower adsorption energy, they reduce diffusion paths, favouring mass transport and helping to increase the equilibrium coverage of micropores. A hierarchical and/or interconnected porous structure further favours these effects (Duan et al., 2017; Tian et al., 2020).

The introduction of pores, in addition to increasing the contact area between the catalytic surface and the mixture containing the reactants, can introduce important confinement effects capable of influencing chemical reactions as well as the activity and selectivity of the catalyst. The nanoconfinement originates from geometrical constraints due to the pore size and selective adsorption effects from interaction with the pore walls intensified by its greater curvature.

The neighbouring environment can favour or hinder the formation of a transition state through steric effects or fluid-wall interactions. For example, the introduction of mesopores could favour the appearance of products or intermediates that are disadvantaged in the micropores because they are spatially hindered or, on the contrary, otherwise disadvantaged products could be formed thanks to the greater number of interactions with the pore wall of micropores (Santiso et al., 2005). Furthermore, confinement in small channels or pores could increase the local concentration of reactants and their local pressure. This effect was positive in favouring C-C dimerisation and the formation of C₂₊ products (K. Zhao & Quan, 2021).

An example of the above is the nitrogen-doped ordered mesoporous carbons synthesised by Song et al. in 2017. The carbons with the same nitrogen content and pore dimension differed in porous structure: c-NC has a structure formed by mesoporous cylindrical

channels while i-NC has the inverse structure composed of interconnected cylindrical bars. The two different structures are shown in [Figure 9](#).

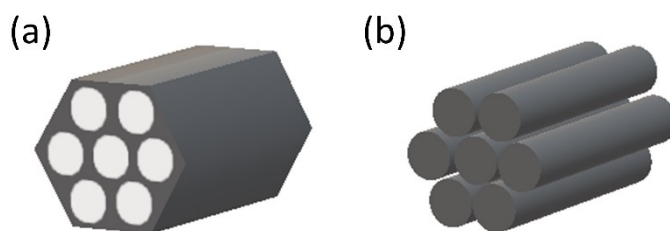


Figure 9: Schematic representation of carbon samples with (a) cylindrical channels and (b) interconnected cylindrical nanorods.

Although both structures have proved to be active for the reduction of CO₂, c-NC was superior with a faradaic efficiency towards ethanol equal to 77% at -0.56 V vs RHE, while for i-NC it was 44% at -0.50 V vs RHE. The superiority of c-NC has been attributed to the synergistic effect of the heteroatoms and the effects due to the structure of cylindrical channels, which could favour the dimerisation C-C thanks to the stronger adsorption energy of *CO due to their negative curvature.

The hybridisation of carbon atoms is another important parameter that influences their properties, and their activity can be optimised by regulating the sp²/sp³ content. Porous carbons usually exhibit a predominantly amorphous structure, containing both sp³ hybridised carbon atoms and sp² hybridised carbon atoms as in graphitic aromatic rings (K. Zhao & Quan, 2021).

In any case, as mentioned above, carbonaceous materials have negligible activity when pure, and for this reason, the introduction of different doping atoms is used to remedy that inconvenience.

3.1 Doping

In the case of the EC CO₂R, heteroatoms such as N, P, B, S were used to promote the catalytic activity of carbonaceous materials thanks to their ability to break the electrical neutrality of the carbon structure by modifying its charge distribution and spin symmetry (F. Yang et al., 2021).

The higher electronegativity of nitrogen improves the electrical conductivity and produces the formation of an active site through the polarisation of the N-C bond that leaves the carbon atom slightly positive. The NC groups can act as Lewis bases, thus favouring the CO₂ adsorption.

In the carbon lattice, nitrogen can be found in four forms, which can be seen in [Figure 10](#). These groups are identifiable by X-ray photoelectron spectroscopy (XPS) at 398. eV for pyridinic-N, 400.1 eV pyrrolic-N, 401.1 eV graphitic-N, and 403.2 eV for pyridinic-N oxide. Graphitic or quaternary nitrogen (in red) has 3 adjacent carbon atoms. It is part of a hexagonal ring and is sp² hybridised. The pyridinic nitrogen (in blue) is hybridised sp² located at the edge of a hexagonal ring with only two adjacent carbon atoms contributing to an electron to the π system. The pyrrolic nitrogen (green) is sp³ hybridised in a 5-atom

ring and contributes two electrons to the π system. Finally, pyridinic N oxide is given by nitrogen bonded to two C atoms and an oxygen (Duan et al., 2017).

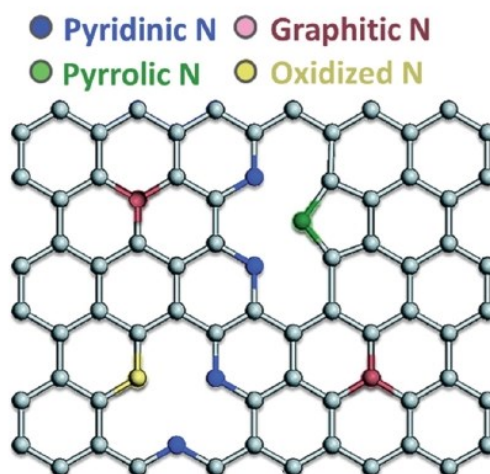


Figure 10: Nitrogen atomic configuration in the carbon framework.
Adjusted from (Singh et al., 2020).

Several studies have proven the positive effect on the activity of N species; however, the mechanisms and effects of the different groups are still being studied.

It has been suggested that pyrrolic N and pyridinic N are active for the chemical reduction of CO_2 as they can act as Lewis bases having an electronic couple available as opposed to graphitic N, which, being bonded to 3 atoms of C, does not have lone electron pair near N atoms.

In particular, the $^* \text{COOH}$ would bind to the defects N in the case of the pyridine and pyrrole N sites, while in the case of the graphitic groups, it would bind to the positive carbon atoms adjacent to the nitrogen atom. Therefore, the formation energy of $^* \text{COOH}$ would decrease following this order graphitic-N > pyrrolic-N > pyridinic-N, thus suggesting that pyridinic-N is the most favourable site (Song et al., 2017; J. Wu et al., 2016).

However, theoretical studies have indicated that the NC sites establish a relatively weak bond with key intermediate $^* \text{COOH}$ while the high spin density would seem to favour HER. As a result, many N-doped carbon catalysts suffer from low FE (<90%) and low CO current densities.

The addition of other heteroatoms, such as S, B and/or P, or metals is a possible solution to improve the performance of these catalysts (F. Yang et al., 2021). However, it will not be explored in this work.

3.2 Synthesis of ordered mesoporous carbons

As mentioned above, microporous materials can suffer from a slow mass transport of molecules due to pore size. For this reason, mesoporous materials have attracted attention especially ordered mesoporous structures, which means uniform in terms of size, shape, and volume of pores, as it can lead to better and more homogeneous properties (Davis, 2002).

3.2.1 Templating

A very effective method for synthesising ordered mesoporous materials is templating, a technique based on the reproduction of a template; it can be referred to as hard or soft templating based on the characteristics of the template.

The final morphology of the material is strongly influenced by the synthesis conditions such as the temperature, the pH, the solvent, the type and concentration of carbon precursors and the templating agent, stirring time, the type of template and his removal conditions; therefore, it is advisable to keep these parameters as constant as possible to allow the reproducibility of the synthesis (Ballem et al., 2010).

Mesoporous carbons will have a smaller area when compared to microporous carbon as they have a predominantly mesoporous uniform structure even if it still has microporosity.

The first mesoporous carbons were synthesised through hard templating, where a solid material such as anodised alumina, zeolites or silica with different nanostructures acts as a templating agent.

An example of this is the mesoporous ordered carbon CMK-1 synthesised by using MCM-48 aluminosilicate as a hard template and sugar as a carbon precursor by Ryoo et al. in 1999.

In other words, this technique involves the impregnation of a solid with a precursor of carbon so that it replicates it, after which it is the precursor so that it generally carbonises through pyrolysis and finally the removal of the template, thus obtaining an inverse replica of the template (Z. Yang et al., 2015), the process is also schematically shown in **Figure 11a**.

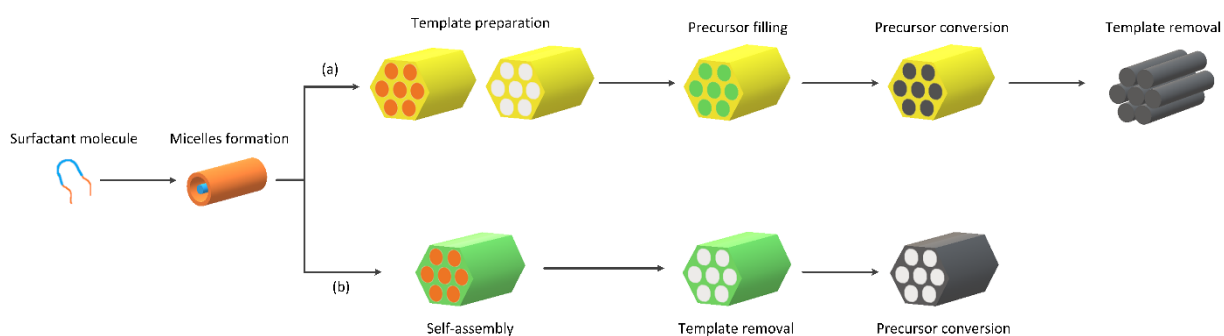


Figure 11: Schematic illustration of hard templating (a) and soft templating (b).

It is possible to resort to the soft templating method where amphiphilic organic molecules such as ionic surfactants or block copolymers can be used as templating agents, to avoid the synthesis of the solid templating.

The principle is similar to that of hard templating, but they differ in the fact that the soft method relies on the cooperative assembly of precursors and soft templates and not on the replication of a surface through its coverage (Z. Yang et al., 2015), as shown in **Figure 11b**.

An example of soft templating ordered porous materials are the mesoporous carbons synthesised by Y. Meng et al. in 2006 through the Solvent Evaporation Induced Self-assembly method (EISA) using a resol resin as carbon precursor and as a templating agent

Pluronic, a tri-block copolymer of poly(ethylene oxide)-poly(propylene)oxide-poly(ethylene oxide) (PEO-PPO-PEO).

The evaporation of the solvent during EISA causes an increase in concentrations that favour the formation of the surfactant micelles and the self-assembly.

In general, organic molecules with a high percentage of carbon, a high number of hydroxyl groups, and polymerise such as sugar, PAN, or phenolic resins are indicated as carbon precursors for templating.

To introduce nitrogen into the carbon structure during templating, starting from a nitrogen-containing precursor such as imidazoline or glucosamine or adding nitrogen-containing molecules such as urea, dicyandiamide, melamine, cyanamide together with the carbon precursor. Dicyandiamide and cyanamide have a high nitrogen content (66.7% for dicyandiamide) and a higher reactivity than melamine. Alternatively, the introduction of heteroatoms is possible through other treatments such as impregnating carbon with solutions containing precursors of the heteroatom and following calcination.

Resol as a carbon source shows very interesting properties. These resins can be obtained through catalysed condensation under basic conditions of phenol and formaldehyde with an excess of formaldehyde (phenol: formaldehyde molar ratio 1: 1.5-2). It is possible to control the polymerisation to obtain a low molecular weight (between 500 and 5000 but also $\leq 500 \text{ g mol}^{-1}$), which gives the molecules good mobility for self-assembly. The basic species act as a catalyst for polymerisation, the maximum polymerisation rate is obtained for pH around 10.

Another crucial factor is the high presence of hydroxyl groups that can interact with the hydrophilic PEO part of the block copolymer through H-bonds. The interactions between precursor and directing agent are the driving force for self-assembly that leads to mesostructure formation.

Furthermore, resol can be cured into a thermally and chemically stable thermosetting phenolic resin that allows the maintenance of the mesostructure during the template removal and carbonisation treatment (J. Wei et al., 2013).

The surfactant will also influence the final morphology it is important that the critical micellar concentration (CMC) is reached at the Krafft temperature to have the formation of micelles (Z. Yang et al., 2015).

The micelles are responsible for the shape and size of the pores, and their shape and size depends on the nature of the surfactant and its concentration.

Different mesoporous structures are possible by varying the ratio of the hydrophilic part of the PEO with respect to the hydrophobic part of the PPO of the copolymer or its concentration. For example, Pluronic F127 has higher hydrophilicity than Pluronic P123, thanks to the greater length of the PEO segments. Meng et al., in 2005, obtained structures with hexagonal 2D geometry ($P6m$) and cubic 3D ($Im\bar{3}m$) using Pluronic F127 with different concentration while using the P123 it was possible to obtain lamellar geometry structures.

After curing the resin, it is necessary to remove the templating agent through calcination and to obtain the carbon, it is necessary to convert the precursor through pyrolysis. These are very important steps that can greatly affect the final product. To remove the template,

it is sufficient to calcinate at 300-400 °C, possibly in an inert atmosphere. The removal of the template will lead to the formation of pores.

However, the final treatment temperature will decide whether an ordered mesoporous carbon or an ordered mesoporous polymer will be obtained.

If the temperature is below 600 °C you will have a mesoporous polymer; if higher, you will have carbonisation of the phenolic resin. Even if pyrolysis is a process through which there is the thermal decomposition of organic material at high temperatures in the absence of oxygen; a small amount of oxygen (approximately 2.4% v/v) in the inert gas feed can aid in the complete removal of the Pluronic and increase the pore size (Y. Meng et al., 2006).

Finally, the degree of graphitisation depends primarily on the precursor chosen. In the case of phenol-formaldehyde resins, it will not be possible to obtain a completely graphitic carbon; in fact, during the pyrolysis, the resin is transformed into carbon through polycyclic reactions. Graphite has a layered structure composed of well-stacked sheets of hexagonal rings horizontally arranged. The difficulty in graphitization originates from the strong cross-linking bonds that hinder the formation of perfectly ordered carbon sheets. The distorted carbon layers rich in defects that are created are stacked unevenly with greater distances between the planes than graphite thus leading to structures halfway between amorphous and crystalline. The two different structures are shown in **Figure 12**. Amorphous carbons generally have limited electrocatalytic activity due to the lower conductivity and the high degree of the disorder compared to graphitic carbons.

Increasing the temperature makes it possible to increase the degree of graphitisation even if the development of a graphitic structure is low even at very high temperatures (3000 °C) in the case of most thermosetting resins. However, using high temperatures is not desirable in the case of porous carbons, as any increase in graphitisation leads to a decrease in microporosity.

In the case of porous carbons, graphitisation will be further hampered by the limited volume, consisting of the pore walls, within which the transformation should take place (Duan et al., 2017; Inagaki et al., 2014).

The final temperature of the thermal treatment also affects the atomic configuration and content of nitrogen in the carbon. The nitrogen content decreases by increasing temperatures as the pyridinic-N, and pyrrolic-N groups are relatively unstable, and with the increase in temperature, they are partially eliminated and transformed into quaternary nitrogen (J. Wu et al., 2016).

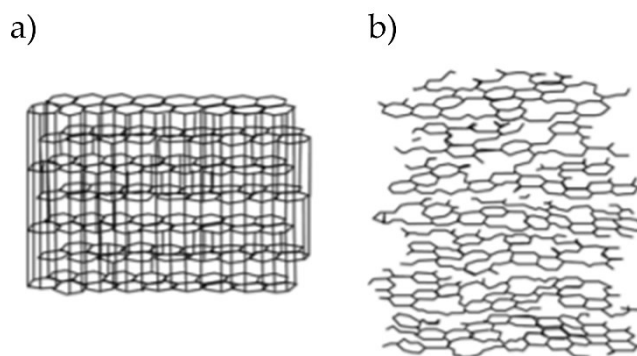


Figure 12: a) graphite and b) hard carbon structure. Adapted from (Dasgupta & Sathiyamoorthy, 2003).

4. Purpose of the work

The rapid increase in the concentration of carbon dioxide in the Earth's atmosphere has led to various environmental problems that have aroused concern and a growing interest in the chemical reduction of CO₂ into valuable chemical products. Among the possible alternatives for carbon capture and utilisation, electrocatalysis has quickly attracted attention even if it suffers from numerous limitations, including the need to develop a highly active, selective, stable electrocatalyst. Among the candidates, carbonaceous materials have stood out due to their attractive properties, low cost and great availability.

This work aimed to synthesise and investigate the catalytic properties for the CO₂ electrochemical reduction of nitrogen-doped and ordered mesoporous carbons. Porous carbons distinguished themselves among various carbonaceous materials due to their high surface area and tailorable porous structures.

In this work, the mesoporous carbon was synthesised through solvent evaporation induced self-assembly using the Pluronic F127 block copolymer as a templating agent, a low molecular weight soluble resol resin as the carbon precursor, and dicyandiamide for the introduction of nitrogen into the carbon framework. Three different heat treatments were used to investigate the role of the porous structure. In addition, ordered mesoporous CMK-3 carbon samples doped with nitrogen synthesised by a hard templating method were analysed.

Finally, a nitrogen-doped mesoporous carbon was synthesised with the addition of copper, with the aim of combining the best of the two types of catalyst and investigating the performance of the hybrid material.

5. Materials, methods and experimental procedures

In this section, the materials, the characterisation techniques, and the procedures used will be reported.

5.1 Materials

For the synthesis of the carbon were used: Phenol (99 %, *Riedel-de-Haën*), Formalin solution (37 % wt formaldehyde in water, *Sigma Aldrich*), Sodium hydroxide (97 %, NaOH, *Sigma-Aldrich*), Chlorhydric acid (37 % HCl, *Sigma-Aldrich*), Pluronic F127 (PEO₁₀₆ PPO₇₀ PEO₁₀₆) (*Sigma-Aldrich*), Ethanol (*Sigma Aldrich*), Water (purified with Milli-Q system), Dicyandiamide (99 %, *Sigma-Aldrich*), Nitrogen (99.99%) pure gas.

Copper (II) nitrate trihydrate (99 %, Cu(NO₃)₂ 3H₂O *Sigma-Aldrich*) was used as a copper precursor.

Regarding the catalytic ink, 2-propanol (99%, *Sigma-Aldrich*) and Nafion 117 solution (5% in weight in a mixture of lower aliphatic alcohols and water, *Sigma-Aldrich*) were used for the preparation.

For electrochemical tests CO₂ (99.99%) pure gas was used as a feedstock. Besides Potassium bicarbonate (99.7 % KHCO₃, *Sigma-Aldrich*) and Potassium hydroxide (99 % KOH, *Sigma-Aldrich*) were used as electrolytes.

5.2 Synthesis procedure

5.2.1 Ordered mesoporous nitrogen-doped carbon

This process can be summarised in 5 steps: 1) the synthesis of the precursor, 2) formation of a surfactant/precursor complex and assembly of mesostructures, 3) stabilisation of the structure through thermo-polymerisation, 4) removal of the template, and 5) carbonisation. In this case, steps 4 and 5 can be performed with the same treatment.

The initial step for the carbon synthesis is the pre-polymerisation of the resol resin, allowing better control of the molecular weight.

First, phenol was melted at 40-42 °C before a 20 % wt of NaOH solution in water was slowly added (one or two drops per minute) over 10 minutes while stirring. Then, formalin was added dropwise, and the mixture was stirred at 70 °C for 60 minutes to promote the condensation of phenol and formaldehyde.

These reagents should be in a molar ratio of 1:0.1: 2 (phenol: NaOH_(aq): formaldehyde); in this case were used 1.83 g (19.5 mmol) of phenol, 0.39 g (1.95 mmol) of NaOH solution, and 3.15 g of formalin (containing 39 mmol of formaldehyde).

After cooling at room temperature, the pH was adjusted to neutral (7) with a 0.6 M solution of HCl in water, avoiding further condensation. The pH was measured using litmus paper (Johnson) and a pH meter. Lastly, water was removed in the oven below 50 °C overnight. In this way, a low molecular weight resol (Mw ≤ 500 g mol⁻¹) should be obtained.

For the second phase of the synthesis, 1 g of Pluronic F127 and 1.5 g of dicyandiamide were dissolved in 20 g (25 mL) of ethanol and 10 g of water. Meanwhile, a solution of 20 % wt resol in ethanol was prepared.

Then, 5 g of 20 % wt resol solution were poured into the Pluronic and dicyandiamide solution and then stirred for 30 minutes at room temperature to form a homogeneous solution. The quantities of solvent, carbon precursor, and surfactant used were such to promote the formation of rod-like micelles and promote a hexagonal mesoscopic arrangement of the assembly (space group $p6mm$), specifically the composition range should be 1:2:0.010-0.015 (phenol: formaldehyde: Pluronic F127). The solution was transferred into a large vessel, such as a Petri dish, to maximise the surface and favour the solvent evaporation at 60 °C in the oven overnight.

Figure 13a shows the white-transparent membrane obtained. Then, it was treated at 100 °C for 24 hours to promote the curing of the resin and stabilise the mesostructure. The thermoset resin (see **Figure 13b**) was scraped from the vessel with a spatula, and the fragments were crushed and ground with mortar and pestle to obtain a powder of particle size lower than 200 μm . Lastly, 0.6 g of ground resin, with particle size between 100 and 200 μm , was put into a ceramic boat as in **Figure 13c**. The choice of particle size was made to favour heat treatment uniformity.

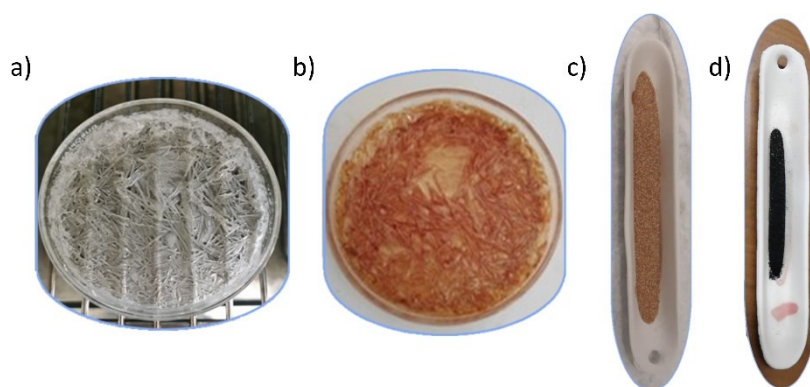


Figure 13: Resin after removal of solvent a) before and b) after thermo-polymerisation, c) resin powder, and d) carbon sample.

The powder was calcinated at 250 °C for 2 hours, then carbonised for 3 hours and left to cool to room temperature, all under nitrogen flux. Three different thermal treatments, T0, T1 and T2, summarised in **Table 4** and shown in **Figure 14**, were carried out.

Table 4: Thermal treatments parameters.

Treatment	Ramp rate (°C min ⁻¹)	Calcination		Carbonisation	
		Temperature (°C)	Held time (h)	Temperature (°C)	Held time (h)
T0	1	250	2	700	3
T1	1.5	250	2	700	3
T2	1.5	250	2	900	3

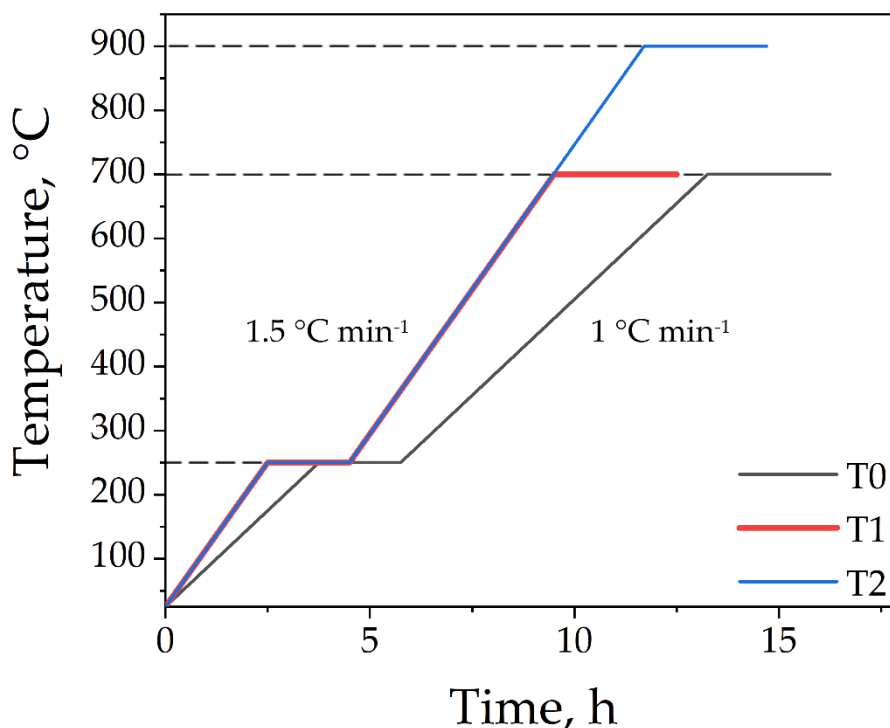


Figure 14: Representation of the different thermal treatments.

The carbon samples were named: CND_T0, CND_T1, and CND_T2 (where CND stands for Carbon Nitrogen-Doped).

Based on the measurements performed, the synthesis yield was about 25 %, for 0.6 of resin powder, about 150 mg of carbon, shown in **Figure 13d**, was obtained upon pyrolysis.

The information on the synthesis described in (Meng et al., 2005; Song et al., 2017) were used for this procedure.

Below are summed up the synthesis steps schematically, while in **Figure 15** is represented the self-assembly during EISA.

Step 1: Resol polymerisation

1. Melt phenol at 40-42 °C.
2. Add slowly 20 % wt NaOH solution over 10 minutes while stirring.
3. Add formalin dropwise.
4. Stir for 60 minutes at 70 °C.
5. Cool at room temperature and adjust to neutral pH using a 0.6 M HCl solution.
6. Remove water below 50 °C overnight.

Step 2: Meso-structuring, formation of the surfactant/resol complex

7. Dissolve Pluronic F127, Dicyandiamide in a mixture of 10 g of water and 20 g of ethanol.
8. Prepare 5 g of 20 % wt resol solution in ethanol.

9. Pour the resol solution into the Pluronic F127 solution.
10. Stir for 30 minutes at room temperature and pour the mixture into a wide vessel.
11. Remove the solvent in the oven at 60 °C overnight.

Step 3: Thermosetting and powders

12. Cure the resin at 100 °C for 24 hours.
13. Scrape off the resin with a spatula.
14. Grind the fragments with mortar and pestle.

Step 4-5: Template removal and carbonisation

15. Put 0.6 g of resin powder in a ceramic boat and position the boat in the middle of the tubular furnace tube.
16. Calcinate and carbonise in an inert atmosphere.

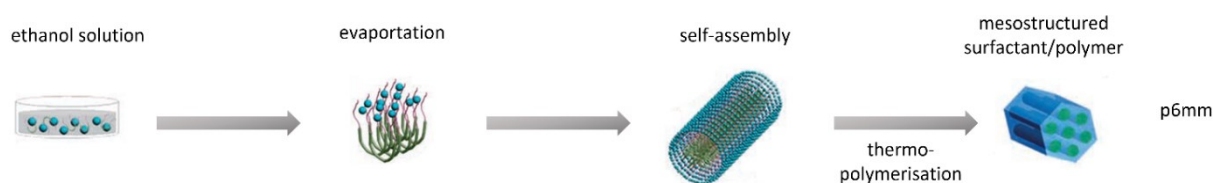


Figure 15: Formation of the pluronic/resol complex during EISA promoted by solvent evaporation. Adjusted from (Meng et al., 2005).

To further study the influence of the structure, two other samples were electrochemically analysed: CMK-3-600 and CMK-3-750. These samples were synthesised by Elisa Maruccia of the Istituto Italiano di Tecnologia (IIT) through hard templating using a mesoporous silica SBA-15 (space group p6mm) as a solid template and an aminosaccharide, glucosamine, as a precursor of carbon and nitrogen. The CMK-3-600 sample was obtained following pyrolysis at 600 °C, while for the CMK-3-750 sample, the pyrolysis took place at 750 °C. The SBA-15 synthesis procedure can be found in (Nicolas et al., 2008) with a hydrothermal treatment temperature of 100°C, while more details about the CMK-3 synthesis are reported in (Maruccia et al., 2022), with the only difference being the solid template used.

5.2.2 Ordered mesoporous nitrogen-doped carbon with copper

Copper was introduced in the carbon structure. Copper(II) nitrate trihydrate was chosen as a precursor since it is easy to handle and decomposes into copper oxide (CuO) after calcination.

Copper nitrate was reduced to a fine powder with a pestle before being added and mixed to the resin, obtained in the mortar as described in the previous section (step 1-14). To better disperse the nitrate and attain a powder as homogeneous as possible, the mixture was transferred into an agate vessel with 4-5 agate balls and mixed for 1 hour and 20 minutes at 300 rpm using a grinding mill IGWE2E/S (Giuliani, Torino, Italy). Then, 0.6 g of the resultant mixture, homogeneous at the eye as shown in **Figure 16a**, was placed in a ceramic boat and thermally treated according to T0.

The quantities of nitrate and resin powder were decided to achieve the 30 % in weight copper concentration in the final carbon sample considering 10 % of losses during grinding and blending, assuming the complete decomposition of copper and a yield of 25 % for the resin pyrolysis. The sample was named Cu_CND_T0, shown in **Figure 16b**.

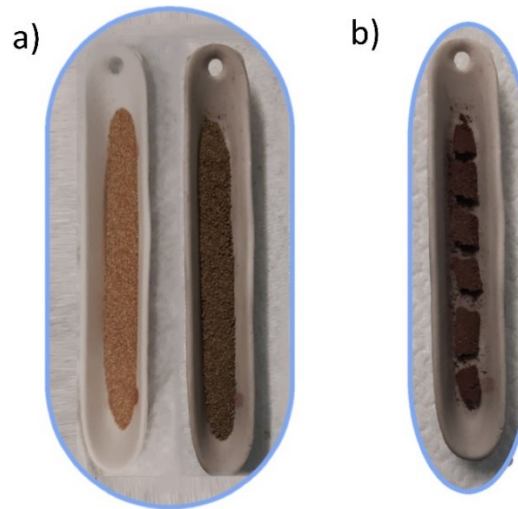


Figure 16: a) colour change after adding copper nitrate to the resin mixing and b) sample Cu_CND_T0.

Additionally, 0.6 g of copper nitrate was treated following the same calcination ramp of the thermal treatment T0 to verify his complete decomposition and investigate the difference in performance compared to carbon with copper. This sample was named CuO. The carbon samples were rapidly ground using a mortar and pestle to obtain a homogeneous and fine powder by breaking aggregates formed during the heat treatment. **Table 5** summarises the samples and the corresponding heat treatments analysed in this thesis.

Table 5: Sample list with the corresponding heat treatments.

Sample	Thermal treatment
CND_T0	Ramp rate 1 °C/min carbonisation
Cu_CND_T0	temperature 700 °C (T0)
CND_T1	Ramp rate 1.5 °C/min carbonisation
	temperature 700 °C (T1)
CND_T2	Ramp rate 1.5 °C/min carbonisation
	temperature 900 °C (T2)
CMK-3-650	Pyrolysis at 600 °C
CMK-3-750	Pyrolysis at 750 °C
CuO	Calcination 250 °C, Ramp rate 1°C/min

5.3 Characterisation techniques

The following techniques characterised the samples.

Nitrogen adsorption was used to investigate the surface area and the pore distribution collecting the nitrogen isotherms at 77 K using a Micrometrics Tristar II 3020, shown in [Figure 17a](#).

The adsorption method is an effective method that involves the use of molecules as a probe to detect information regarding pores. In the case of nitrogen, the pore size range detectable is 2-50 nm and therefore, it is not fit for microporosity investigation.

The specific surface area was calculated with the Brunauer- Emmett-Teller (BET) model using the nitrogen adsorption branch in the range of relative pressures (P/P^0 , where P^0 is the saturation pressure of the adsorption gas) between 0.1 and 0.3, while the pore size distribution and volume were derived from the adsorption branch using the Barrett-Joyner-Halenda (BJH) model.

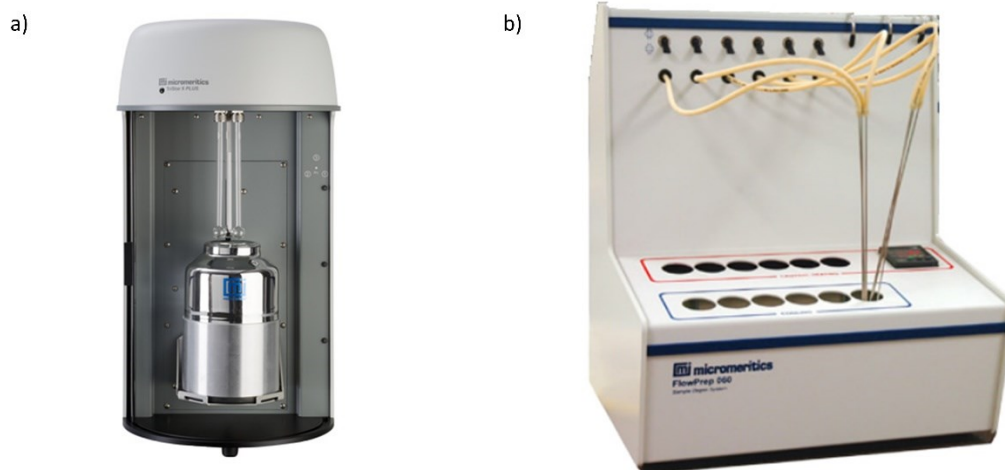


Figure 17: a) Micrometrics Tristar II 3020 and b) degassing station FlowPrep060.

Typically for the analysis, 100 mg of carbon were placed in a burette which, before being inserted into the instrument, was heated to 200 ° C for 2 hours under nitrogen flux, using the degassing station shown in [Figure 17b](#), to favour the desorption of any adsorbed substances.

X-ray diffraction (XRD) is a common non-destructive technique based on the study of elastic X-ray scattering after hitting a sample, a phenomenon that requires the presence of reticular planes and, therefore, crystallinity. This technique was used to investigate the degree of graphitisation and the nature of the copper species. The analyses were performed with a Malvern Panalytical X'Pert PRO X-ray diffractometer with a Cu $K\alpha$ monochromatic radiation wavelength $\lambda = 1.54 \text{ \AA}$, shown in [Figure 18a](#). The XRD patterns were collected in a range of 2θ angles of 10°- 80 °; unfortunately, it was impossible to perform analyses at smaller angles to study the mesoporous structure due to issues with the instrument at our disposal. The average crystallite sizes (D) of copper phases were calculated through the Debye-Scherrer equation (see [Equation 3](#)); where K is a shape factor typically equal to 0.9, λ is the X-ray wavelength, β is the line broadening at half the maximum intensity (FWHM) and θ is the Bragg angle.

$$D = \frac{K\lambda}{\beta \cos\theta}$$

Equation 3

A ZEISS Merlin Field Emission Scanning Electron Microscope (FESEM) was used to collect images about the samples and investigate their morphology. This equipment, shown in **Figure 18b**, also allows investigating the composition through Energy Dispersive X-ray Spectroscopy (EDS).

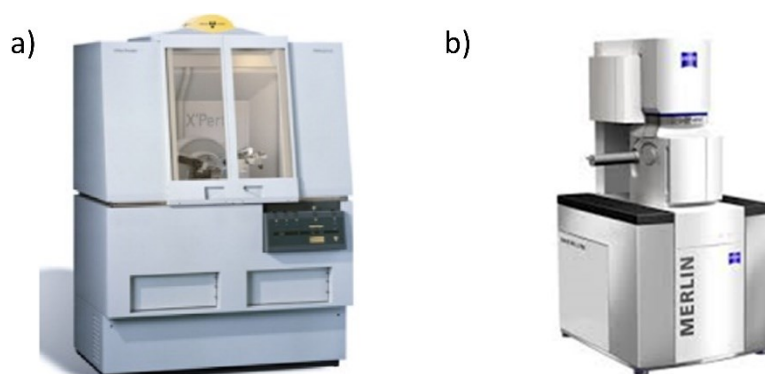


Figure 18: a) Malvern Panalytical X'Pert PRO X-ray diffractometer and b) ZEISS Merlin FESEM.

Samples for FESEM were prepared by dispersing a small amount of catalyst in ethanol through sonication for 5 minutes. A droplet of 5 μL was deposited on a Lacey Carbon only 200 mesh copper (Ted Pella Inc.) in the case of samples CND_T0, CND_T1, CND_T2. While for the copper-based samples, the deposition took place on Lacey Carbon 200 mesh Ni (EMResolution) to facilitate its detection. After solvent evaporation, the mesh was attached on a stab through adhesive tape.

Raman spectroscopy analyses were performed using a Jobin Yvon HR800 LabRam μ -spectrometer (HORIBA Jobin Yvon, Paris, France), shown in **Figure 19**, to further investigate the mesoporous carbon structure and nitrogen content. The spectra were obtained under conditions to preserve the sample without modification caused by laser energy. Specifically, the operating conditions adopted were a spectral range between 4000-100 cm^{-1} , a green laser ($\lambda = 532 \text{ nm}$) with a 3.2% filter and two exposures of 30 seconds (total time accumulation). The spectra were then subjected to deconvolution through a seven-way fitting process, explained in Croce et al., 2021. The analyses were performed by A. Croce, G. Gatti, L. Cagna of the Università del Piemonte Orientale (UPO).



Figure 19: Equipment for Raman spectroscopy.

X-ray photoelectron spectroscopy (XPS) analyses were performed to study the surface composition, the nitrogen and copper content, and their atomic configuration using a PHI 5000 Versa Probe system (Physical Electronics, Chanhassen, MI, USA) equipped with a source of monochromatic X-rays Al K α (1486.6 eV).

The deconvolution procedures were performed through a dedicated Multipak 9.7 software.

5.4 *Electrochemical activity testing*

The electrocatalytic activity of the different studied samples was examined through different electrochemical techniques. The electrical supply to the electrochemical cell was ensured by a Biologic VSP-300 multichannel potentiostat (Bio-Logic SAS, Seyssinet-Pariset, France), which was operated in potentiostatic and galvanostatic mode.

Cyclic voltammetry (CV) was performed with N₂ and CO₂ to get a first idea of the catalyst activity, to ensure its stability for subsequent analyses and to test the behaviour in the reaction medium. In addition to this, through cyclic voltammetry, it is possible to obtain information about the redox peaks (anodic-cathodic branches), which can be associated with oxidation (positive currents) or reduction process (negative current) reaction. The onset is the potential value at which a reaction product is produced at a given electrode and defined conditions CV is a potentiodynamic method involving the linear variation of the working electrode potential with a constant scan rate (V s⁻¹) from a preset maximum to a minimum. After reaching the lower limit, the potential returns to the maximum value. This inversion can occur numerous times to obtain the desired number of cycles. During the test, the current intensity is recorded and plotted as a function of the applied potential.

Linear scanning voltammetry (LSV) was performed for screening potentials and determining an onset potential for the reduction reaction. The onset is the potential value at which a reaction product is produced at a given electrode and defined conditions. In general, LSV follows the same principle as CV. The current is measured as a potential function that varies linearly from a maximum to a minimum. It is a non-cyclical measurement as once the lower limit is reached, there will be no inversion. Moreover, it was performed at lower scan rates than the CV for greater accuracy.

Chronopotentiometry (CP) or Chronoamperometry (CA) were performed to evaluate the electrocatalytic activity of the different materials studied, obtaining the productivity and the Faradaic efficiency towards the different CO₂ reduction products. Unlike the abovementioned techniques, a constant magnitude is applied to the electrode. In chronopotentiometry, a constant current density is applied to the electrode for a certain period of time, and the required potential to maintain that current density is. The potential assumes a value at which the flow of the electro-active species towards the electrode is sufficient to balance the applied current. (Baur, 2007).

On the other hand, in chronoamperometry, a constant potential is applied to the working electrode, and the required current density is registered. The CA is useful for monitoring processes governed by diffusion, as in the case of CO₂ reduction; in fact, the current varies over time based on the diffusion of the analyte from a certain distance in bulk to the electrode surface. From the CA, it is possible to obtain information on the kinetics of the reactions, the diffusion of the species, and their adsorption.

5.4.1 Electrochemical cell configuration and setup

The electrochemical tests were performed at ambient temperature and pressure, adopting a 3-electrode gas-tight system (see **Figure 20**) consisting of an H-cell with compartments separated by a Nafion 117 membrane. The counter-electrode was a Pt coil, while a silver/silver chloride electrode (Ag/AgCl, 3 M NaCl) was used as reference. The catalysts were deposited on a glassy carbon rotating disk electrode (RDE) or on a porous Toray carbon paper (TP-060T Quintech, Göppingen, Germany), which were used as a working electrode.

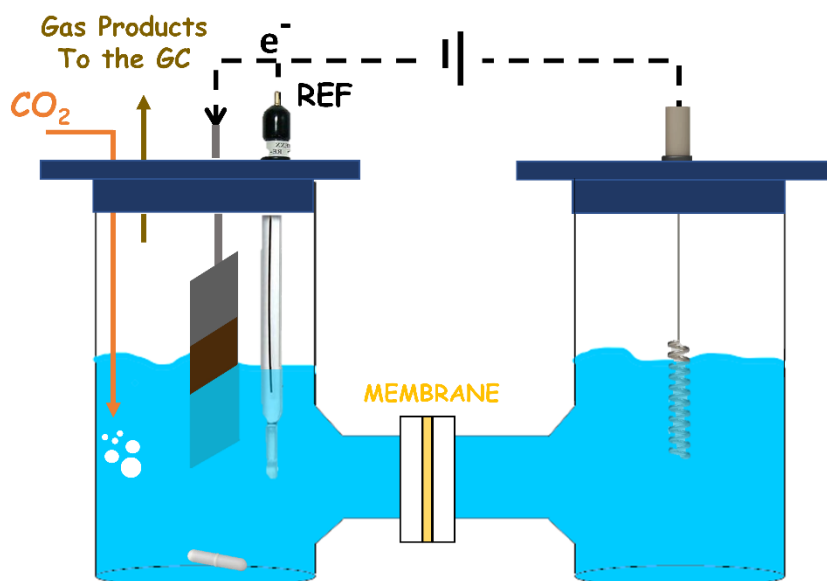


Figure 20: Schematic representation of the electrochemical cell used for testing the electrochemical activity.

Preliminary tests were performed using a RDE system (RRDE-3A), shown in **Figure 21a** since it is simpler and avoids mass transfer limitations. It consists of a rotating unit to which RDE is connected. The electrode was immersed in the electrolyte during the test and set into rotation thanks to a motor. The system is equipped with an RDE with a 5 mm diameter glassy carbon (GC) disc, on which the catalyst can be deposited, surrounded by a Teflon ring that facilitates the deposition, as shown in **Figure 21b**. A 0.1 M KHCO₃ solution was used as the electrolyte, 45 mL in the cathodic compartment and 34 mL in the anodic compartment.

CV was performed under both N₂ and CO₂ flow by scanning the potential from 0 to -3 V vs Ag/AgCl at a scan rate of 30 mV s⁻¹. LSVs were performed in the same potential range but with a scan rate of 5 mV s⁻¹. Chronopotentiometry was performed in a CO₂ saturated electrolyte applying a current intensity I of -3.9 mA, equal to a current density $J = -20$ mA cm⁻², for 2 hours.

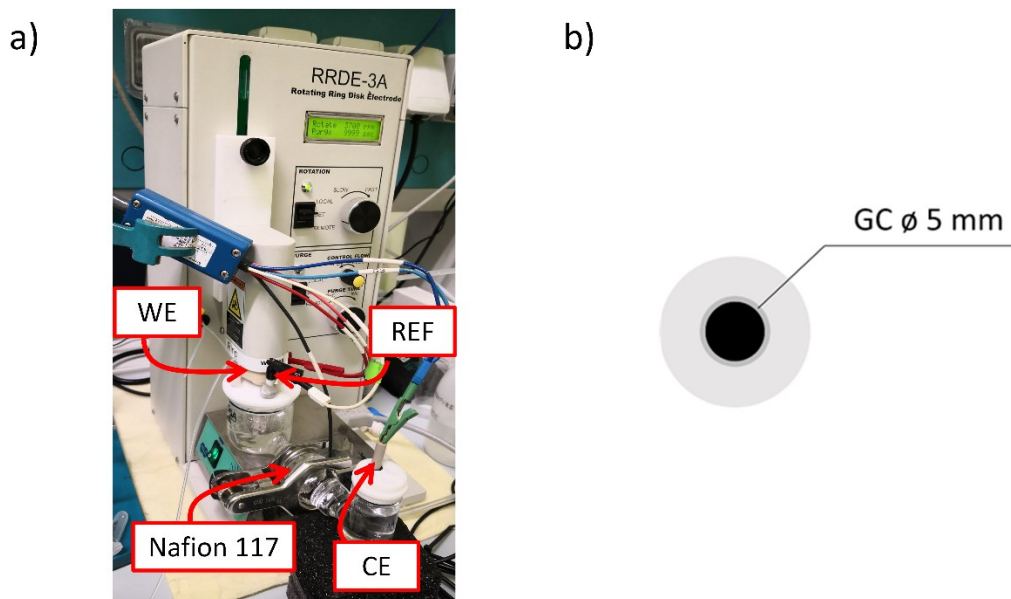


Figure 21: a) setup used for RDE testing and b) top view of the RDE.

The gases were bubbled with 8.86 NmL/min flow controlled through a mass flow controller (EL-Flow Select, PN64). All the tests were performed after gas saturation of the electrolyte with the RDE rotating at 3000 rpm. Samples CND_T1 and CND_T2 were analysed with a catalyst loading equal to 0.6 mg cm⁻².

Subsequent analyses employed working electrodes with a larger area and higher catalyst loading, 1 cm² and 1 mg cm⁻², respectively. As mentioned before, the electrodes were made depositing the catalyst material onto a carbon paper substrate; with the aim of increasing the productivity of the reaction.

As in the previous case, a 0.1 M KHCO₃ solution was used as the catholyte, while a 0.1 M KOH solution was used as the anolyte to reduce the electrolyte resistance since it presents a higher conductivity. The CVs were performed first by bubbling N₂, then CO₂, again after the electrolyte saturation; furthermore, the catholyte was stirred to mimic the conditions of the RDE, to try to avoid mass transfer limitations. Flows of 10 NmL min⁻¹ were used for both N₂ and CO₂. CVs were performed between 0 and -2.5 V vs Ag/AgCl at 10 mV s⁻¹.

A continuous CO₂ electrolysis tests under constant potential mode (CA) were performed for 20 min at different potentials: -1, -1.2, -1.6 V vs Ag/AgCl (corresponding to -0.4, -0.6, -1 V vs RHE) in CO₂ saturated electrolyte. Since more positive potentials would favour the production of more reduced products, such as C₂₊ products, it was decided to apply lower potentials. It is in agreement with what has been reported in the literature (Birdja et al., 2019; Song et al., 2017; K. Zhao & Quan, 2021).

The change in the pH of the electrolyte resulting from its saturation has been considered; hence the potentials will be converted using [Equation 4](#) and referred to RHE in the next chapters.

$$E_{RHE} = E_{Ag/AgCl} + 0.21 + 0.059 \cdot pH \quad \text{Equation 4}$$

The pH values were 8.32 for N₂ and 6.8 for CO₂ in the case of a saturated 0.1 M KHCO₃ solution.

During the CO₂ electroreduction tests for both CPs and CAs, the gaseous products were analysed online using an Inficon Micro GC fusion gas chromatograph. The liquid samples taken at the beginning and end of the test were analysed to detect formate with a High-Performance Liquid Chromatography (HPLC) Prominence by Shimadzu, equipped with two detectors RID-10A and PDA 212 nm, a Rezex ROA Organic acid column (D: 7.8 mm; L: 300 mm) and using 5 mM H₂SO₄ as the mobile phase. A gas chromatograph with a mass spectrometer detector Perkin Elmer GC Clarus 580, equipped with a Head Space and a Stabilwax-DA column, was employed to detect the other liquid products.

The Faradaic efficiencies were calculated following [Equation 2](#). In the case of the carbon paper electrodes, since the samples for the liquid products were taken, for simplicity, only at the end of the 3 CA the efficiencies were calculated considering the total charge spent in the 3 tests and therefore not referable to a single potential.

5.4.2 ECSA measurements

The electrochemical active surface area was determined through the double-layer capacitance method using the RDE system abovementioned. All the samples were analysed at 1500 rpm adopting a catalyst loading of 0.6 mg cm⁻² with 45 mL of 0.1 M KHCO₃ solution as catholyte and 30 mL of 0.1 M of KOH solution as anolyte.

The measurements were conducted in a 500 mV potential window centred at the open circuit potential (OCP) of the system and on the assumption that all the measured current was spent in the double-layer charging. In this potential window, no faradaic processes occur. The capacitive current (*i_c*) was measured by performing CVs at different scan rates (5, 10, 25, 50, 75, 100 mV s⁻¹). Through the capacitive current, electrochemical double-layer capacitance (*C_{dl}*) was obtained using [Equation 5](#), which is based on the hypothesis that the current is given by the product of the electrochemical double-layer capacitance (*C_{dl}*) and the scan rate (*v*) (Clark et al., 2018; Morales & Risch, 2021).

$$i_c = C_{dl} \cdot v \quad \text{Equation 5}$$

Therefore, the *C_{dl}* is the slope of the linear fitting of the *i_c* plotted versus the multiple scan rates. The ECSA can be calculated through [Equation 6](#), which is the ratio between *C_{dl}* and *C_s*. The *C_s* is the reference capacity for a flat surface of the same material. A *C_s* value equal to 27 μF cm⁻² was used for the carbon-based electrodes (Schild et al., 2021), while for the copper-based electrodes, a *C_s* of 28 μF cm⁻² was used (Zeng et al., 2018).

$$ECSA = \frac{C_{dl}}{C_s} \quad \text{Equation 6}$$

5.4.3 Working electrodes preparation

The working electrodes, shown in [Figure 22](#) were made by depositing the catalyst on a substrate through ink with two different compositions depending on the substrate.

The ink for RDE deposition was composed of 5 mg of catalyst, 20 μL of Nafion 117 solution as a binder to facilitate adhesion to the substrate, and as a solvent 100 μL of water and 900 μL of 2-propanol.

The mixture was homogenised for 20 minutes using an ultrasonic tip at 30 kHz. During sonication, the vial was immersed in cold water (about 4 °C), which was changed after 10 minutes to counteract particle aggregation. For the deposition, the ink density was obtained by averaging several measurements using a known volume and a laboratory scale; then, knowing the area of the electrode, the percentage of catalyst in the ink and its density, it was possible to deduce the catalyst loading. The calculations used are shown below in more detail.

$$(\%wt)Catalyst = \frac{Carbon\ mass}{Carbon\ mass + Nafion\ sol.mass + isopropanol\ mass + H_2O\ mass} \cdot 100$$

For this ink composition the $(\%wt)Catalyst\ in\ the\ ink \cong 0.6\ \%$. For the ink mass, an arbitrary value of the volume V was taken to deposit.

$$Ink\ mass = Ink\ density \cdot V$$

$$Catalyst\ mass = Ink\ mass \cdot (\%wt)Catalyst$$

Assuming 5% of ink losses during deposition and knowing the RDE area equal to 0.1962 cm^2 , it is possible to obtain the catalyst loading.

$$Catalyst\ mass\ with\ loss = Catalyst\ mass \cdot (0.95)$$

$$Catalyst\ loading = \frac{Catalyst\ mass\ with\ loss}{Electrode\ Area}$$

At this point, V can be written as a function of catalyst loading:

$$V = \frac{Catalyst\ loading \cdot Electrode\ Area}{Ink\ density \cdot 0.95 \cdot (\%wt)\ catalyst}$$

In this way, it is possible to know the ink volume necessary to obtain the desired quantity of catalyst on the electrode. It was deposited drop by drop using a micropipette and removing the solvent through evaporation at 400 rpm for a couple of minutes between one drop and the next.

At the end of its use, the RDE was cleaned using an alumina suspension and a diamond suspension on polishing cloths. Then, it was rinsed using pure water and dried.

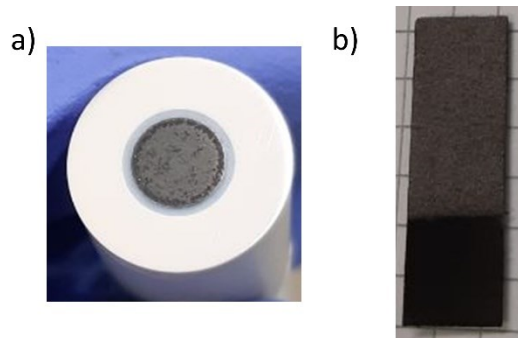


Figure 22: Images of the working electrodes used a) RDE and b) carbon paper.

For carbon paper substrates, the first step was cutting portions of carbon paper 1 cm wide and 3 cm long, which were covered with a Teflon mask leaving exposed an area of 1 cm² and fixed on a heating plate.

The ink was prepared using 10 mg of carbon powder and 1 ml of diluted Nafion 117 solution 0.25% wt in ethanol. It was homogenised using an ultrasonic tip for ten minutes while the vial was immersed in cold water.

The resultant mixture was air-brushed on the carbon paper favouring solvent evaporation at 70 °C and left drying for 15 minutes. This temperature was chosen for rapid solvent removal but avoiding modification of the catalyst.

The quantity of the solid deposited corresponding to the increase in mass (Δm) of the carbon paper after deposition was obtained according to the calculation below, after measuring the mass of the piece of carbon paper before (m_i) and the final mass (m_f) with a scale.

$$\Delta m = m_f - m_i$$

Knowing that the increase in mass is due to the solid deposited, 85% of it is the catalyst and that the area of the substrate is 1 cm², it is possible to obtain the catalyst loading as:

$$\text{Catalyst loading} = \Delta m \cdot 0.85 \cdot 1 \text{ cm}^{-2}$$

6. Results and Discussion

The results of the characterisations performed and the electrochemical activity investigation will be reported and discussed in the following section.

6.1 Physical characterisation results

For CMK-3 samples, the results will be briefly reported since they were not characterised in this work.

6.1.1 Nitrogen adsorption

The specific surface area is a crucial aspect for a catalyst, **Table 6** shows the results obtained through nitrogen adsorption. Unfortunately, it was impossible to analyse CuO and Cu_CND_T0 samples due to an instrument failure.

Analyses of the carbon precursor before thermal treatment confirmed the absence of porosity and the positive role of the carbonisation treatment in its formation.

CND_T0, CND_T1, CND_T2 samples showed type IV nitrogen adsorption isotherms, in **Figure 23a**, typical of materials with mesoporous structures. The rapid increase in adsorption in low-pressure regions suggest the presence of micropores originating from the dehydrogenation and dehydration of the thermoset resin during the pyrolysis process (Z. Meng et al., 2021). Capillary condensation in the low relative pressures region (0.4-0.6) indicates a narrow pore size distribution (Uddin Ahmad et al., 2019), further confirmed by the pore size distribution obtained in **Figure 23b**. The largest surface area is $460 \text{ m}^2 \text{ g}^{-1}$ belonging to CND_T0, while CND_T2 shows the minor one equal to $328 \text{ m}^2 \text{ g}^{-1}$, as visible in **Table 6**. Both samples show similar curves with a steep H1 hysteresis loop indicating the presence of an ordered mesoporous structure with cylindrical channels, again supported by the pore size distribution, which suggests the same for CND_T1 as well. However, this sample shows an H3 hysteresis loop with further adsorption in high relative pressure range ($P/P^0 \geq 0.8$) attributable to the existence of non-framework mesoporosity (interparticle voids) as also visible from the cumulative pore volume in **Figure 23c** (Ayinla et al., 2019; Z. Yang & Mokaya, 2008).

The CND_T0 nitrogen isotherm lacks adsorption in the abovementioned pressure range meaning a virtual micropore free structure, purely mesoporous, imputable to the lower ramp rate used in treatment T0 (Z. Yang & Mokaya, 2008).

In the case of CND_T2, it should be noted that the hysteresis loop does not close even at low pressures. The slowness of the system could also be caused, in this case, by the presence of interparticle porosity or a greater microporosity. In fact, the increase in the carbonisation temperature promotes the decomposition of the precursor by favouring the increase of microporosity and leads to the sintering of part of the porosity, causing the opposite effect. The sharp increase at relative pressures close to 1 could mean the presence of micropores. Considering the significant decrease in the surface area, it can be assumed that the high carbonisation temperature of treatment T2 ($900 \text{ }^\circ \text{C}$) possibly induced the formation of micropores but also has led to a partial collapse of the carbon framework and loss of porosity (Long et al., 2015).

The analyses confirmed a narrow pore size distribution centred at 3.7 nm, thus confirming the ordered porous structure. The larger pore size of CND_T1 may be due to the faster heating ramp rate, which causes non-homogeneous carbonisation of the precursor. It is not true for sample CND_T2, possibly because the higher final temperature prevented this effect. The variation in pore size is therefore attributable to how much the carbon framework shrinks during carbonisation. Low heating rates or higher temperatures result in lower shrinkage and smaller pores (Z. Yang & Mokaya, 2008). In any case, the ramp rates used in this work were low enough to obtain mesoporous ordered carbons.

Thermal treatment T0 produced mesoporous carbon with the best order, higher surface area, and possibly micropore-free as it offers a more homogeneous carbonisation process. It is also plausible that the evolution of gases resulting from the precursor organic species decomposition is slower, minimising the disturbance to the carbon framework formation (Z. Yang & Mokaya, 2008).

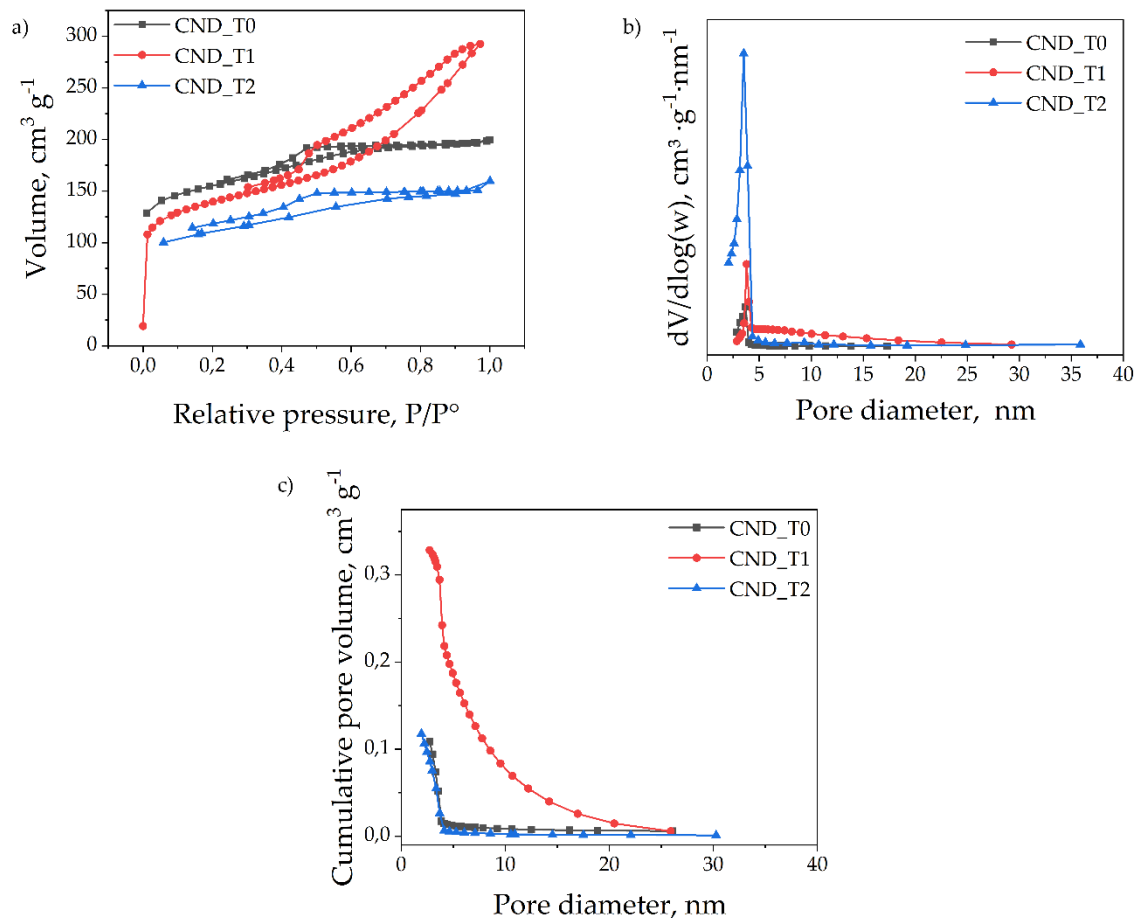


Figure 23: a) nitrogen adsorption isotherms, b) pore size distribution, c) cumulative pore volume of CND nitrogen-doped carbon samples.

Table 6: Specific surface area (SSA) and average pore size.

Sample	SSA _{BET} (m ² g ⁻¹)	Pore size (nm)
CND_T0	460	3.7
CND_T1	446	3.9
CND_T2	328	3.5
CMK-3-600	605	4
CMK-3-750	656	4

6.1.2 X-ray diffraction

High angle XRD spectra show the presence of graphite-like carbon in almost all samples. Instead, as already anticipated, it was impossible to perform small-angles XRD ($2\theta < 10^\circ$) and, therefore, obtain information on the order and symmetry of the mesoporous structure with this analysis. However, considering the procedure used to synthesise the samples is plausible to hypothesize an ordered mesostructure with hexagonal symmetry (p6mm).

XRD profiles of the nitrogen-doped carbon samples are shown in [Figure 24](#). CND_T0 and CND_T2 exhibit diffraction shoulders for angles 2θ of 24° and 43° , identifiable to the graphitic reflections (002) and (101) respectively (J. Ni et al., 2013). Graphite (002) shows peaks at 26° . The shift towards lower angles means that the microcrystallites of these samples differ from those of graphite (Lee et al., 2021). The presence of broad peaks at lower angles can be ascribed to the lower number of uniformly stacked graphitic layers with greater interplanar distances than in graphite due to weaker Van der Waals interaction between distorted carbon layers (Q.-S. Du et al., 2017). The synthesised carbons show a low degree of graphitisation despite the crystallinity and a high degree of disorder.

Samples CND_T0 and CND_T2 possess higher crystallinity, coherent to the longer treatment time set in the T0 and the higher temperatures of T2. The higher intensity of the CND_T2 (002) shoulder could be ascribed to larger crystallites. Although CND_T1 and CND_T0 were treated with the same carbonisation temperature, CND_T1 presents a structure completely amorphous as visible from the absence of peaks in the spectra. It can be explained by the faster heating rate, which results in a shorter residence time at temperatures higher than 600°C and more disturbed carbonisation. Furthermore, as mentioned in paragraph 3.2.1, graphitisation depends on the carbon precursor. In the case of phenolic resins, which are hard carbon precursors, it is hard to obtain carbons with high graphitisation due to the difficulty of the uniform stacking of graphitic planes. The introduction of nitrogen in the structure further promotes lower graphitisation distorting the bonds because of the higher electronegativity and difference in atomic mass.

Higher temperatures and/or lower ramp rates promote higher crystallinity and also higher graphitisation. Samples CMK-3 also show a low degree of graphitisation with only a broad peak, broader than CND samples, corresponding to (002) planes.

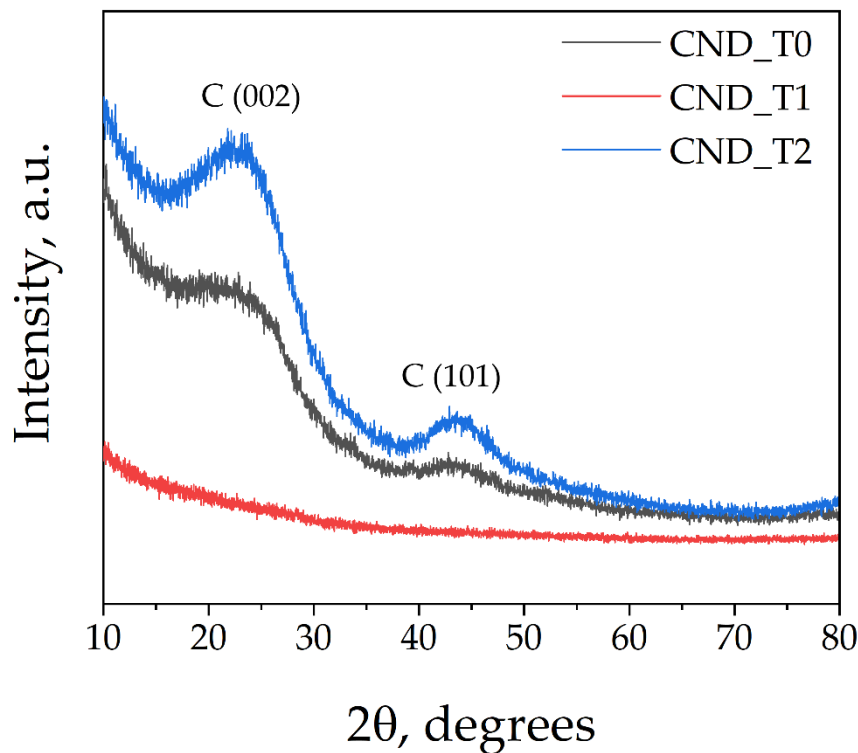


Figure 24: XRD spectra of nitrogen-doped carbon samples.

The XRD analyses at angles 2θ between 10° and 80° on the samples with copper CuO and Cu_CND_T0 are in [Figure 25](#). Cu_CND_T0 has a broad peak around 24° , similar to his copper-free counterpart CND_T0 and other additional three peaks. The diffraction peaks located at 43° , 50° , and 74° are assigned to the reflections (111), (200), and (220), respectively, corresponding to metallic copper. Therefore, it can be stated that the metal is crystalline, with crystallites having an average size of 28 nm, probably present in the form of nanoparticles resulting from the aggregation of atoms due to the considerable amount of copper introduced in the carbon. However, it could be possible that the copper is present also in the form of Cu-N_x moieties.

The copper nitrate trihydrate was completely decomposed in copper oxide and then reduced by the reducing species (such as carbon monoxide) evolved from the resin pyrolysis. The complete decomposition of the nitrate after calcination was also proved through the analyses of the CuO sample in [Figure 25b](#). The profile shows different peaks, all attributable to different diffraction reflections of copper (II) oxide with higher intensity for the (111) and ($\bar{1}\bar{1}\bar{1}$) planes, and the average crystallite size is 17 nm. All peaks belong to a single phase of the monoclinic crystal system structure with space group Cc. It is worth remembering that the CuO sample is a reference to Cu_CND_T0. Therefore, it was not synthesised with a process that would allow the selection of specific features, such as facets, for EC CO₂R. The absence of nitride peaks confirms the dispersion of nitrogen in the carbon.

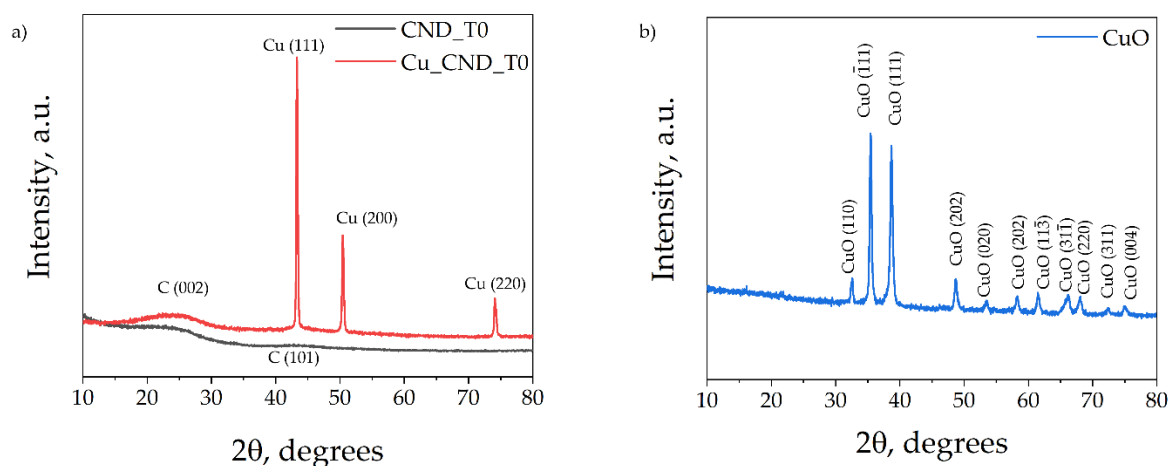


Figure 25: XRD profile of a) *Cu_CND_T0*, b) *CuO*.

6.1.3 FESEM and EDS

Different features of the ordered mesoporous metal-free CND carbons are shown in **Figure 26**. The CND samples exhibit particles of irregular shape (see **Figure 26a**) with heterogeneous sizes from a few hundreds of nanometers to a few micrometres. In general, the particles show uneven rough surfaces with excoriated sections (see **Figure 26b** and **d**), possibly due to the grinding (Mangi et al., 2022). Some of them possess sponge-like morphology, as visible in **Figure 26c**. The magnification and resolution were insufficient to investigate the porous structure.

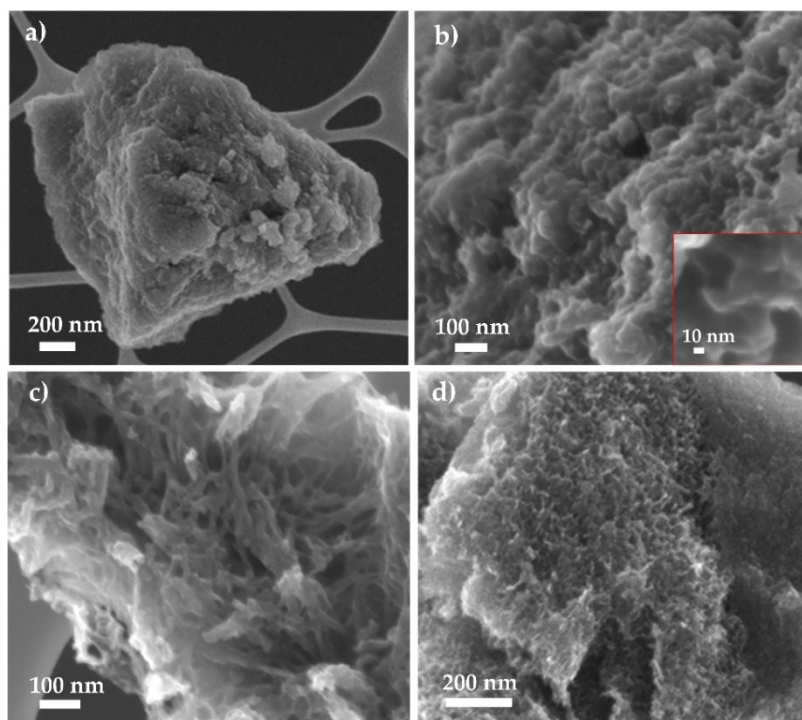


Figure 26: Different details for CND carbon samples: a) *CND_T1* particle (50 kX), b) particle surface from *CND_T1* (100kX) with detail at 500kX, c) *CND_T0* sponge-like morphology (250 kX), d) *CND_T2* (100kX).

Cu_CND_T0 particles have a similar shape and size to the metal-free counterpart but, unlike the latter, show numerous nanostructures on the surface (see [Figure 27b](#)). It is assumed that they result from the aggregation of copper atoms during the heat treatment to form crystalline clusters of irregular shapes densely packed due to a large amount of copper introduced.

CuO also presents particles of different sizes and wide distribution ranging from hundreds of nanometers to micrometres. It shows both irregular particles (see [Figure 27d](#)), formed by disordered aggregations of prismatic crystals and nanosheets, and ordered structure. [Figure 27c](#) is shown a flower-shaped spherical particle whose external surface is made of CuO nanosheets, with a thickness of a few tens of nanometers, densely packed grown in a self-organized way proper to give micro-flowers with radii of few micrometres (Khan et al., 2013).

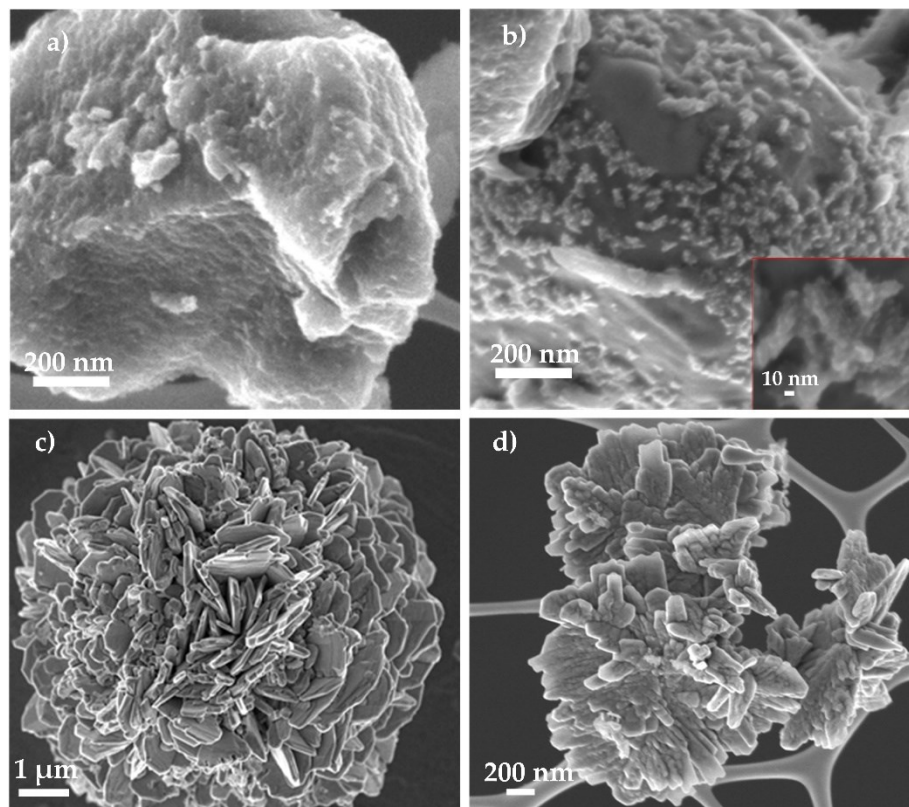


Figure 27: Comparison between a) CND_T0 (100kX) and b) Cu_CND-T0 (100 kX) particles surface with detail on Cu nanostructures (500kX); c) flower-shaped (25kX) and d) irregular (50kX) CuO particles.

EDS analyses confirmed the absence of metals in the carbon samples (CND_T0, CND_T1, CND_T2). No nitrogen was found in the case of CND_T0. On the other hand, CND_T1 showed a massive presence of nitrogen in bulk, while sample CND_T2 showed concentrations around 1% at.

The EDS analysis performed for the Cu_CND_T0 sample reveals a high metal presence. No oxygen is detected, as confirmed by XRD measurement. Therefore, it is possible to exclude the presence of Cu₂O or CuO in bulk. It was expected to have a 30% wt of Cu in the carbon structure, as it was the theoretical amount in the precursors. However, the different zones analysed for that sample present a 1.64% of Cu higher than C. It could be attributed to the inhomogeneity of the sample due to the synthesis process, which involved

the mixing of two micrometric powders, which led to aggregation and coalescence of the copper.

Lastly, as expected, CuO shows only oxygen and copper with an atomic ratio of 1 to 1. **Table 7** collects the EDS results.

It should be noted that it would be better to refer to XPS analyses for the composition of nitrogen carbon-based materials since the carbon and nitrogen peaks could overlap due to their vicinity not allowing precise identification of nitrogen content with EDS (Massardier et al., 2001).

Table 7: EDS results.

Sample	%At			
	C	N	O	Cu
CND_T0	96.77	0	3.23	0
CND_T1	53.19	46.8	0	0
CND_T2	98.95	1.04	0	0
Cu_CND_T0	37.8	0.5	0	61.8
CuO	0	0	51.65	48.34

6.1.4 Raman spectroscopy

Raman spectroscopy was used to investigate the order degree and the nitrogen content of the nitrogen-doped carbon catalysts. The resulting data are summed up in **Table 8**, and the spectra are shown in **Figure 28**.

To evaluate the order degree of carbon structures, the D and G bands are of particular interest, which in this case are identified as peaks at 1330 cm^{-1} and about 1560 cm^{-1} , respectively.

The G band results from the planar vibrations of the sp^2 hybridised carbon atoms. It is related to the graphitic domains. The D band is associated with the disorder in the graphite-like structure and originates from out-plane vibrations sp^3 -like defects.

The ratio between the intensity of these two bands ($I_{D/G}=I_D/I_G$) is a measure of the carbon structure order, it relates to sp^3/sp^2 ratio and depends on multiple factors such as the degree of graphitization, the presence of heteroatoms, and in case of porous carbons also on the presence of pores and the surface area.

The CND_T0 and CND_T2 samples show lower indices than CND_T1, $I_{D/G}$ equal to 1.65, 1.68, and 2.03, respectively, suggesting a greater degree of order.

Despite the remarkable difference between the surface areas between the former two, the indices are similar, as crystallinity and nitrogen content, and therefore a correlation between the surface area and the degree of order can be excluded.

Instead, it is attributable to the crystallinity and nitrogen content, higher temperatures, or time (slower heating rates) of treatment leading to higher crystallinity with graphitic-like

microcrystallites, as also highlighted by the XRD analysis. The introduction of nitrogen causes a local distortion of the bonds in the graphitic sheets due to the differences in the atomic mass, radii, and electronegativity between carbon and nitrogen atoms (J. Wu et al., 2015). The intensity values of the I C-N band suggest a high presence of N in the CND_T1 sample, which constitute defects in the lattice and combined with its completely amorphous structure, explain its lower degree of order. However, when compared with other graphitic materials (for ideal graphene $I_{D/G}$ is about 0), all the samples show high indices confirming a low order degree which originates from nitrogen doping, defects, low graphitisation degree, and structure voids due to porosity.

Lastly, it should be noted that the CND_T1 sample still has a greater intensity of the G band than the other samples. The nitrogen content, the number of defects and distortion, can favour the formation of sp^2 clusters (Ray et al., 2014), consistent with the high number of pyridinic groups reported in the next section.

Table 8: Raman spectroscopy results.

Sample	I_D	I_G	$I_{D/G}$	G (cm^{-1})	I C-N band
CND_T0	321.91	189.66	1.65	1560	175.06
CND_T1	504.9	248.71	2.03	1558	254.27
CND_T2	141.25	84.14	1.68	1551	85.09

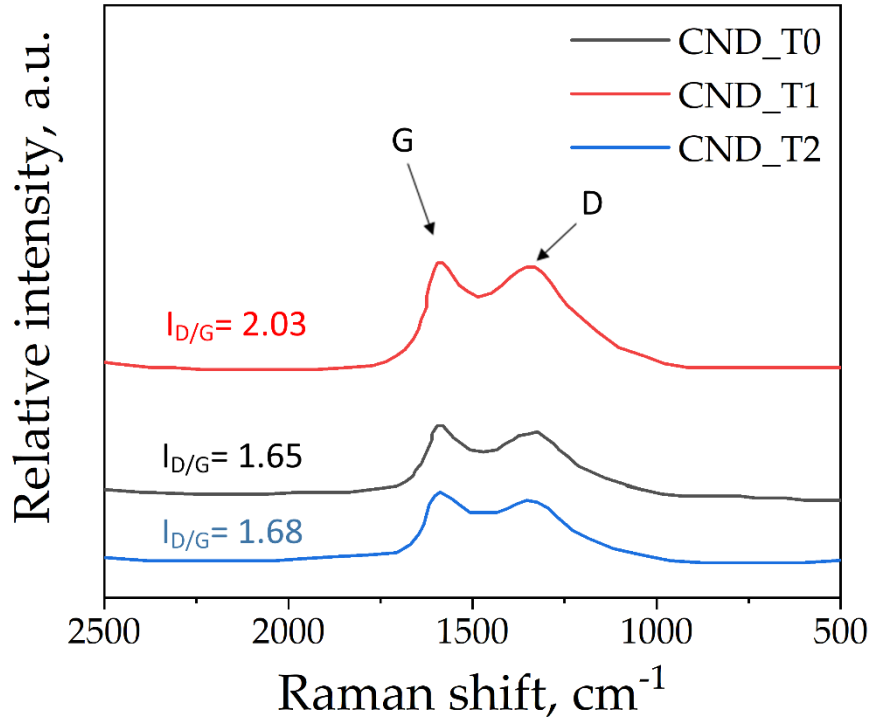


Figure 28: Raman spectra of CND samples.

6.1.5 X-ray photoelectron spectroscopy

Table 9 shows the superficial composition of the samples in atomic percentage. The analyses confirmed the absence of metals in the CND samples, while in the case of Cu_CND_T0 and CuO, only copper was detected (Na excluded, present in less than 2 % at possibly residual due to the synthesis process).

Table 9: Composition of samples in atomic percentage (%at).

Sample	C	O	N	Cu
CND_T0	83	12.1	2.5	–
CND_T1	75	12.5	10.6	–
CND_T2	81	13.7	2.4	–
Cu_CND_T0	73.6	18.3	4.4	1.3
CuO	45.2	34.7	3	17.1
CMK-3-600	78.6	8.4	11.3	–
CMK-3-750	79.1	8.9	8.3	–

A low nitrogen concentration was detected for all the samples. The atomic concentration of N is equal to 2.4 and 2.5% for the CND_T0 and CND_T2 samples compared to 10.6% for the CND_T1 sample, confirming the trend found with the Raman spectroscopy analysis.

The nitrogen content is strongly affected by the carbonisation treatment. It decreases by increasing the treatment temperature and duration while the thermal ramp has negligible effects or rather influences through time modification (Long et al., 2015). Therefore, the lower time and temperature of the treatment T1 would be responsible for greater nitrogen incorporation in the carbon framework.

In addition to the content, the atomic configuration of nitrogen was also investigated. The results are shown in **Table 10** and **Figure 29**.

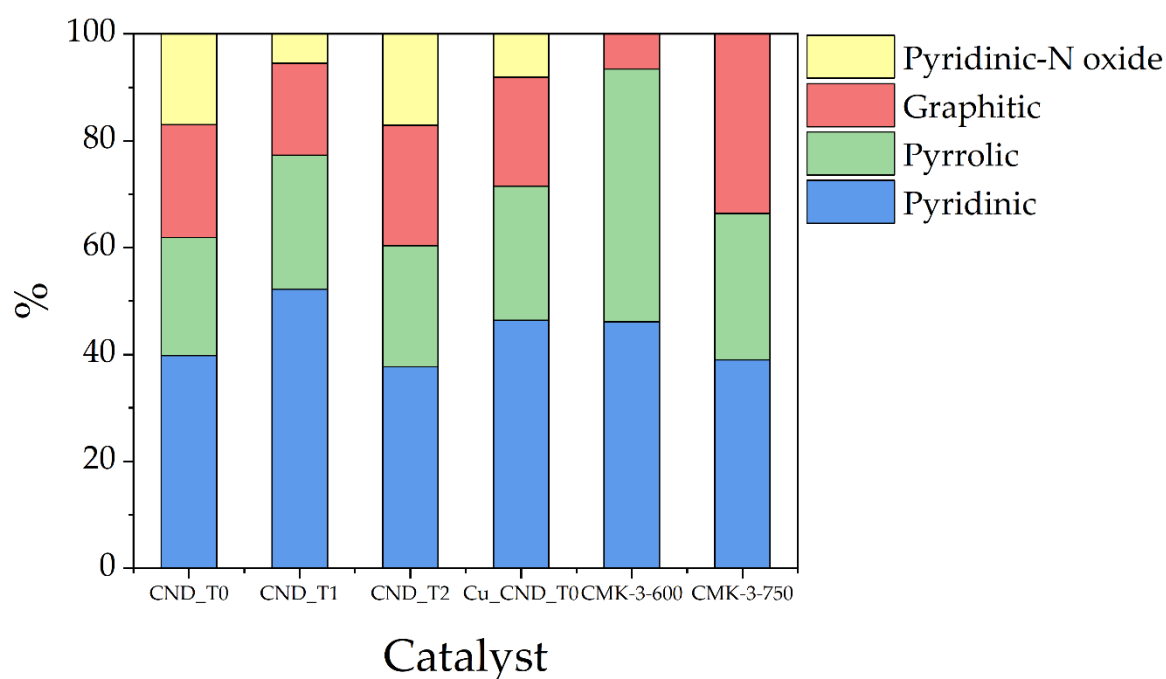


Figure 29: Visual representation of N-species percentage.

Table 10: Nitrogen species percentage.

Sample	Pyridinic	Pyrrolic	Graphitic	Pyridinic-N oxide
CND_T0	39.8	22.1	21.1	17
CND_T1	52.2	25.1	17.2	5.5
CND_T2	37.7	22.7	22.5	17.1
Cu_CND_T0	46.4	25.1	20.4	8.1
CMK-3-600	46.1	47.3	6.6	–
CMK-3-750	39.0	27.4	33.6	–

The deconvolution of the N1s peak (see **Figure 30**) highlighted the presence of several nitrogen species, the peaks at 398.5, 400.1, and 401 eV correspond to pyridinic, pyrrolic,

and graphitic nitrogen, respectively. Pyridinic nitrogen is the prevalent species for all samples with 52.2 % in CND_T1, remarkably higher than 39.8 % and 37.7% for CND_T0 and CND_T2, respectively. The carbonisation temperature also affects the atomic configuration. Higher temperatures favour the conversion of the less stable species to more stable ones promoting the transformation of pyridinic/pyrrolic groups into quaternary nitrogen (J. Wu et al., 2016).

This trend is visible in the CMK-3 samples, the samples treated at 600 °C show more pyridinic and pyrrolic groups than the sample CMK-3-750, which shows much more graphitic-N. It is not true for CND samples. While there is a slight decrease in the concentration of pyrrolic nitrogen for the samples treated at higher temperatures or for a longer time, the graphitic-N content is almost similar for all three catalysts.

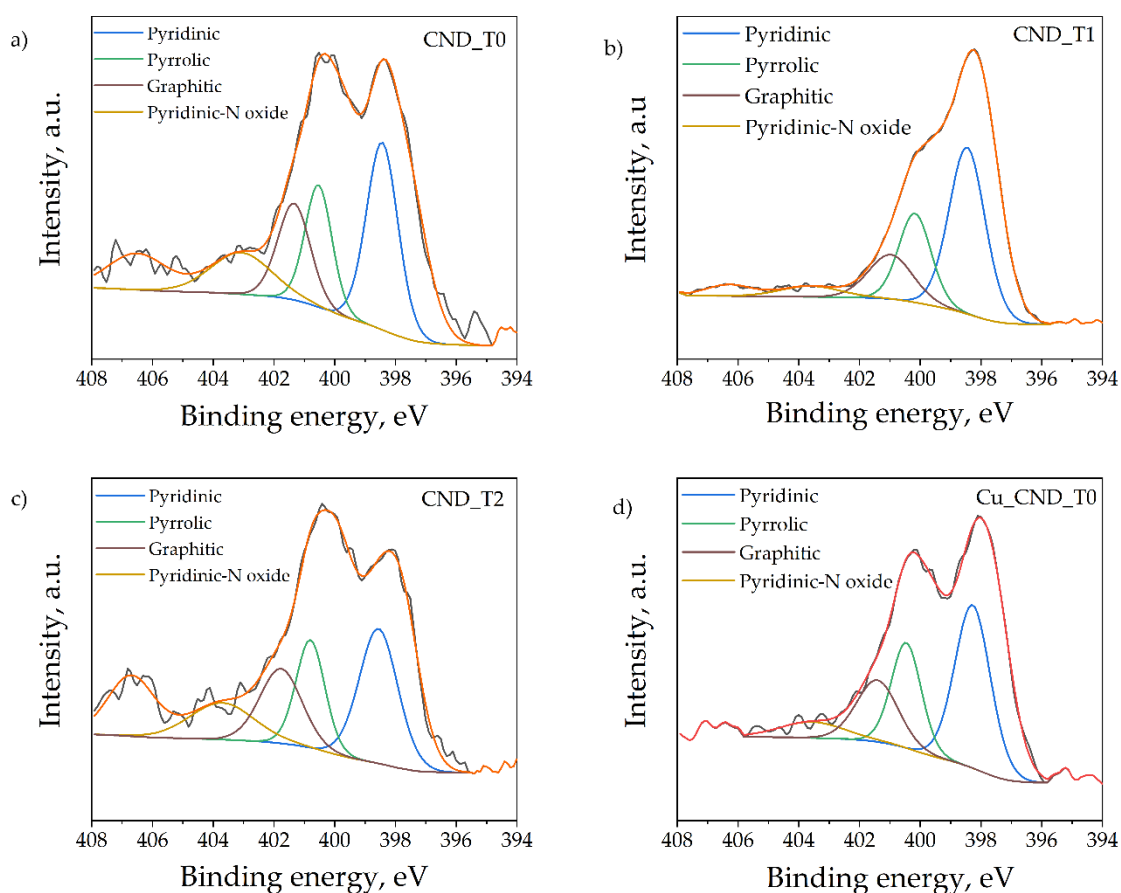


Figure 30: *N1s* profile for a) CND_T0, b) CND_T1, c) CND_T2, and d) Cu_CND_T0.

Figure 31 shows the analysis of the C1s spectra. A greater presence of sp^2 carbon species can be found in the case of the carbons with a greater degree of order, while the CND_T1 sample shows a greater number of sp^3 like defects. CND_T0 and CND_T2 C1s spectra are almost overlapped while the CND_T1 one deviates more, the number of defects or C atoms bonded to different atoms, such as nitrogen, increases from T0 to T1, confirming what was said in the previous sections.

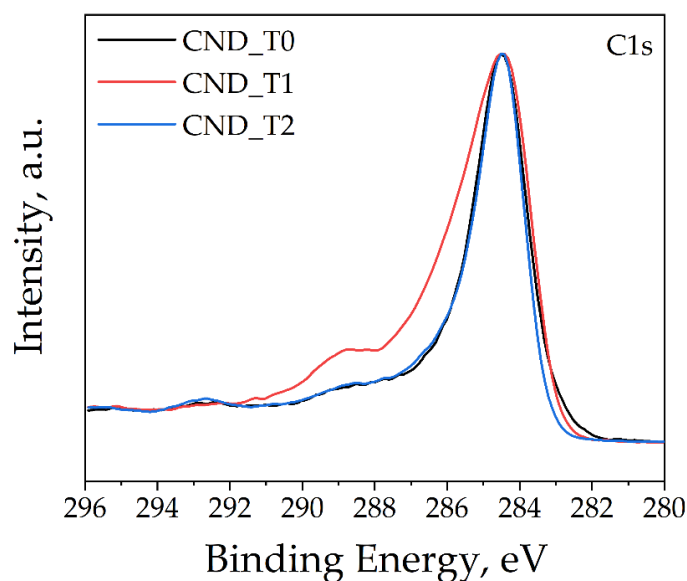


Figure 31: Comparison of C1s spectra of CND metal-free carbon samples.

The introduction of copper in the CND_T0 carbon caused an increase of nitrogen content of up to 100%, obtaining a 4.4%at for the Cu_CND_T0 sample. The higher nitrogen content is probably favoured by interactions with the metal (Y. Ni et al., 2017). Also, in this case, the nitrogen species present in greater quantities is pyridinic nitrogen (see [Figure 30d](#)). The Cu2p doublet spectra, determined in the high-resolution mode, display a typical spectrum mainly related to CuO, which is clearly visible thanks to the presence of the Cu²⁺ satellite at 940–945 eV (not shown here). The Cu²⁺ state has been already observed in bulk with the XRD analysis. The deconvolution procedure of the Cu2p spectra results is complex due to the overlapping of binding energies of the different Cu oxidation states. However, following the method developed by Biesinger et al. was possible to evaluate the ratio between CuO and Cu+Cu₂O by fitting the Cu2p_{3/2} peak and its related satellite. The results revealed that the Cu_CND_T0 presents 70% of CuO. From the C1s and N1s spectra, shown in [Figure 32](#), it is possible to exclude different bonds between Cu and N (Cu-N_x) or with other atoms. The introduction of copper does not lead to the appearance of new peaks linked to different nitrogen species from the ones present in metal-free samples while from the carbon spectra appears a negligible increase of order in case of Cu_CND_T0. Therefore, the CuO state could be due to surface oxidation of the metallic copper after exposure to the atmosphere. The remaining 30% is present in the Cu₂O and metallic copper forms.

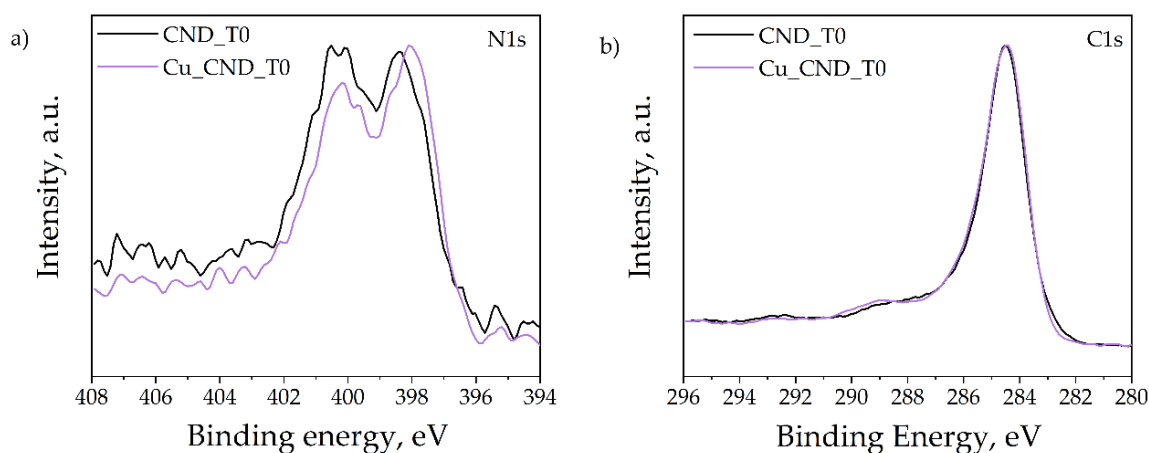


Figure 32: a) N1s and b) C1s peaks of Cu_CND_T0 and CND_T0 samples.

The XPS analysis of copper oxide showed a high presence of adventitious carbon in the forms C–C, C–O–C and O–C=O, probably due to contamination following exposure to the atmosphere. In addition to this, it confirmed that the composition of the CuO sample is mainly of copper oxide (88% Cu(II)) while the remainder is a mixture of metallic copper and Cu (I), whose formation is possibly due to exposure to X-rays during the test (C.-K. Wu et al., 2006).

6.2 Electrochemical behaviour of the synthesised N-doped carbon

6.2.1 Preliminary activity tests with RDE system

Based on the physico-chemical characterisation performed on the studied materials, preliminary electrocatalytic tests were carried out on CND_T1 and CND_T2 to verify their activity. The main idea was to evaluate the electrochemical behaviour comparing samples with different surface areas, order degrees, nitrogen content (especially pyridinic groups). For convenience, **Table 11** sums the value of these parameters for the chosen samples.

Table 11: Physical characterisation results for samples CND_T1 and CND_T2.

Sample	SSA _{BET} (m ² g ⁻¹)	I _{D/G}	N (%at)	% N-Pyridinic
CND_T1	446	2.03	10.6	52.2
CND_T2	328	1.68	2.4	37.7

CVs in N₂ and CO₂ and LSVs in CO₂ are reported in **Figure 33** and **Figure 34**. The noise at high potentials is inevitable; it is possibly originated from the uneven diffusion of CO₂ molecules at high current densities (W. Xie et al., 2021).

In both samples, CV curves performed while bubbling CO₂ reach lower current densities than in N₂. Generally, it means a higher catalytic activity towards HER than for CO₂RR. However, it could also be due to the adsorption of carbon dioxide molecules on the carbon

surface inhibiting the current for potentials higher than -0.8 V vs RHE (Pérez-Rodríguez et al., 2017).

There are no evident reduction peaks for both catalysts. There is an inflexion starting from -0.8 V vs RHE in the CO₂ curves, while in the nitrogen curves around -0.7 V, in the N₂ voltammetry, the CND_T1 sample shows an onset slightly more positive and reaches higher current densities equal to 68 mA cm⁻² compared to 61 mA cm⁻² of CND_T2. It could be ascribed to the larger surface area of the former. For both samples, CO₂ cyclic voltammetry shows maximum current densities around 60 mA cm⁻² and overlapped branches (see [Figure 34a](#)), indicating the lower activity towards the CO₂ reduction reaction (Song et al., 2017).

As aforementioned in section 2.1, the onset potential in CO₂RR is not strictly determined by a bend in the curve (steep increase of the current), and it is possible to yield reduction products at lower potentials than the detected reduction peaks.

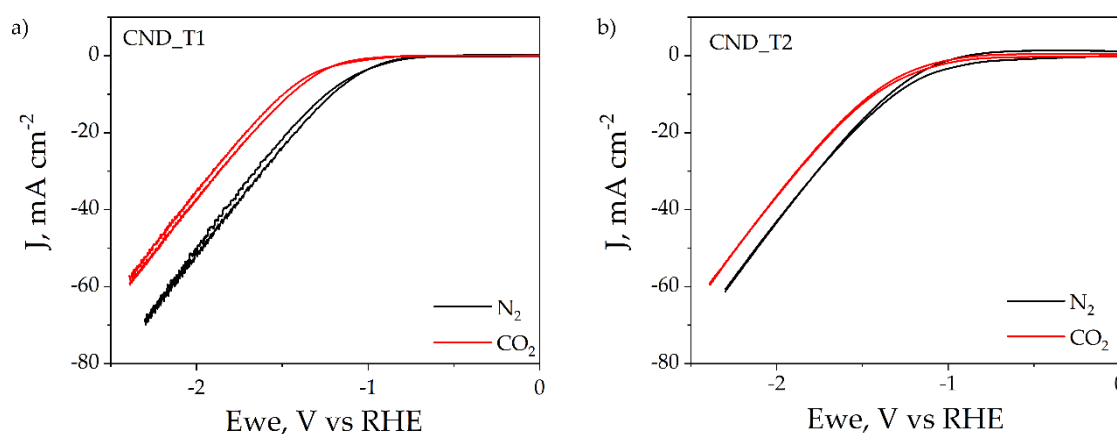


Figure 33: CVs in N₂ and CO₂ for a) CND_T1 and b) CND_T2.

From the LSV (see [Figure 34b](#)), it can be seen again that the CND_T1 catalyst reaches higher maximum current densities at the same potential, as noted above in the case of the cyclic voltammetry under nitrogen. The explanation could lie in a greater conductivity of the CND_T1 sample than CND_T2, contrary to what one might expect based on the degree of crystallinity, due to the greater nitrogen content whose introduction into the structure has a positive effect on the conductivity of amorphous carbons (Ray et al., 2014).

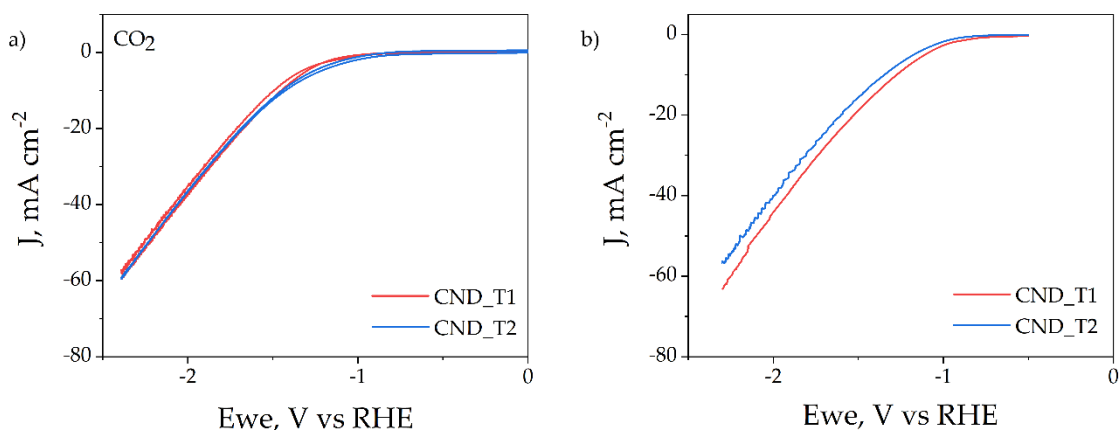


Figure 34: a) CVs and b) LSVs in CO₂ of both samples.

Based on the LSV results, it was decided to test the CO₂ reduction activity with a CP, shown in **Figure 35**, supplying a current corresponding to a potential of -1.6 V vs RHE, a more negative potential to ensure catalytic activity. Maintaining this current density required a slightly higher potential in the CND_T1 sample, which preserved a constant current over the two hours, a possible indicator of greater stability.

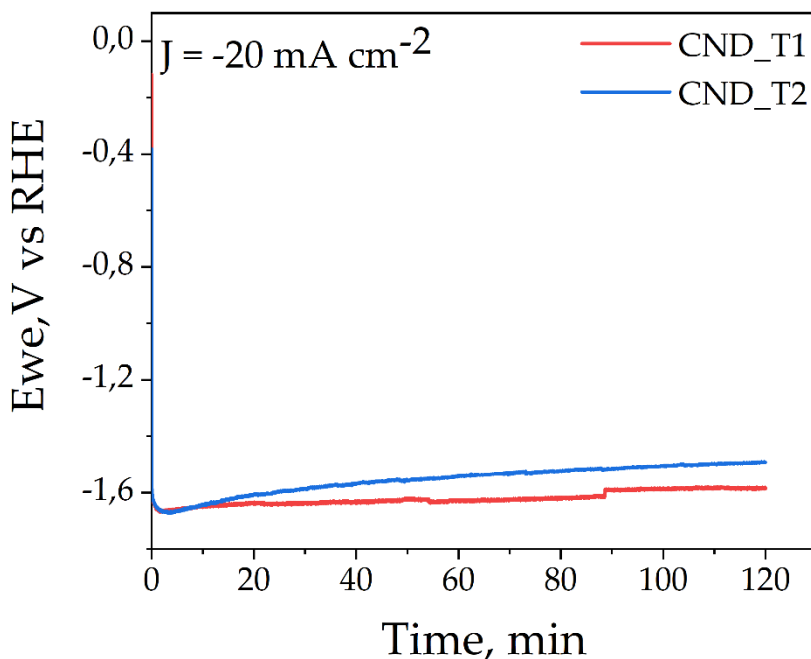


Figure 35: Electrochemical CO₂ reduction testing chronopotentiometry.

The only gaseous products detected were hydrogen and carbon monoxide, whose evolution during the CP is shown in **Figure 36a**, while the corresponding Faradaic efficiencies are shown in **Table 12**. For both samples, higher hydrogen production than CO was found with Faradaic efficiencies of 70% for CND_T1 and 79% for CDN_T2, which

confirms the weak catalytic activity towards CO₂RR. The concentration of the gaseous products was approximately constant for the test duration, suggesting the stability of both catalysts for 2 hours.

Regarding the liquid products, the Faradaic efficiencies are collected in **Figure 36b**. As it is possible to see, C₂₊ products like ethanol and 2-propanol were detected in the case of CND_T1. For the CND_T2, in addition to those, methanol, acetone and COOH were also relieved. In the case of ethanol, both samples have very low efficiencies of approximately 0.2 %. The largest liquid product was isopropanol in the case of the CND_T1 sample, achieving a FE of approximately 2% and productivity of 1.3 mmol h⁻¹g⁻¹. For CND_T2, it was formate with 19 mmol h⁻¹ g⁻¹ and FE of 3%. In any case, the productivity of liquid products was very low and is collected in **Table 13**.

Based on the results obtained despite the weak catalytic activity towards CO₂, the CND_T1 sample would seem inclined to yield multi-carbon products. In fact, the CND_T1 catalyst seems to promote the formation of the intermediate *COOH, which evolves towards CO and then towards C₂₊ products through dimerization mechanism. It could be attributed to the greater presence of pyridinic groups, while CND_T2 could enhance the *OCHO intermediate and therefore, COOH formation, as shown in **Figure 6**. For this reason, it was decided to conduct further tests employing the CND_T1 as catalyst. Furthermore, as reported in section 5.4.1, based on the low productivity, the tests were performed using electrodes made onto carbon paper.

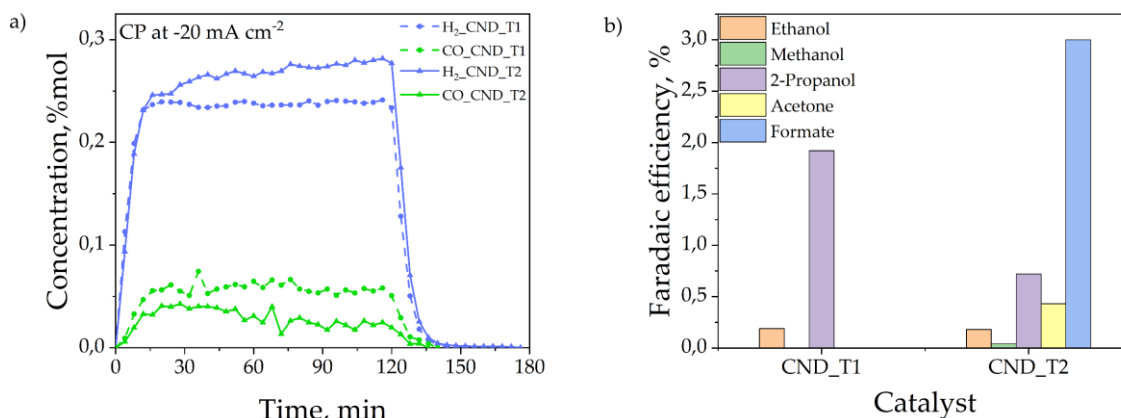


Figure 36: a) Evolution of gaseous products during CP, and b) Faradaic efficiencies at -1.6 V vs RHE of the obtained liquid products.

Table 12: FE for gaseous products at -1.6 V vs RHE.

Sample	FE H ₂ %	FE CO ₂ %	CO/H ₂
CND_T1	70.95	16.85	0.24
CND_T2	79.63	8.29	0.104

Table 13: Liquid products productivity.

Sample	Productivity (mmol h ⁻¹ g ⁻¹)				
	Formate	Methanol	Ethanol	Acetone	2-Propanol
CND_T1	0	0	0.2	0	1.3
CND_T2	19	0.1	0.18	0.3	0.5

6.2.2 Electrochemical activity of carbon paper working electrodes

The tests were performed at lower potentials since they would seem to favour the production of hydrocarbons, alcohols, and organic acids (Pérez-Rodríguez et al., 2017) through the unblocking of reaction pathways otherwise thermodynamically disadvantaged. In addition, the CMK-3 samples were tested to ascertain the effect of the different structures shown in [Figure 9](#). The electrocatalytic activity of the bare copper (CuO) sample was investigated to understand the possible synergies between the precursors to prepare the Cu_CND_T0 material.

[Figure 37](#) shows the CVs in nitrogen and CO₂. [Figure 38](#) shows the comparisons between the CVs in CO₂ and CVs with normalized current densities with respect to ECSA for carbonaceous samples, copper-based samples, and CMK-3 samples. The calculated ECSA values are instead shown in [Table 14](#).

In general, the current densities are lower than those recorded during RDE preliminary tests due to the different charge and mass transport resistances and the larger area of the electrodes (1 cm² for carbon paper electrodes vs 0.1962 cm² for RDE). It is important to mention that fabricating a larger electrode does not guarantee a uniform current density.

The CND_T1 sample shows higher currents than the CND_T0 and the CMK-3 materials. The curve under CO₂ has a lower onset potential than under nitrogen. The two samples have comparable ECSA values of approximately 3.8 cm².

For samples with copper (see [Figure 38b](#)), the currents reached are higher than those without, suggesting higher conductivity induced by the metal. The fact that the current densities under CO₂ are lower than those under nitrogen could be attributed to the inhibition of the current based on the effect explained in the previous section. Copper samples have lower ECSA than metal-free carbon. The lower value can be explained by a lower exposure of the active sites due to the absence of porosity for CuO, while in the case of Cu_CND_T0, the introduction of copper and the formation of nanoparticles could have reduced the surface area and thus induced a similar effect. However, in the absence of nitrogen adsorption analyses, these remain hypotheses.

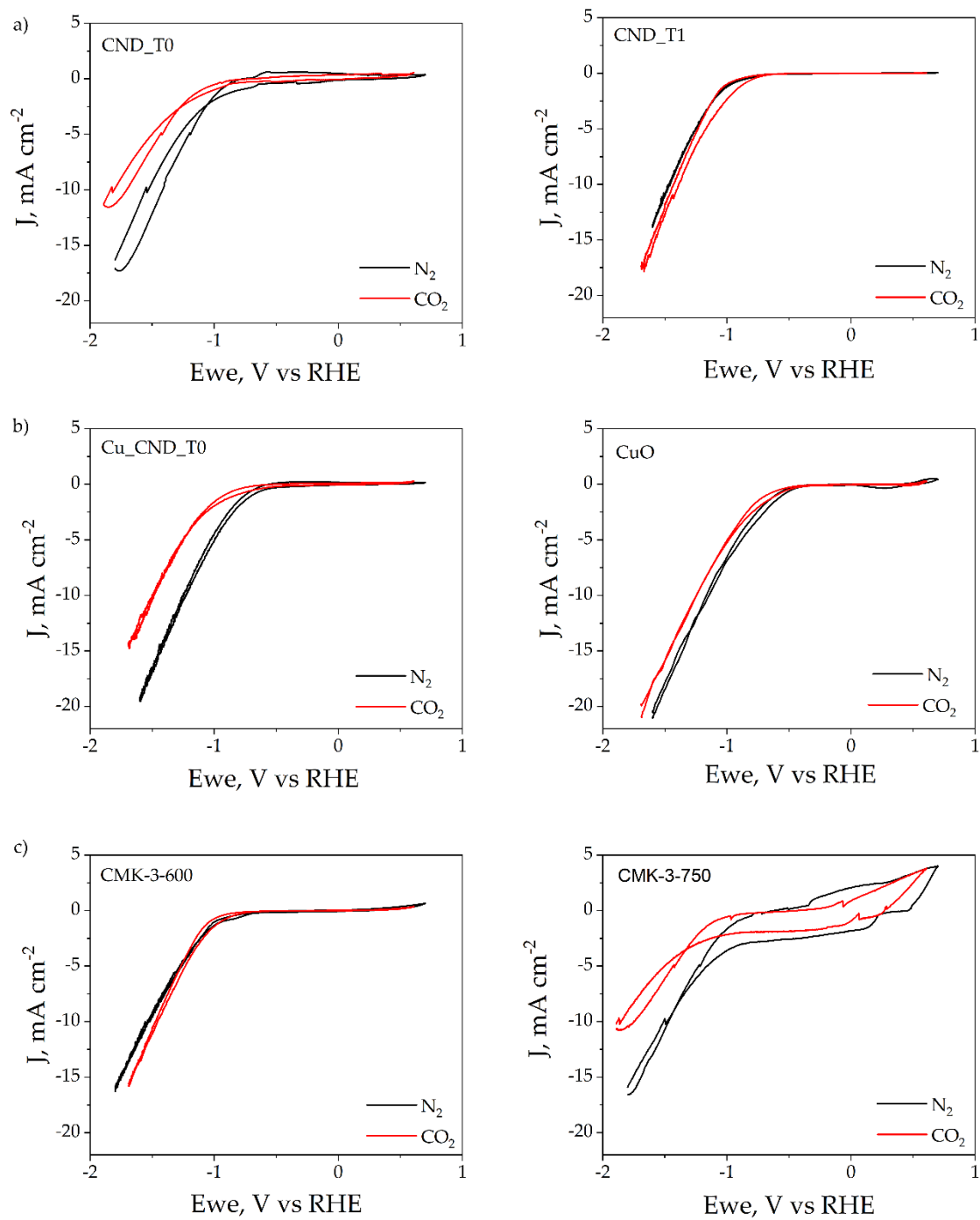


Figure 37: CVs in N_2 and CO_2 for a) metal-free CND samples, b) copper samples, and c) CMK-3 samples.

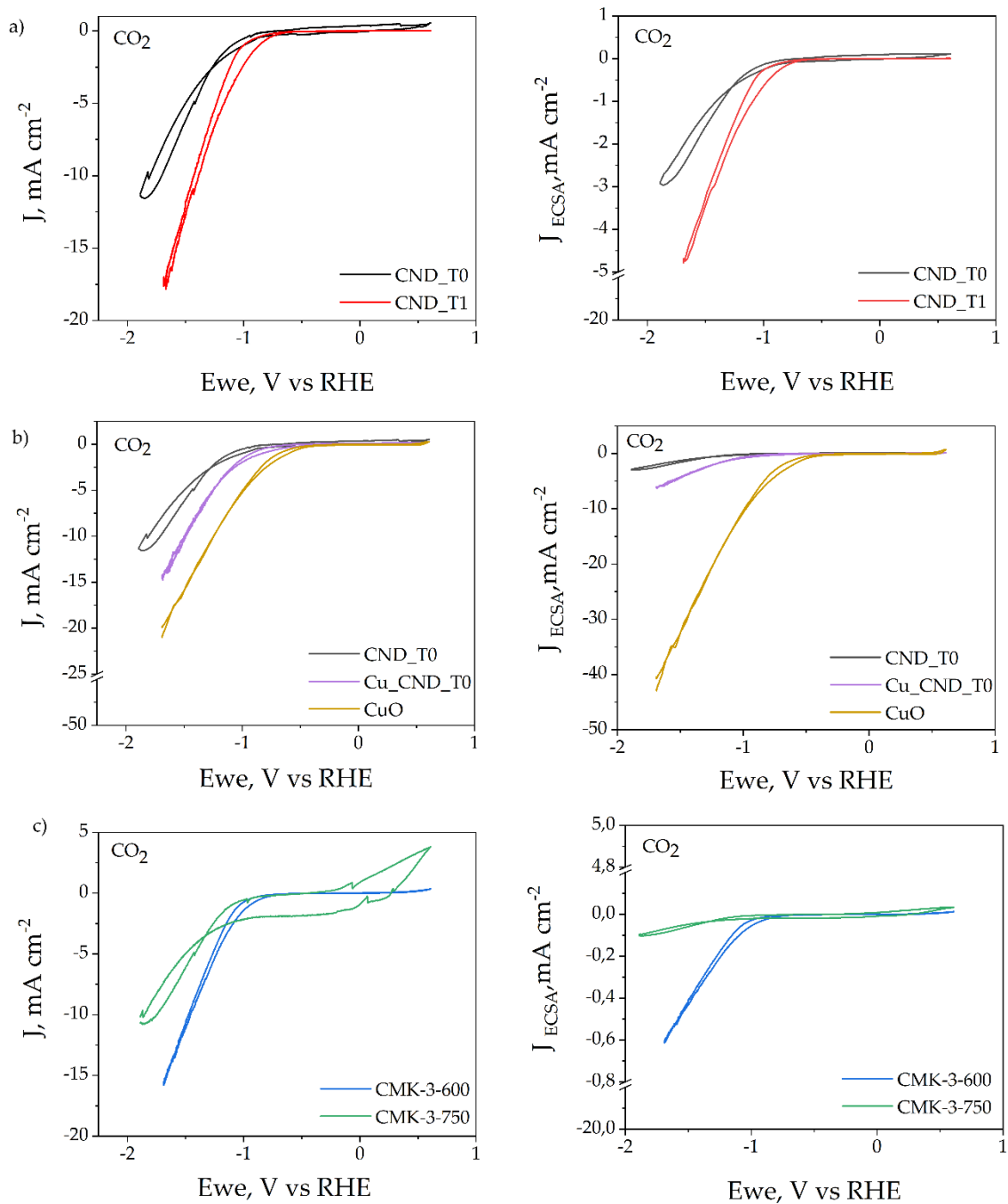


Figure 38: CVs in CO₂ without (left) and with normalized current with ECSA (right) for a) metal-free CND samples, b) copper samples, and c) CMK-3 samples.

Table 14: ECSA calculated values.

Sample	ECSA (cm ²)
CMK-3-600	25.8
CMK-3-750	105
CND_T0	3.9
CND_T1	3.7
CND_T2	17.3
Cu_CND_T0	2.3
CuO	0.5

The catalytic activity for CO₂ was then studied using a CA measurement, shown in [Figure 39](#), and performed as explained in the previous sections. In general, very low current densities are achieved at low potentials, between 0.02 and 0.15 mA cm⁻² for -0.4 V, and 0.04 mA cm⁻² for CND_T0 and 0.8 mA cm⁻² of sample CuO at -0.6 V vs RHE.

CuO and CND_T1 show the largest current densities at high potentials, equal to 7 and 6 mA cm⁻² respectively, suggesting greater catalytic activity and conductivity, followed by the Cu_CND_T0 sample with 2.5 mA cm⁻².

The CND_T0 and CMK-3 samples instead show the lowest current densities at all potentials reaching maximum values at -1 V vs RHE, equal to 0.8 mA cm⁻² for CND_T0 and CMK-3-750 and 1.3 mA cm⁻² for CMK-3-600.

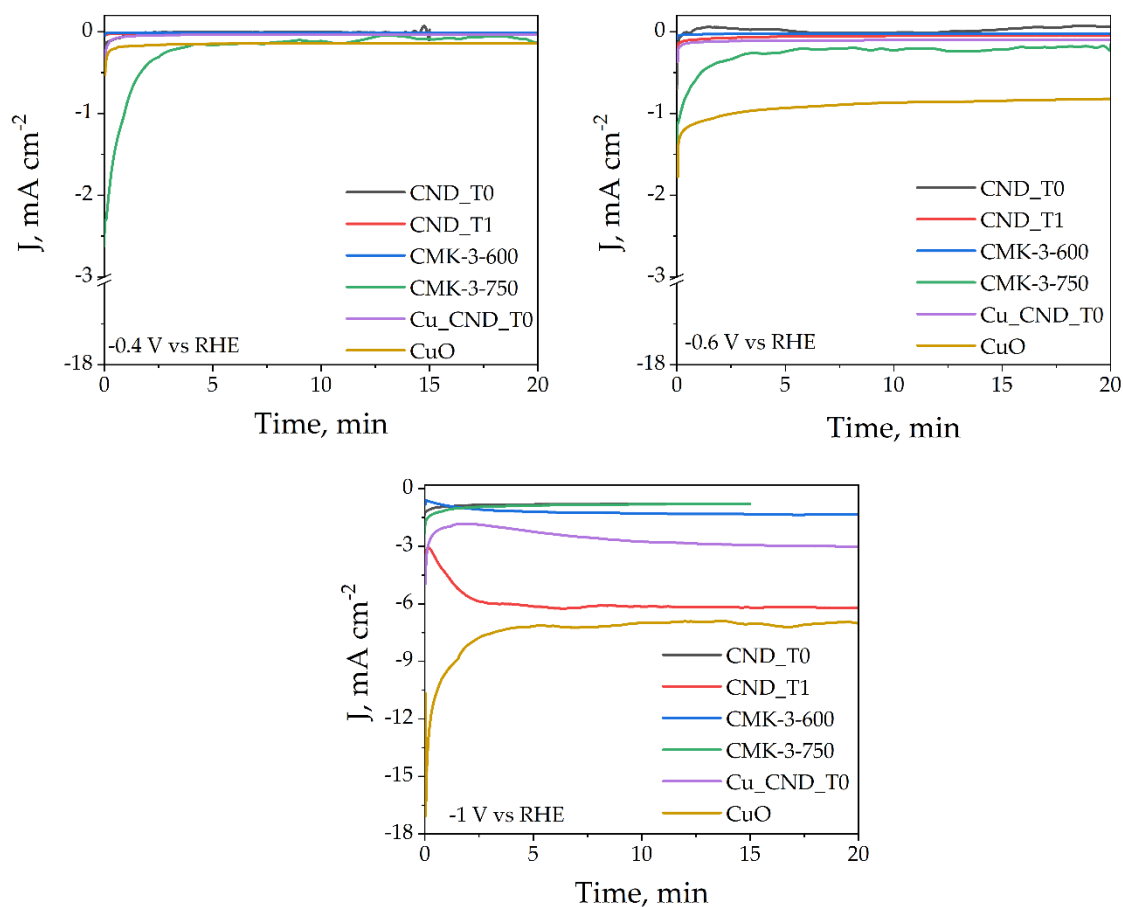


Figure 39: CA in CO₂ at -0.4, -0.6, -1 V vs RHE.

The Faradaic efficiencies of the gaseous products are shown in **Figure 40** and summarised in **Table 15**. In comparison, the productivities of liquid products are collected in **Table 16** and **Figure 41**.

Table 15: FE of gaseous products.

Potential (V vs RHE)	FE H ₂ %						FE CO %	
	CND_T0	CND_T1	Cu_CND_T0	CuO	CMK- 3-600	CMK- 3-750	Cu_CND_T0	CuO
-0.4	0	0	22.6	80.5	0	2	0	0
-0.6	0	45.5	82	95	0	21	0	8.6
-1	28	98.7	97	57	97.5	42	2.1	5.8

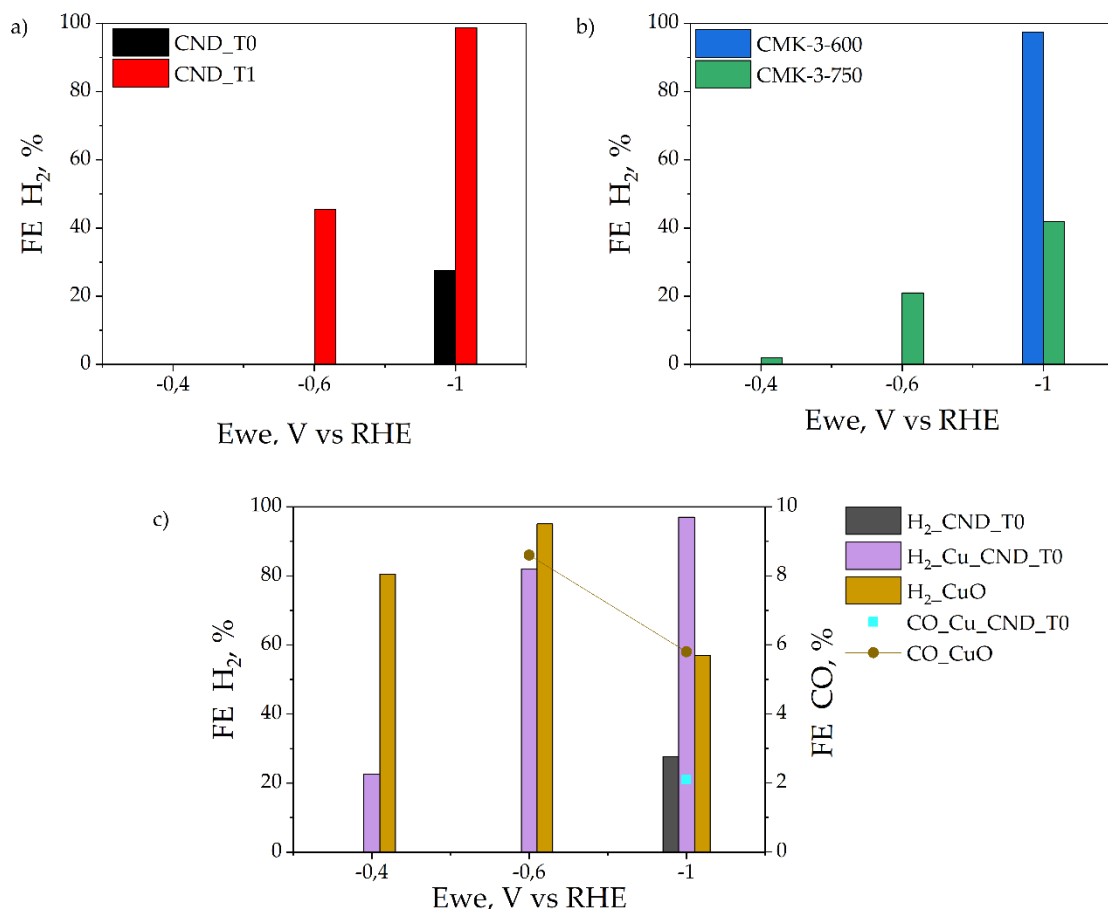


Figure 40: FE of gaseous products for a) CND metal-free carbon samples, b) CMK-3 samples, and c) copper samples.

The metal-free samples (CND) have only hydrogen as a gaseous product, contrary to what has been seen in the RDE measurement. It could be referred to the minor potentials applied that would favour the retention of the *CO intermediate and its further reduction. At the potential -0.4 V vs RHE, there is no production of any gaseous product. It could be due to the absence of catalytic activity or the production of only liquid products. Increasing the applied potential, they showed a higher selectivity towards hydrogen production, reaching a FE close to 100% at -1 V vs RHE, in the case of CND_T1. The higher bubbles production coming from hydrogen production hinders the adsorption of CO₂ molecules on the catalyst, inhibiting its reduction (Song et al., 2016).

On the other hand, for copper-based electrodes, CO was favoured. The CuO sample shows a high Faradaic efficiency for hydrogen at lower potentials, as the potential increased to -0.6 vs RHE, the CO production increased. However, a further increase in potential resulted, both the FE of hydrogen and CO decreased, probably because it became more selective to liquid products.

The copper sample Cu_CND_T0 is more catalytically active than the copper-free counterpart CND_T0 in terms of HER and CO₂ reduction. It is the only carbon-based sample capable that was able to produce CO, albeit with very low efficiencies (2%) at high potentials.

In **Figure 40**, CMK-3-600 shows no production of H₂ at -0.4 and -0.6 V vs RHE, possibly meaning higher CO₂RR than CMK-3-750, which, however, shows lower H₂ FE than the metal-free CND samples suggesting a higher selectivity for CO₂ reduction.

In general, for all carbon-based samples, it is noted that the production of gaseous products increases as the applied potential increases. This trend is not true for the CuO-based sample, which shows higher efficiencies at intermediate potentials suggesting a different catalytic activity compared to carbon-based samples.

Regarding the liquid products, the faradaic efficiencies are listed in **Figure 42** and **Table 17**. All the samples have relatively low Faradaic efficiencies. In general, the highest productivity was reached for the formate production. CMK-3 samples showed very low productivity when compared with the other samples. The CND_T0 sample showed high selectivity towards formate with an FE of 72.6%, while the production of C₂₊ products is negligible. The introduction of a higher nitrogen content (CND_T1) or copper (Cu_CND_T0) is favourable for improving the catalytic activity and the selectivity towards more reduced products such as methanol and ethanol even if the main product remains formate. Cu_CND_T0 shows the highest faradaic efficiency for ethanol, equal to 18%.

The high selectivity towards HCOO⁻ of the CND_T0 sample compared to the CND_T1 sample, as well as the difference in terms of nitrogen content, could be attributed to the crystallinity of the carbon. The results obtained both with the preliminary tests in RDE and in these tests would suggest that an increase in crystallinity favours the selectivity and efficiency towards *COOH.

The CuO sample was selective towards the formation of formate with slight production of alcohols. CMK-3-600 sample showed a higher selectivity towards alcohols while CMK-3-750 sample towards formate. The difference could lie in the greater presence of pyridinic groups in the former. Despite the lower productivity, the CMK-3 samples evidenced higher faradaic efficiencies than the CND_T1 sample; the CMK-3-600 sample shows the greater efficiency for methanol, equal to 8.7 %. The different carbon structures could explain this effect. Carbons with a structure formed by cylindrical channels (CND) have greater productivity and conductivity; instead, the curvature of the pores of the nanorods structure would limit the formation of products, and the low number of contact points between the rods results in a lower conductivity leading to lower currents, and therefore a lower amount of charge used which goes hand in hand with low productivity. A cylindrical pore structure would therefore be more favourable to CO₂ reduction.

The application of copper on the carbon structure favours selectivity towards multi-carbon products; however, CuO has been synthesized by calcination without introducing features that could improve its catalytic activity.

Finally, it should be remembered that the faradic efficiencies were averaged over the three CAs and, therefore, not referable to a single potential. Based on this, it is not possible to verify whether the application of minor potentials favours the production of hydrocarbons, alcohols, and organic acids. Based on the results obtained, it is not possible to suggest which are the reaction pathways or the active sites in reducing CO₂.

Table 16: Liquid products productivity for carbon paper electrodes.

Sample	Productivity (mmol h ⁻¹ g ⁻¹)			
	Formate	Methanol	Ethanol	Acetone
CND_T0	9.22	0.24	0.07	0.02
CND_T1	3.67	0.51	0.64	0.15
Cu_CND_T0	4.95	0.4	0.85	0
CuO	14.5	0.05	0.35	0.06
CMK-3-600	0	0.18	0.07	0.002
CMK-3-750	0.7	0.12	0.06	0

Table 17: Liquid products FE for carbon paper electrodes.

Sample	Faradaic efficiency (%)			
	Formate	Methanol	Ethanol	Acetone
CND_T0	72.6	5.8	3.5	0.97
CND_T1	3.4	1.4	3.5	1.1
Cu_CND_T0	13.3	4.2	18	0
CuO	19.4	0.18	2.8	0.63
CMK-3-600	0	8.7	6.8	0.28
CMK-3-750	13.6	7	7.6	0.06

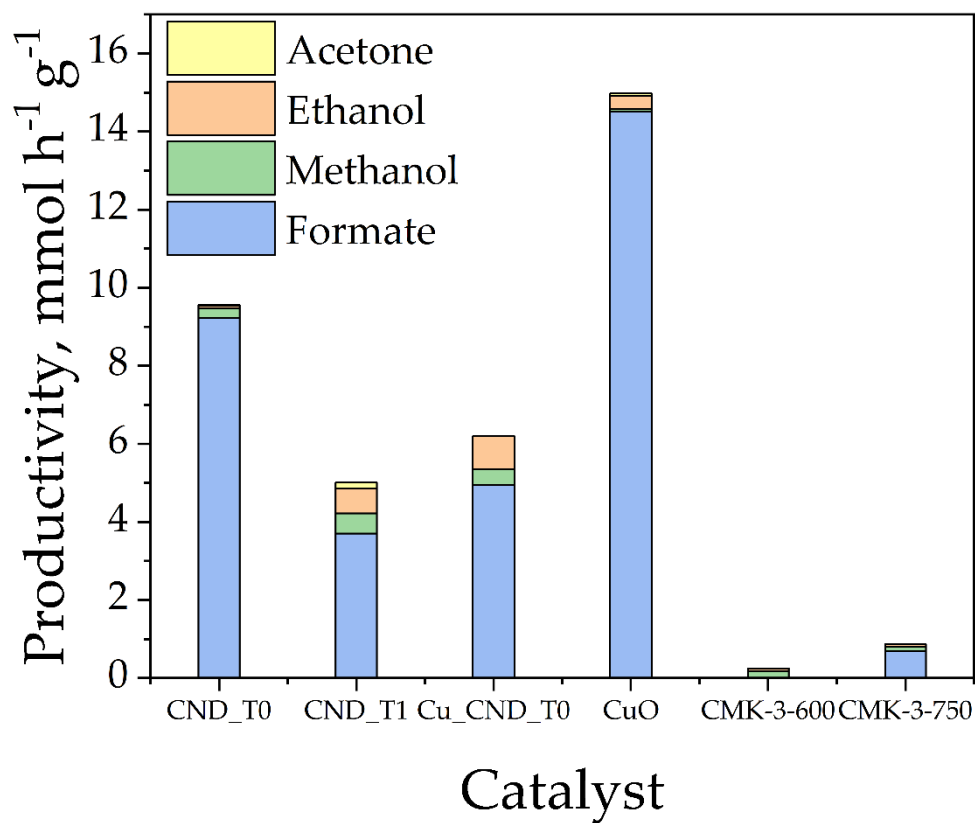


Figure 41: Liquid products productivity for carbon paper electrodes.

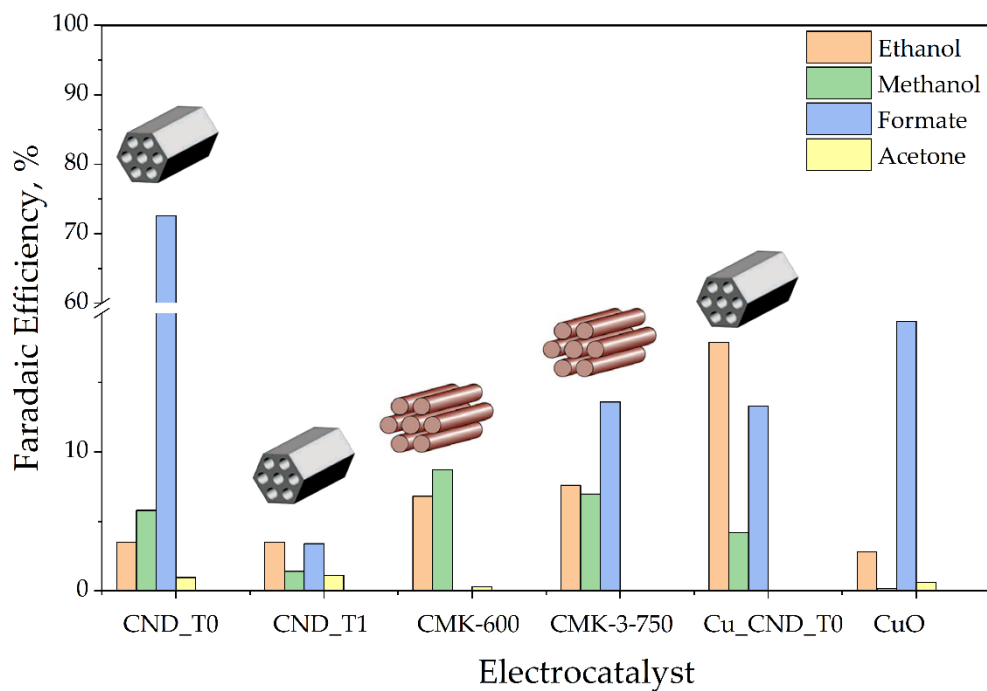


Figure 42: FE for liquid products with corresponding carbon structure representations.

7. Conclusions

In summary, using a soft template and the EISA method allowed the synthesis of mesoporous nitrogen-doped carbons with ordered cylindrical channels. Treatments with lower ramp rate and final temperature were favourable for the production of samples with a higher degree of order, higher surface area and more ordered porous structure, while slightly faster heating rates allowed greater incorporation of nitrogen at the expense of the degree of order. The former treatments also proved beneficial in catalytic activity, leading to achieve a Faradaic efficiency of 72% for formate production. Therefore, a more orderly structure and a more uniform mesoporousness would be beneficial for the increase in selectivity towards CO₂RR.

Higher nitrogen incorporation has shown positive effects in increasing the conductivity and the productivity of multi-carbon products even if the efficiencies remain low.

The grinding process was successful in introducing metallic copper in the form of crystalline aggregates on the surface of carbon particles, with a positive role in terms of CO₂ reduction towards alcohols and for the achievement of higher current densities. At the same time, no Cu-N_x groups were detected. The copper sample showed the greatest selectivity towards ethanol with an efficiency of 18%.

Finally, the investigation of the structure revealed that a structure of ordered cylindrical channels leads to greater productivity, catalytic activity, and current density than a structure of interconnected nanorods, probably due to better interactions given by the different curvature of the pores.

In general, all samples exhibit low current densities and higher selectivity towards HER, especially at high potentials. In contrast, CO₂ reduction could be favoured at low potentials. In any case, in this study, it was not verified the origin of the catalytic activity nor the role of the potential applied in the selectivity of the catalyst.

Anyhow, the synthesised samples did not meet the necessary requisites for suitability for commercial application.

8. Future perspectives

Nitrogen-doped porous carbonaceous materials have acquired increasing importance in the EC CO₂R scenario thanks to the combination of interesting qualities and the introduction of nitrogen which leads to the breakdown of electroneutrality by modifying the carbon charge distribution and spin symmetry. However, the origin of the catalytic activity and the identity of the active sites remains uncertain. Further advances are needed to understand better the activity of the active sites and the reaction paths on this type of material. The N species, major candidates as active sites for CO₂ reduction, have low binding energies towards *COOH thanks to the presence of charge dipoles, while their high spin density favours HER. Therefore, their ambiguous nature prevents the obtaining of high efficiency and selectivity catalysts for CO₂RR.

Different heteroatoms could be introduced in addition to nitrogen, such as sulfur and phosphorus, to bypass the limit mentioned above. Those could further modify the spin density in nitrogen-doped carbons, enhancing charge delocalization and introducing synergistic effects to improve the catalytic activity of these materials (F. Yang et al., 2021).

Another strategy could be the addition of metals to synthesise SAC, which in addition to allowing material savings, would lead to the appearance of new effects and M-N_x groups capable of directing the catalysts towards better performance.

However, when used at the atomic level, metals assume a different behaviour compared to their bulk counterpart, requiring further efforts for the correct identification of the reaction pathways and active sites, as well as the introduction of new techniques for better engineering and control of the structure and the active sites.

For greener synthesis processes, it would be desirable to abandon phenol progressively and fossil deriving precursors and reduce the use of organic solvents in favour of synthesis in the aqueous phase using raw materials deriving from biomass such as tannins, starch, cellulose (Kong et al., 2019).

Finally, most of the heteroatoms doped carbons deliver low current densities. The doping level could be improved to overcome this problem, the ECSA increased and the active sites atomic structure engineered optimizing their interactions with the reaction intermediates.

Furthermore, the use of a different electrochemical cell configuration, passing from the H-cells to the GDE, and the development of new solvents would favour overcoming the current limitations given by the low mass transport of CO₂ in an aqueous environment.

The utilisation of CO₂ by converting it into products with high added value holds great promise for the mitigation and averting of a climate crisis with devastating effects on the life of the planet; continuous progress in process understanding and the development of materials and systems are necessary to render EC CO₂R eventually industrially viable.

List of abbreviations

IPCC	Intergovernmental Panel on Climate Change
NASA	National Aeronautics and Space Administration
IEA	International Energy Agency
CCS	Carbon Capture Storage
CCU	Carbon Capture Utilisation
EC CO ₂ R	Electrochemical reduction of CO ₂
CO ₂ RR	Reduction Reaction of CO ₂
OER	Oxygen Evolution Reaction
HER	Hydrogen Evolution Reaction
FE	Faradaic Efficiency
ECSA	Electrochemical Surface Area
TOF	Turnover Frequency
GDL	Gas Diffusion Layer
GDE	Gas Diffusion Electrode
MEA	Membrane Electrode Assembly
NP	Nanoparticles
CNT	Carbon Nanotubes
RHE	Reversible Hydrogen Electrode
NHE	Normal Hydrogen Electrode
SHE	Standard Hydrogen Electrode
SAC	Single-atom Catalyst
CVD	Chemical Vapor Deposition
ALD	Atomic Layer Deposition
DFT	Density Functional Theory
XPS	X-ray Photoelectron Spectroscopy
CMK	Carbons Mesostructured from Korea
MCM	Mobil Composition of Matter

EISA	Evaporation-Induced Self-Assembly
CMC	Critical Micellar Concentration
CND	Carbon Nitrogen-Doped
IIT	Istituto Italiano di Tecnologia
SBA	Santa Barbara Amorphous
BET	Brunauer-Emmett-Teller
BJH	Barrett-Joyner-Halenda
XRD	X-ray Diffraction
FESEM	Field-Emission Scanning Electron Microscope
EDS	Energy dispersive X-ray Spectroscopy
UPO	Università del Piemonte Orientale
CV	Cyclic Voltammetry
LSV	Linear Sweep Voltammetry
CP	Chronopotentiometry
CA	Chronoamperometry
RDE	Rotating Disk Electrode
RRDE	Rotating Ring-Disk Electrode
GC	Glassy Carbon
HPLC	High-Performance Liquid Chromatography
OCP	Open Circuit Potential
SSA	Specific Surface Area

List of figures

Figure 1: Carbon capture storage and utilisation cycle. It is inspired by (Eren & Özkar, 2021).	2
Figure 2: Basic principle of Carbon capture storage. Courtesy of Piyush Choudhary and Clicinnovation.....	3
Figure 3: Carbon dioxide molecule, with carbon atoms in black and oxygen atoms in red.	4
Figure 4: Schematic concepts of 3-electrode (a) traditional cell, (b) H-cell, (c) Gas Diffusion Electrode cell and (d) Membrane Electrode Assembly for electrochemical CO ₂ reduction reactions. Adjusted from (Guzmán, Russo, et al., 2021).	8
Figure 5: Schematic representation of selectivity-based classification of mono metallic catalyst.	11
Figure 6: CO and HCOOH pathways and schematic pathways for methane, methanol and C ₂₊ products. Adjusted from K. Zhao & Quan, 2021.	16
Figure 7: Examples of pathways on copper for methane and methanol. Reaction pathways from (Cheng et al., 2015; X. Liu et al., 2019).....	16
Figure 8: Ethylene and ethanol reaction pathways from K. Zhao & Quan, 2021.....	18
Figure 9: Schematic representation of carbon samples with (a) cylindrical channels and (b) interconnected cylindrical nanorods.	20
Figure 10: Nitrogen atomic configuration in the carbon framework. Adjusted from (Singh et al., 2020).	21
Figure 11: Schematic illustration of hard templating (a) and soft templating (b).....	22
Figure 12: a) graphite and b) hard carbon structure. Adapted from (Dasgupta & Sathiyamoorthy, 2003).	24
Figure 13: Resin after removal of solvent a) before and b) after thermo-polymerisation, c) resin powder, and d) carbon sample.....	27
Figure 14: Representation of the different thermal treatments.....	28
Figure 15: Formation of the pluronic/resol complex during EISA promoted by solvent evaporation. Adjusted from (Meng et al., 2005).....	29
Figure 16: a) colour change after adding copper nitrate to the resin mixing and b) sample Cu_CND_T0.....	30
Figure 17: a) Micrometrics Tristar II 3020 and b) degassing station FlowPrep060.	31
Figure 18: a) Malvern Panalytical X'Pert PRO X-ray diffractometer and b) ZEISS Merlin FESEM.....	32
Figure 19: Equipment for Raman spectroscopy.....	32
Figure 20: Schematic representation of the electrochemical cell used for testing the electrochemical activity.	34
Figure 21: a) setup used for RDE testing and b) top view of the RDE.....	35
Figure 22: Images of the working electrodes used a) RDE and b) carbon paper.	37
Figure 23: a) nitrogen adsorption isotherms, b) pore size distribution, c) cumulative pore volume of CND nitrogen-doped carbon samples.....	40
Figure 24: XRD spectra of nitrogen-doped carbon samples.....	42
Figure 25: XRD profile of a) Cu_CND_T0, b) CuO.	43

Figure 26: Different details for CND carbon samples: a) CND_T1 particle (50 kX), b) particle surface from CND_T1 (100kX) with detail at 500kX, c) CND_T0 sponge-like morphology (250 kX), d) CND_T2 (100kX).....	43
Figure 27: Comparison between a) CND_T0 (100kX) and b) Cu_CND-T0 (100 kX) particles surface with detail on Cu nanostructures (500kX); c) flower-shaped (25kX) and d) irregular (50kX) CuO particles.	44
Figure 28: Raman spectra of CND samples.	47
Figure 29: Visual representation of N-species percentage.	48
Figure 30: N1s profile for a) CND_T0, b) CND_T1, c) CND_T2, and d) Cu_CND_T0.	49
Figure 31: Comparison of C1s spectra of CND metal-free carbon samples.....	50
Figure 32: a) N1s and b) C1s peaks of Cu_CND_T0 and CND_T0 samples.....	51
Figure 33: CVs in N ₂ and CO ₂ for a) CND_T1 and b) CND_T2.....	52
Figure 34: a) CVs and b) LSVs in CO ₂ of both samples.....	53
Figure 35: Electrochemical CO ₂ reduction testing chronopotentiometry.....	53
Figure 36: a) Evolution of gaseous products during CP, and b) Faradaic efficiencies at -1.6 V vs RHE of the obtained liquid products.....	54
Figure 37: CVs in N ₂ and CO ₂ for a) metal-free CND samples, b) copper samples, and c) CMK-3 samples.	56
Figure 38: CVs in CO ₂ without (left) and with normalized current with ECSA (right) for a) metal-free CND samples, b) copper samples, and c) CMK-3 samples.	57
Figure 39: CA in CO ₂ at -0.4, -0.6, -1 V vs RHE.	59
Figure 40: FE of gaseous products for a) CND metal-free carbon samples, b) CMK-3 samples, and c) copper samples.	60
Figure 41: Liquid products productivity for carbon paper electrodes.	63
Figure 42: FE for liquid products with corresponding carbon structure representations.	63

List of tables

Table 1: Examples of metallic catalyst for CO ₂ RR. Current densities are reported in absolute value.	12
Table 2: Interesting carbon-based and single-atom catalyst. Current densities are in absolute value.	14
Table 3: Table of products with half-cell reaction. Potential referred to standard hydrogen electrode (SHE) at pH 7 in aqueous solution. Data from (K. Zhao & Quan, 2021).	15
Table 4: Thermal treatments parameters.	27
Table 5: Sample list with the corresponding heat treatments.	30
Table 6: Specific surface area (SSA) and average pore size.	41
Table 7: EDS results.	45
Table 8: Raman spectroscopy results.	46
Table 9: Composition of samples in atomic percentage (%at).	47
Table 10: Nitrogen species percentage.	48
Table 11: Physical characterisation results for samples CND_T1 and CND_T2.	51
Table 12: FE for gaseous products at -1.6 V vs RHE.	54
Table 13: Liquid products productivity.	55
Table 14: ECSA calculated values.	58
Table 15: FE of gaseous products.	59
Table 16: Liquid products productivity for carbon paper electrodes.	62
Table 17: Liquid products FE for carbon paper electrodes.	62

Bibliography

- Albo, J., Perfecto-Irigaray, M., Beobide, G., & Irabien, A. (2019). Cu/Bi metal-organic framework-based systems for an enhanced electrochemical transformation of CO₂ to alcohols. *Journal of CO₂ Utilization*, 33, 157–165. <https://doi.org/10.1016/j.jcou.2019.05.025>
- Albo, J., Sáez, A., Solla-Gullón, J., Montiel, V., & Irabien, A. (2015). Production of methanol from CO₂ electroreduction at Cu₂O and Cu₂O/ZnO-based electrodes in aqueous solution. *Applied Catalysis B: Environmental*, 176–177, 709–717. <https://doi.org/10.1016/j.apcatb.2015.04.055>
- Alinajafi, H. A., Ensafi, A. A., & Rezaei, B. (2018). Reduction of carbon dioxide to methanol on the surface of adenine functionalized reduced graphene oxide at a low potential. *International Journal of Hydrogen Energy*, 43(52), 23262–23274. <https://doi.org/10.1016/j.ijhydene.2018.10.188>
- Allahyarzadeh-Bidgoli, A., Hamidishad, N., & Yanagihara, J. I. (2022). Carbon Capture and Storage Energy Consumption and Performance Optimization Using Metamodels and Response Surface Methodology. *Journal of Energy Resources Technology, Transactions of the ASME*, 144(5). <https://doi.org/10.1115/1.4051679>
- Ayinla, R. T., Dennis, J. O., Zaid, H. M., Sanusi, Y. K., Usman, F., & Adebayo, L. L. (2019). A review of technical advances of recent palm bio-waste conversion to activated carbon for energy storage. *Journal of Cleaner Production*, 229, 1427–1442. <https://doi.org/10.1016/j.jclepro.2019.04.116>
- Ballem, M. A., Córdoba, J. M., & Odén, M. (2010). Influence of synthesis temperature on morphology of SBA-16 mesoporous materials with a three-dimensional pore system. *Microporous and Mesoporous Materials*, 129(1–2), 106–111. <https://doi.org/10.1016/j.micromeso.2009.09.004>
- Baur, J. E. (2007). Diffusion Coefficients. In *Handbook of Electrochemistry* (pp. 829–848). Elsevier. <https://doi.org/10.1016/B978-044451958-0.50036-7>
- Biesinger, M. C., Lau, L. W. M., Gerson, A. R., & Smart, R. St. C. (2010). Resolving surface chemical states in XPS analysis of first row transition metals, oxides and hydroxides: Sc, Ti, V, Cu and Zn. *Applied Surface Science*, 257(3), 887–898. <https://doi.org/10.1016/j.apsusc.2010.07.086>
- Birdja, Y. Y., Pérez-Gallent, E., Figueiredo, M. C., Göttle, A. J., Calle-Vallejo, F., & Koper, M. T. M. (2019). Advances and challenges in understanding the electrocatalytic conversion of carbon dioxide to fuels. In *Nature Energy* (Vol. 4, Issue 9, pp. 732–745). Nature Publishing Group. <https://doi.org/10.1038/s41560-019-0450-y>
- Catizzzone, E., Bonura, G., Migliori, M., Frusteri, F., & Giordano, G. (2018). CO₂ recycling to dimethyl ether: State-of-the-art and perspectives. In *Molecules* (Vol. 23, Issue 1). MDPI AG. <https://doi.org/10.3390/molecules23010031>
- Cheng, T., Xiao, H., & Goddard, W. A. (2015). Free-Energy Barriers and Reaction Mechanisms for the Electrochemical Reduction of CO on the Cu(100) Surface,

Including Multiple Layers of Explicit Solvent at pH 0. *Journal of Physical Chemistry Letters*, 6(23), 4767–4773. <https://doi.org/10.1021/acs.jpcllett.5b02247>

- Clark, E. L., Resasco, J., Landers, A., Lin, J., Chung, L. T., Walton, A., Hahn, C., Jaramillo, T. F., & Bell, A. T. (2018). Standards and Protocols for Data Acquisition and Reporting for Studies of the Electrochemical Reduction of Carbon Dioxide. *ACS Catalysis*, 8(7), 6560–6570. <https://doi.org/10.1021/acscatal.8b01340>
- Croce, A., Re, G., Bisio, C., Gatti, G., Coluccia, S., & Marchese, L. (2021). On the correlation between Raman spectra and structural properties of activated carbons derived by hyper-crosslinked polymers. *Research on Chemical Intermediates*, 47(1), 419–431. <https://doi.org/10.1007/s11164-020-04338-x>
- Das, C. K., Bass, O., Kothapalli, G., Mahmoud, T. S., & Habibi, D. (2018). Overview of energy storage systems in distribution networks: Placement, sizing, operation, and power quality. In *Renewable and Sustainable Energy Reviews* (Vol. 91, pp. 1205–1230). Elsevier Ltd. <https://doi.org/10.1016/j.rser.2018.03.068>
- Dasgupta, K., & Sathiyamoorthy, D. (2003). Disordered carbon—its preparation, structure, and characterisation. *Materials Science and Technology*, 19(8), 995–1002. <https://doi.org/10.1179/026708303225004693>
- Davis, M. E. (2002). Ordered porous materials for emerging applications. *Nature*, 417(6891), 813–821. <https://doi.org/10.1038/nature00785>
- de Coninck, H., & Benson, S. M. (2014). Carbon dioxide capture and storage: Issues and prospects. In *Annual Review of Environment and Resources* (Vol. 39, pp. 243–270). Annual Reviews Inc. <https://doi.org/10.1146/annurev-environ-032112-095222>
- Dongare, S., Singh, N., Bhunia, H., Bajpai, P. K., & Das, A. K. (2021). Electrochemical Reduction of Carbon Dioxide to Ethanol: A Review. In *ChemistrySelect* (Vol. 6, Issue 42, pp. 11603–11629). John Wiley and Sons Inc. <https://doi.org/10.1002/slct.202102829>
- Du, J., Li, S., Liu, S., Xin, Y., Chen, B., Liu, H., & Han, B. (2020). Selective electrochemical reduction of carbon dioxide to ethanol via a relay catalytic platform. *Chemical Science*, 11(19), 5098–5104. <https://doi.org/10.1039/d0sc01133a>
- Du, Q.-S., Tang, P.-D., Huang, H.-L., Du, F.-L., Huang, K., Xie, N.-Z., Long, S.-Y., Li, Y.-M., Qiu, J.-S., & Huang, R.-B. (2017). A new type of two-dimensional carbon crystal prepared from 1,3,5-trihydroxybenzene. *Scientific Reports*, 7(1), 40796. <https://doi.org/10.1038/srep40796>
- Duan, X., Xu, J., Wei, Z., Ma, J., Guo, S., Wang, S., Liu, H., & Dou, S. (2017a). Metal-Free Carbon Materials for CO₂ Electrochemical Reduction. In *Advanced Materials* (Vol. 29, Issue 41). Wiley-VCH Verlag. <https://doi.org/10.1002/adma.201701784>
- Duan, X., Xu, J., Wei, Z., Ma, J., Guo, S., Wang, S., Liu, H., & Dou, S. (2017b). Metal-Free Carbon Materials for CO₂ Electrochemical Reduction. In *Advanced Materials* (Vol. 29, Issue 41). Wiley-VCH Verlag. <https://doi.org/10.1002/adma.201701784>
- Eren, E. O., & Özkar, S. (2021). Recent advances in heterogeneous catalysts for the effective electroreduction of carbon dioxide to carbon monoxide. In *Journal of Power Sources* (Vol. 506). Elsevier B.V. <https://doi.org/10.1016/j.jpowsour.2021.230215>

- Fan, Q., Zhang, M., Jia, M., Liu, S., Qiu, J., & Sun, Z. (2018). Electrochemical CO₂ reduction to C₂⁺ species: Heterogeneous electrocatalysts, reaction pathways, and optimization strategies. In *Materials Today Energy* (Vol. 10, pp. 280–301). Elsevier Ltd. <https://doi.org/10.1016/j.mtener.2018.10.003>
- Gawande, M. B., Fornasiero, P., & Zbořil, R. (2020). Carbon-Based Single-Atom Catalysts for Advanced Applications. *ACS Catalysis*, 10(3), 2231–2259. <https://doi.org/10.1021/acscatal.9b04217>
- Guzmán, H., Russo, N., & Hernández, S. (2021). CO₂ valorisation towards alcohols by Cu-based electrocatalysts: challenges and perspectives. In *Green Chemistry* (Vol. 23, Issue 5, pp. 1896–1920). Royal Society of Chemistry. <https://doi.org/10.1039/d0gc03334k>
- Guzmán, H., Zammillo, F., Roldán, D., Galletti, C., Russo, N., & Hernández, S. (2021). Investigation of Gas Diffusion Electrode Systems for the Electrochemical CO₂ Conversion. *Catalysts*, 11(4), 482. <https://doi.org/10.3390/catal11040482>
- Hori, Y., Kikuchi, K., & Suzuki, S. (1985). PRODUCTION OF CO AND CH₄ IN ELECTROCHEMICAL REDUCTION OF CO₂ AT METAL ELECTRODES IN AQUEOUS HYDROGENCARBONATE SOLUTION. *Chemistry Letters*, 14(11), 1695–1698. <https://doi.org/10.1246/cl.1985.1695>
- Hori, Y., Murata, A., & Takahashi, R. (1989). Formation of hydrocarbons in the electrochemical reduction of carbon dioxide at a copper electrode in aqueous solution. *Journal of the Chemical Society, Faraday Transactions 1: Physical Chemistry in Condensed Phases*, 85(8), 2309–2326. <https://doi.org/10.1039/F19898502309>
- Inagaki, M., Toyoda, M., & Tsumura, T. (2014). Control of crystalline structure of porous carbons. In *RSC Advances* (Vol. 40, Issue 78, pp. 41411–41424). Royal Society of Chemistry. <https://doi.org/10.1039/c4ra06730d>
- Jia, C., Dastafkan, K., & Zhao, C. (2022). Key factors for designing single-atom metal-nitrogen-carbon catalysts for electrochemical CO₂ reduction. In *Current Opinion in Electrochemistry* (Vol. 31). Elsevier B.V. <https://doi.org/10.1016/j.coelec.2021.100854>
- Ju, W., Bagger, A., Hao, G.-P., Varela, A. S., Sinev, I., Bon, V., Roldan Cuenya, B., Kaskel, S., Rossmeisl, J., & Strasser, P. (2017). Understanding activity and selectivity of metal-nitrogen-doped carbon catalysts for electrochemical reduction of CO₂. *Nature Communications*, 8(1), 944. <https://doi.org/10.1038/s41467-017-01035-z>
- Karapinar, D., Huan, N. T., Ranjbar Sahraie, N., Li, J., Wakerley, D., Touati, N., Zanna, S., Taverna, D., Galvão Tizei, L. H., Zitolo, A., Jaouen, F., Mougél, V., & Fontecave, M. (2019). Electroreduction of CO₂ on Single-Site Copper-Nitrogen-Doped Carbon Material: Selective Formation of Ethanol and Reversible Restructuration of the Metal Sites. *Angewandte Chemie*, 131(42), 15242–15247. <https://doi.org/10.1002/ange.201907994>
- Khan, S. B., Faisal, M., Rahman, M. M., Abdel-Latif, I. A., Ismail, A. A., Akhtar, K., Al-Hajry, A., Asiri, A. M., & Alamry, K. A. (2013). Highly sensitive and stable phenyl hydrazine chemical sensors based on CuO flower shapes and hollow spheres. *New Journal of Chemistry*, 37(4), 1098. <https://doi.org/10.1039/c3nj40928g>

- Kong, L., Zhao, J., Han, S., Zhang, T., He, L., Zhang, P., & Dai, S. (2019). Facile Synthesis of Copper Containing Ordered Mesoporous Polymers via Aqueous Coordination Self-Assembly for Aerobic Oxidation of Alcohols. *Industrial & Engineering Chemistry Research*, 58(16), 6438–6445. <https://doi.org/10.1021/acs.iecr.9b00669>
- Kozuch, S., & Martin, J. M. L. (2012). “Turning Over” Definitions in Catalytic Cycles. *ACS Catalysis*, 2(12), 2787–2794. <https://doi.org/10.1021/cs3005264>
- Lee, S.-M., Lee, S.-H., & Roh, J.-S. (2021). Analysis of Activation Process of Carbon Black Based on Structural Parameters Obtained by XRD Analysis. *Crystals*, 11(2), 153. <https://doi.org/10.3390/cryst11020153>
- Li, J., Abbas, S. U., Wang, H., Zhang, Z., & Hu, W. (2021). Recent Advances in Interface Engineering for Electrocatalytic CO₂ Reduction Reaction. In *Nano-Micro Letters* (Vol. 13, Issue 1). Springer Science and Business Media B.V. <https://doi.org/10.1007/s40820-021-00738-9>
- Li, L., Huang, Y., & Li, Y. (2020). Carbonaceous materials for electrochemical CO₂ reduction. *EnergyChem*, 2(1), 100024. <https://doi.org/10.1016/j.enchem.2019.100024>
- Li, Y. C., Wang, Z., Yuan, T., Nam, D. H., Luo, M., Wicks, J., Chen, B., Li, J., Li, F., de Arquer, F. P. G., Wang, Y., Dinh, C. T., Voznyy, O., Sinton, D., & Sargent, E. H. (2019). Binding Site Diversity Promotes CO₂ Electroreduction to Ethanol. *Journal of the American Chemical Society*, 141(21), 8584–8591. <https://doi.org/10.1021/jacs.9b02945>
- Li, Y., & Sun, Q. (2016). Recent Advances in Breaking Scaling Relations for Effective Electrochemical Conversion of CO₂. *Advanced Energy Materials*, 6(17). <https://doi.org/10.1002/aenm.201600463>
- Li, Y., Tian, Z., & Chen, L. (2021). Theoretical Understanding of the Interface Effect in Promoting Electrochemical CO₂ Reduction on Cu-Pd Alloys. *Journal of Physical Chemistry C*, 125(39), 21381–21389. <https://doi.org/10.1021/acs.jpcc.1c03330>
- Liang, C., Li, Z., & Dai, S. (2008). Mesoporous Carbon Materials: Synthesis and Modification. *Angewandte Chemie International Edition*, 47(20), 3696–3717. <https://doi.org/10.1002/anie.200702046>
- Liang, S., Huang, L., Gao, Y., Wang, Q., & Liu, B. (2021). Electrochemical Reduction of CO₂ to CO over Transition Metal/N-Doped Carbon Catalysts: The Active Sites and Reaction Mechanism. In *Advanced Science* (Vol. 8, Issue 24). John Wiley and Sons Inc. <https://doi.org/10.1002/advs.202102886>
- Lin, L., Liu, T., Xiao, J., Li, H., Wei, P., Gao, D., Nan, B., Si, R., Wang, G., & Bao, X. (2020). Enhancing CO₂ Electroreduction to Methane with a Cobalt Phthalocyanine and Zinc–Nitrogen–Carbon Tandem Catalyst. *Angewandte Chemie International Edition*, 59(50), 22408–22413. <https://doi.org/10.1002/anie.202009191>
- Ling, Y., Ma, Q., Yu, Y., & Zhang, B. (2021). Optimization Strategies for Selective CO₂ Electroreduction to Fuels. In *Transactions of Tianjin University* (Vol. 27, Issue 3, pp. 180–200). Tianjin University. <https://doi.org/10.1007/s12209-021-00283-x>
- Liu, A., Gao, M., Ren, X., Meng, F., Yang, Y., Gao, L., Yang, Q., & Ma, T. (2020). Current progress in electrocatalytic carbon dioxide reduction to fuels on heterogeneous

- catalysts. *Journal of Materials Chemistry A*, 8(7), 3541–3562. <https://doi.org/10.1039/C9TA11966C>
- Liu, S. P., Zhao, M., Gao, W., Jiang, Q., & Jacob, T. (2017). Theoretical Studies on the CO₂ Reduction to CH₃OH on Cu(211). *Electrocatalysis*, 8(6), 647–656. <https://doi.org/10.1007/s12678-017-0403-9>
- Liu, X., Schlexer, P., Xiao, J., Ji, Y., Wang, L., Sandberg, R. B., Tang, M., Brown, K. S., Peng, H., Ringe, S., Hahn, C., Jaramillo, T. F., Nørskov, J. K., & Chan, K. (2019). pH effects on the electrochemical reduction of CO (2) towards C₂ products on stepped copper. *Nature Communications*, 10(1). <https://doi.org/10.1038/s41467-018-07970-9>
- Liu, Y., Zhang, Y., Cheng, K., Quan, X., Fan, X., Su, Y., Chen, S., Zhao, H., Zhang, Y., Yu, H., & Hoffmann, M. R. (2017). Selective Electrochemical Reduction of Carbon Dioxide to Ethanol on a Boron- and Nitrogen-Co-doped Nanodiamond. *Angewandte Chemie*, 129(49), 15813–15817. <https://doi.org/10.1002/ange.201706311>
- Long, G., Wan, K., Liu, M., Li, X., Liang, Z., & Piao, J. (2015). Effect of pyrolysis conditions on nitrogen-doped ordered mesoporous carbon electrocatalysts. *Cuihua Xuebao/Chinese Journal of Catalysis*, 36(8), 1197–1204. [https://doi.org/10.1016/S1872-2067\(15\)60912-3](https://doi.org/10.1016/S1872-2067(15)60912-3)
- Lu, L., Sun, X., Ma, J., Yang, D., Wu, H., Zhang, B., Zhang, J., & Han, B. (2018). Highly Efficient Electroreduction of CO₂ to Methanol on Palladium-Copper Bimetallic Aerogels. *Angewandte Chemie International Edition*, 57(43), 14149–14153. <https://doi.org/10.1002/anie.201808964>
- Ma, X., Du, J., Sun, H., Ye, F., Wang, X., Xu, P., Hu, C., Zhang, L., & Liu, D. (2021). Boron, nitrogen co-doped carbon with abundant mesopores for efficient CO₂ electroreduction. *Applied Catalysis B: Environmental*, 298, 120543. <https://doi.org/10.1016/j.apcatb.2021.120543>
- Maruccia, E., Lourenço, M. A. O., Priamushko, T., Bartoli, M., Bocchini, S., Pirri, F. C., Saracco, G., Kleitz, F., & Gerbaldi, C. (2022). Nanocast nitrogen-containing ordered mesoporous carbons from glucosamine for selective CO₂ capture. *Materials Today Sustainability*, 17, 100089. <https://doi.org/10.1016/j.mtsust.2021.100089>
- Massardier, V., Voron, L., Esnouf, C., & Merlin, J. (2001). Identification of the nitrides formed during the annealing of a low-carbon low-aluminium steel. *Journal of Materials Science*, 36(6), 1363–1371. <https://doi.org/10.1023/A:1017547318732>
- Meng, Y., Gu, D., Zhang, F., Shi, Y., Cheng, L., Feng, D., Wu, Z., Chen, Z., Wan, Y., Stein, A., & Zhao, D. (2006). A family of highly ordered mesoporous polymer resin and carbon structures from organic-organic self-assembly. *Chemistry of Materials*, 18(18), 4447–4464. <https://doi.org/10.1021/cm060921u>
- Meng, Y., Gu, D., Zhang, F., Shi, Y., Yang, H., Li, Z., Yu, C., Tu, B., & Zhao, D. (2005). Ordered mesoporous polymers and homologous carbon frameworks: Amphiphilic surfactant templating and direct transformation. *Angewandte Chemie - International Edition*, 44(43), 7053–7059. <https://doi.org/10.1002/anie.200501561>
- Meng, Z., Chen, N., Cai, S., Wang, R., Guo, W., & Tang, H. (2021). <sc>Co-N</sc>-doped hierarchically ordered macro/mesoporous carbon as bifunctional electrocatalyst

- toward oxygen reduction/evolution reactions. *International Journal of Energy Research*, 45(4), 6250–6261. <https://doi.org/10.1002/er.6247>
- Morales, D. M., & Risch, M. (2021). Seven steps to reliable cyclic voltammetry measurements for the determination of double layer capacitance. *JPhys Energy*, 3(3). <https://doi.org/10.1088/2515-7655/abee33>
- Natsui, K., Iwakawa, H., Ikemiya, N., Nakata, K., & Einaga, Y. (2018). Stable and Highly Efficient Electrochemical Production of Formic Acid from Carbon Dioxide Using Diamond Electrodes. *Angewandte Chemie International Edition*, 57(10), 2639–2643. <https://doi.org/10.1002/anie.201712271>
- Ni, J., Huang, Y., & Gao, L. (2013). A high-performance hard carbon for Li-ion batteries and supercapacitors application. *Journal of Power Sources*, 223, 306–311. <https://doi.org/10.1016/j.jpowsour.2012.09.047>
- Ni, Y., Chen, Z., Kong, F., Qiao, Y., Kong, A., & Shan, Y. (2017). Space-confined synthesis of multilayer Cu–N-doped graphene nanosheets for efficient oxygen electroreduction. *Dalton Transactions*, 46(26), 8586–8592. <https://doi.org/10.1039/C7DT01614J>
- Nicolas, R., Bérubé, F., Kim, T. W., Thommes, M., & Kleitz, F. (2008). Tailoring mesoporosity and intrawall porosity in large pore silicas: synthesis and nitrogen sorption behavior. *Studies in Surface Science and Catalysis*, 174(SUPPL. PART A), 141–148. [https://doi.org/10.1016/S0167-2991\(08\)80165-6](https://doi.org/10.1016/S0167-2991(08)80165-6)
- Nitopi, S., Bertheussen, E., Scott, S. B., Liu, X., Engstfeld, A. K., Horch, S., Seger, B., Stephens, I. E. L., Chan, K., Hahn, C., Nørskov, J. K., Jaramillo, T. F., & Chorkendorff, I. (2019). Progress and Perspectives of Electrochemical CO₂ Reduction on Copper in Aqueous Electrolyte. In *Chemical Reviews* (Vol. 119, Issue 12, pp. 7610–7672). American Chemical Society. <https://doi.org/10.1021/acs.chemrev.8b00705>
- North, M. (2015). What is CO₂? Thermodynamics, Basic Reactions and Physical Chemistry. In *Carbon Dioxide Utilisation: Closing the Carbon Cycle: First Edition* (pp. 3–17). Elsevier Inc. <https://doi.org/10.1016/B978-0-444-62746-9.00001-3>
- Pérez-Rodríguez, S., Pastor, E., & Lázaro, M. J. (2017). Noble metal-free catalysts supported on carbon for CO₂ electrochemical reduction. *Journal of CO₂ Utilization*, 18, 41–52. <https://doi.org/10.1016/j.jcou.2017.01.010>
- Rabiee, H., Ge, L., Zhang, X., Hu, S., Li, M., & Yuan, Z. (2021). Gas diffusion electrodes (GDEs) for electrochemical reduction of carbon dioxide, carbon monoxide, and dinitrogen to value-added products: A review. In *Energy and Environmental Science* (Vol. 14, Issue 4, pp. 1959–2008). Royal Society of Chemistry. <https://doi.org/10.1039/d0ee03756g>
- Rasul, S., Anjum, D. H., Jedidi, A., Minenkov, Y., Cavallo, L., & Takanabe, K. (2015). A highly selective copper-indium bimetallic electrocatalyst for the electrochemical reduction of aqueous CO₂ to CO. *Angewandte Chemie - International Edition*, 54(7), 2146–2150. <https://doi.org/10.1002/anie.201410233>

- Ray, S. C., Mbiombi, W., & Papakonstantinou, P. (2014). Electrical and electronic properties of nitrogen doped amorphous carbon (a-CN_x) thin films. *Current Applied Physics*, 14(12), 1845–1848. <https://doi.org/10.1016/j.cap.2014.10.016>
- Roy, S., Cherevotan, A., & Peter, S. C. (2018). Thermochemical CO₂ Hydrogenation to Single Carbon Products: Scientific and Technological Challenges. *ACS Energy Letters*, 3(8), 1938–1966. <https://doi.org/10.1021/acscenergylett.8b00740>
- Ryoo, R., Joo, S. H., & Jun, S. (1999). Synthesis of highly ordered carbon molecular sieves via template-mediated structural transformation. *Journal of Physical Chemistry B*, 103(37), 7743–7746. <https://doi.org/10.1021/jp991673a>
- Santiso, E. E., George, A. M., Turner, C. H., Kostov, M. K., Gubbins, K. E., Buongiorno-Nardelli, M., & Sliwiska-Bartkowiak, M. (2005). Adsorption and catalysis: The effect of confinement on chemical reactions. *Applied Surface Science*, 252(3), 766–777. <https://doi.org/10.1016/j.apsusc.2005.02.101>
- Schild, J., Reuillard, B., Morozan, A., Chenevier, P., Gravel, E., Doris, E., & Artero, V. (2021). Approaching Industrially Relevant Current Densities for Hydrogen Oxidation with a Bioinspired Molecular Catalytic Material. *Journal of the American Chemical Society*, 143(43), 18150–18158. <https://doi.org/10.1021/jacs.1c07093>
- Shinagawa, T., Larrazábal, G. O., Martín, A. J., Krumeich, F., & Pérez-Ramírez, J. (2018). Sulfur-Modified Copper Catalysts for the Electrochemical Reduction of Carbon Dioxide to Formate. *ACS Catalysis*, 8(2), 837–844. <https://doi.org/10.1021/acscatal.7b03161>
- Singh, G., Lee, J., Karakoti, A., Bahadur, R., Yi, J., Zhao, D., Albahily, K., & Vinu, A. (2020). Emerging trends in porous materials for CO₂ capture and conversion. In *Chemical Society Reviews* (Vol. 49, Issue 13, pp. 4360–4404). Royal Society of Chemistry. <https://doi.org/10.1039/d0cs00075b>
- Song, Y., Chen, W., Zhao, C., Li, S., Wei, W., & Sun, Y. (2017). Metal-Free Nitrogen-Doped Mesoporous Carbon for Electroreduction of CO₂ to Ethanol. *Angewandte Chemie - International Edition*, 56(36), 10840–10844. <https://doi.org/10.1002/anie.201706777>
- Song, Y., Peng, R., Hensley, D. K., Bonnesen, P. v., Liang, L., Wu, Z., Meyer, H. M., Chi, M., Ma, C., Sumpter, B. G., & Rondinone, A. J. (2016). High-Selectivity Electrochemical Conversion of CO₂ to Ethanol using a Copper Nanoparticle/N-Doped Graphene Electrode. *ChemistrySelect*, 1(19), 6055–6061. <https://doi.org/10.1002/slct.201601169>
- Sun, K., Wu, L., Qin, W., Zhou, J., Hu, Y., Jiang, Z., Shen, B., & Wang, Z. (2016). Enhanced electrochemical reduction of CO₂ to CO on Ag electrocatalysts with increased unoccupied density of states. *Journal of Materials Chemistry A*, 4(32), 12616–12623. <https://doi.org/10.1039/c6ta04325a>
- Sun, X., Kang, X., Zhu, Q., Ma, J., Yang, G., Liu, Z., & Han, B. (2016). Very highly efficient reduction of CO₂ to CH₄ using metal-free N-doped carbon electrodes. *Chemical Science*, 7(4), 2883–2887. <https://doi.org/10.1039/C5SC04158A>
- Sun, Z., Ma, T., Tao, H., Fan, Q., & Han, B. (2017). Fundamentals and Challenges of Electrochemical CO₂ Reduction Using Two-Dimensional Materials. In *Chem* (Vol. 3, Issue 4, pp. 560–587). Elsevier Inc. <https://doi.org/10.1016/j.chempr.2017.09.009>

- Tian, W., Zhang, H., Duan, X., Sun, H., Shao, G., & Wang, S. (2020). Porous Carbons: Structure-Oriented Design and Versatile Applications. *Advanced Functional Materials*, 30(17), 1909265. <https://doi.org/10.1002/adfm.201909265>
- Wang, G., Chen, J., Ding, Y., Cai, P., Yi, L., Li, Y., Tu, C., Hou, Y., Wen, Z., & Dai, L. (2021). Electrocatalysis for CO₂ conversion: From fundamentals to value-added products. In *Chemical Society Reviews* (Vol. 50, Issue 8, pp. 4993–5061). Royal Society of Chemistry. <https://doi.org/10.1039/d0cs00071j>
- Wang, H., Chen, Y., Hou, X., Ma, C., & Tan, T. (2016). Nitrogen-doped graphenes as efficient electrocatalysts for the selective reduction of carbon dioxide to formate in aqueous solution. *Green Chemistry*, 18(11), 3250–3256. <https://doi.org/10.1039/C6GC00410E>
- Wang, Y., Wang, D., Dares, C. J., Marquard, S. L., Sheridan, M. v., & Meyer, T. J. (2017). CO₂ reduction to acetate in mixtures of ultrasmall (Cu)_n(Ag)_m bimetallic nanoparticles. *Proceedings of the National Academy of Sciences of the United States of America*, 115(2), 278–283. <https://doi.org/10.1073/pnas.1713962115>
- Wei, J., Zhou, D., Sun, Z., Deng, Y., Xia, Y., & Zhao, D. (2013). A controllable synthesis of rich nitrogen-doped ordered mesoporous carbon for CO₂ capture and supercapacitors. *Advanced Functional Materials*, 23(18), 2322–2328. <https://doi.org/10.1002/adfm.201202764>
- Wei, X., Wei, S., Cao, S., Hu, Y., Zhou, S., Liu, S., Wang, Z., & Lu, X. (2021). Cu acting as Fe activity promoter in dual-atom Cu/Fe-NC catalyst in CO₂RR to C₁ products. *Applied Surface Science*, 564. <https://doi.org/10.1016/j.apsusc.2021.150423>
- Woldu, A. R., Huang, Z., Zhao, P., Hu, L., & Astruc, D. (2022). Electrochemical CO₂ reduction (CO₂RR) to multi-carbon products over copper-based catalysts. *Coordination Chemistry Reviews*, 454, 214340. <https://doi.org/10.1016/j.ccr.2021.214340>
- Wu, C.-K., Yin, M., O'Brien, S., & Koberstein, J. T. (2006). Quantitative Analysis of Copper Oxide Nanoparticle Composition and Structure by X-ray Photoelectron Spectroscopy. *Chemistry of Materials*, 18(25), 6054–6058. <https://doi.org/10.1021/cm061596d>
- Wu, J., Liu, M., Sharma, P. P., Yadav, R. M., Ma, L., Yang, Y., Zou, X., Zhou, X. D., Vajtai, R., Yakobson, B. I., Lou, J., & Ajayan, P. M. (2016). Incorporation of Nitrogen Defects for Efficient Reduction of CO₂ via Two-Electron Pathway on Three-Dimensional Graphene Foam. *Nano Letters*, 16(1), 466–470. <https://doi.org/10.1021/acs.nanolett.5b04123>
- Wu, J., Sharifi, T., Gao, Y., Zhang, T., & Ajayan, P. M. (2019). Emerging Carbon-Based Heterogeneous Catalysts for Electrochemical Reduction of Carbon Dioxide into Value-Added Chemicals. In *Advanced Materials* (Vol. 31, Issue 13). Wiley-VCH Verlag. <https://doi.org/10.1002/adma.201804257>
- Wu, J., Yadav, R. M., Liu, M., Sharma, P. P., Tiwary, C. S., Ma, L., Zou, X., Zhou, X.-D., Yakobson, B. I., Lou, J., & Ajayan, P. M. (2015). Achieving Highly Efficient, Selective, and Stable CO₂ Reduction on Nitrogen-Doped Carbon Nanotubes. *ACS Nano*, 9(5), 5364–5371. <https://doi.org/10.1021/acs.nano.5b01079>

- Xie, J., Zhao, X., Wu, M., Li, Q., Wang, Y., & Yao, J. (2018). Metal-Free Fluorine-Doped Carbon Electrocatalyst for CO₂ Reduction Outcompeting Hydrogen Evolution. *Angewandte Chemie International Edition*, 57(31), 9640–9644. <https://doi.org/10.1002/anie.201802055>
- Xie, W., Li, H., Cui, G., Li, J., Song, Y., Li, S., Zhang, X., Lee, J. Y., Shao, M., & Wei, M. (2021). NiSn Atomic Pair on an Integrated Electrode for Synergistic Electrocatalytic CO₂ Reduction. *Angewandte Chemie International Edition*, 60(13), 7382–7388. <https://doi.org/10.1002/anie.202014655>
- Xing, Z., Shi, K., Hu, X., & Feng, X. (2022). Beyond catalytic materials: Controlling local gas/liquid environment in the catalyst layer for CO₂ electrolysis. *Journal of Energy Chemistry*, 66, 45–51. <https://doi.org/10.1016/j.jechem.2021.07.006>
- Yadav, S., & Mondal, S. S. (2022). A review on the progress and prospects of oxy-fuel carbon capture and sequestration (CCS) technology. *Fuel*, 308, 122057. <https://doi.org/10.1016/j.fuel.2021.122057>
- Yang, F., Yu, H., Mao, X., Meng, Q., Chen, S., Deng, Q., Zeng, Z., Wang, J., & Deng, S. (2021). Boosting electrochemical CO₂ reduction on ternary heteroatoms-doped porous carbon. *Chemical Engineering Journal*, 425. <https://doi.org/10.1016/j.cej.2021.131661>
- Yang, H., Wu, Y., Li, G., Lin, Q., Hu, Q., Zhang, Q., Liu, J., & He, C. (2019). Scalable Production of Efficient Single-Atom Copper Decorated Carbon Membranes for CO₂ Electroreduction to Methanol. *Journal of the American Chemical Society*, 141(32), 12717–12723. <https://doi.org/10.1021/jacs.9b04907>
- Yang, Z., & Mokaya, R. (2008). Probing the effect of the carbonisation process on the textural properties and morphology of mesoporous carbons. *Microporous and Mesoporous Materials*, 113(1–3), 378–384. <https://doi.org/10.1016/j.micromeso.2007.11.035>
- Yang, Z., Zhang, Y., & Schnepf, Z. (2015). Soft and hard templating of graphitic carbon nitride. In *Journal of Materials Chemistry A* (Vol. 3, Issue 27, pp. 14081–14092). Royal Society of Chemistry. <https://doi.org/10.1039/c5ta02156a>
- Zeng, J., Bejtka, K., Ju, W., Castellino, M., Chiodoni, A., Sacco, A., Farkhondeh, M. A., Hernández, S., Rentsch, D., Battaglia, C., & Pirri, C. F. (2018). Advanced Cu-Sn foam for selectively converting CO₂ to CO in aqueous solution. *Applied Catalysis B: Environmental*, 236, 475–482. <https://doi.org/10.1016/j.apcatb.2018.05.056>
- Zhao, K., Nie, X., Wang, H., Chen, S., Quan, X., Yu, H., Choi, W., Zhang, G., Kim, B., & Chen, J. G. (2020). Selective electroreduction of CO₂ to acetone by single copper atoms anchored on N-doped porous carbon. *Nature Communications*, 11(1), 2455. <https://doi.org/10.1038/s41467-020-16381-8>
- Zhao, K., & Quan, X. (2021). Carbon-based materials for electrochemical reduction of CO₂ to C₂+oxygenates: Recent progress and remaining challenges. *ACS Catalysis*, 11(4), 2076–2097. <https://doi.org/10.1021/acscatal.0c04714>

- Zhao, Z., Peng, X., Liu, X., Sun, X., Shi, J., Han, L., Li, G., & Luo, J. (2017). Efficient and stable electroreduction of CO₂ to CH₄ on CuS nanosheet arrays. *Journal of Materials Chemistry A*, 5(38), 20239–20243. <https://doi.org/10.1039/C7TA05507B>
- Zheng, X., de Luna, P., García de Arquer, F. P., Zhang, B., Becknell, N., Ross, M. B., Li, Y., Banis, M. N., Li, Y., Liu, M., Voznyy, O., Dinh, C. T., Zhuang, T., Stadler, P., Cui, Y., Du, X., Yang, P., & Sargent, E. H. (2017). Sulfur-Modulated Tin Sites Enable Highly Selective Electrochemical Reduction of CO₂ to Formate. *Joule*, 1(4), 794–805. <https://doi.org/10.1016/j.joule.2017.09.014>
- Zheng, Y., Vasileff, A., Zhou, X., Jiao, Y., Jaroniec, M., & Qiao, S. Z. (2019). Understanding the Roadmap for Electrochemical Reduction of CO₂ to Multi-Carbon Oxygenates and Hydrocarbons on Copper-Based Catalysts. *Journal of the American Chemical Society*, 141(19), 7646–7659. <https://doi.org/10.1021/jacs.9b02124>
- Zhong, Y., Wang, S., Li, M., Ma, J., Song, S., Kumar, A., Duan, H., Kuang, Y., & Sun, X. (2021). Rational design of copper-based electrocatalysts and electrochemical systems for CO₂ reduction: From active sites engineering to mass transfer dynamics. In *Materials Today Physics* (Vol. 18). Elsevier Ltd. <https://doi.org/10.1016/j.mtphys.2021.100354>
- Zhou, Y., Che, F., Liu, M., Zou, C., Liang, Z., de Luna, P., Yuan, H., Li, J., Wang, Z., Xie, H., Li, H., Chen, P., Bladt, E., Quintero-Bermudez, R., Sham, T. K., Bals, S., Hofkens, J., Sinton, D., Chen, G., & Sargent, E. H. (2018). Dopant-induced electron localization drives CO₂ reduction to C₂ hydrocarbons. *Nature Chemistry*, 10(9), 974–980. <https://doi.org/10.1038/s41557-018-0092-x>